学位論文 (要約)

# Combined experimental and theoretical study on the activation of the C–I bond of $CH_3I$ by coinage metal atoms and clusters

(貨幣金属原子・クラスターによる
$CH_3I$のC–I結合の活性化に関する実験的・理論的研究)

平成29年12月博士 (理学) 申請

東京大学大学院理学系研究科
化学専攻
村松　悟

# Abstract

The discovery of oxidation catalysis of nano-sized gold by Haruta *et al.* stimulated the practical development of highly active and selective Au catalysts. This discovery also led to fundamental studies on model systems to gain insights into the size-specific catalysis. Previous studies on Au clusters isolated in the gas phase and stabilized by polymers in water revealed the close similarity in a key step for activation of $O_2$ molecules, demonstrating that cluster-based catalysts can be developed rationally based on the fundamental knowledge on chemical properties of isolated systems.

Carbon–halogen (C–X) bond activation via oxidative addition is one of the most important reaction steps in synthetic chemistry since it is required in carbon–carbon (C–C) bond-forming reaction, the basis for constructing frameworks of a variety of organic molecules. The aim of the thesis is to obtain clues for development of coinage metal catalysts for C–X bond activation via the fundamental study on model catalytic systems. Toward this goal, I carried out combined experimental and theoretical studies on chemical reactions of methyl iodide ($CH_3I$) toward bare atomic coinage metals and small clusters to reveal whether they have a potential to activate the C–I bond and to elucidate key properties to promote the oxidative addition.

In Chapter 1, I describe the general introduction on rational design of the metal cluster catalysts. I also introduce the chemistry of atomic coinage metals, the small size limit of the clusters, and provide the current stage and challenges in C–X bond activation by Au catalysts.

In Chapter 2, I focus on the gas phase reaction of atomic $Au^-$ with $CH_3I$. The formation of the oxidative addition product $[CH_3–Au–I]^-$ is confirmed by means of mass spectrometry, photoelectron spectroscopy, and density functional theory (DFT) calculations. I discuss the mechanism of the oxidative addition, on the basis of Global Reaction Route Mapping calculations, and propose the successive reaction of $[CH_3–Au–I]^-$ to promote C–C bond-forming reaction.

In Chapter 3, I extend the scope of the reaction found in Chapter 2 to the other coinage metal anions, $Cu^-$ and $Ag^-$. The common products $[CH_3–M–I]^-$ (M = Cu, Ag, Au) are identified and their thermodynamic stabilities are compared.

In Chapter 4, I study the reaction of atomic Au with $CH_3I$ in the low-temperature neon matrix. Infrared spectroscopy and DFT calculations reveal the formation of an oxidative addition product, $[CH_3–Au–I]$, and a novel complex $[(CH_3)_2–Au–I_2]$. I show that visible light irradiation of $[(CH_3)_2–Au–I_2]$ induce the C–C bond-forming reaction to afford $C_2H_6$.

In Chapter 5, I examine the effect of the cluster size by studying the gas phase reaction of $Au_n^-$ ($n$ = 2–4) with $CH_3I$. The highest reactivity of $Au_2^-$ is confirmed based on pseudo-first order kinetic analyses. The difference in the mechanisms and products between the reactions of $Au^-$ and $Au_2^-$ is discussed.

In Chapter 6, I give a summary of the thesis and describe future prospects as a concluding remark.

# Contents

# Chapter 1.

# General introduction

## 1.1. Metal cluster catalysts

### 1.1.1. Metal nanoparticles and clusters

Over the past decades, nanoscience has emerged as a new frontier in fields of both academia and industry. Interests and challenges in this research area originate from a simple fact that structures and properties of the nano-sized material are significantly different from those observed in the bulk material.[1] In metal nanoparticles, especially in gold nanoparticles (AuNPs),[2] such examples can be seen in optical and thermodynamic properties. It is well known that colloidal dispersion of AuNPs with a diameter ~2–100 nm exhibit red color[3] as indicated by intense absorption of ~520 nm light as shown in Figure 1.1(a).[4] This optical response is due to localized surface plasmon resonance (LSPR), a collective oscillation of the electrons at the surface of the particle which occurs when the diameter of the NPs is much smaller than wavelength of the incoming light. Another unique feature is that AuNPs have much lower melting point than the bulk[5,6] due to smaller coordination number. It causes the unique thermal behavior; the AuNPs fluctuate among structural isomers with comparable energies even at temperature below the melting temperature (Figure 1.1(b)).[7] These properties are absent in the Au bulk, showing the peculiarity of nano-materials. Importantly, most of the properties of metal NPs can be predicted from their diameters and shapes; for example, ionization potentials (IP) and electron affinities (EA) of spherical metal NPs are described as functions of their diameters ($D$) according to a liquid-drop model as shown in eqs 1.1 and 1.2.[8]

$$\mathrm{IP} = W_{\mathrm{B}} + \alpha \frac{e^2}{D} \tag{1.1}$$

$$\mathrm{EA} = W_{\mathrm{B}} + \beta \frac{e^2}{D} \tag{1.2}$$

where $W_{\mathrm{B}}$ and $e$ represent the bulk work function and elementary charge, respectively, and $\alpha$ and $\beta$ are metal-dependent constants.

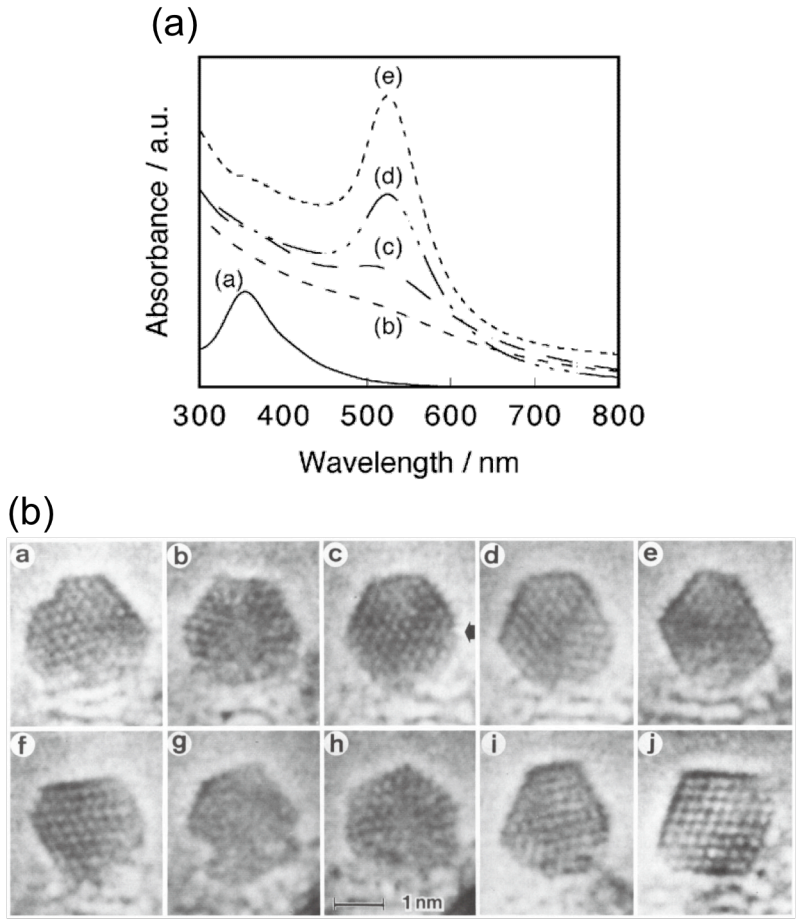


**Figure 1.1.** (a) Optical absorption spectra of solutions containing $[AuCl_4]^-$ ions (a) and AuNPs with diameters of 1.5, 3.4, 5.4, 6.8 and 9.7 nm (b, c, d, and e) covered by dodecanethiolate. (b) Snapshot images of AuNPs (diameter ~2 nm) observed by transmission electron microscopy (TEM). The shape of the particle was changing continually under electron-beam irradiation. a, d, i: particles with single twins. c, e, f, j: cuboctahedral particles. b, h: multiply twinned icosahedral particles. Reprinted from ref. 4 with permission for (a). 2008 American Chemical Society. Reprinted from ref. 7 with permission for (c). 1986 American Physical Society.

Further reduction of the diameter of metal NPs below ~2 nm leads to a distinct phase called as metal clusters. They are composed of fewer than ~100 atoms. Electronic and geometric properties of the metal clusters further deviate from the corresponding NPs and quite often cannot be scaled based on their diameters.[9] For example, the electronic energy levels in metal clusters are discrete and energy gaps are larger than

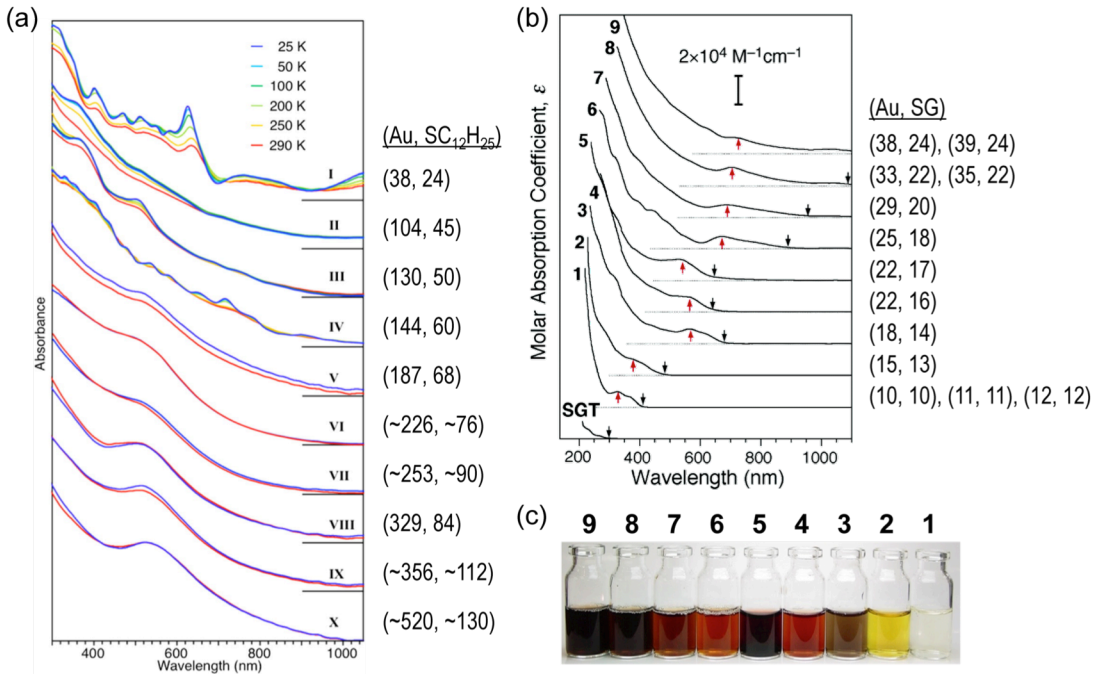


**Figure 1.2.** (a) Optical spectra of dodecanethiolate-protected Au clusters, $Au_n(SC_{12}H_{25})_m$, with the sizes of $n$ = 38–~520 recorded at several sample temperatures (25–290 K). The cluster size of each spectrum is shown on the right in the form of ($n$, $m$). (b) Optical spectra of glutathione-protected Au clusters, $Au_n(SG)_m$, with the sizes of $n$ = 10–39. Arrows in blue and red indicate band onsets and humps respectively. The cluster size of each spectrum is shown on the right in the form of ($n$, $m$). SGT represents sodium Au(I) thiomalate complex. (c) Photographs of aqueous solutions of $Au_n(SG)_m$. The sample numbers **1**–**9** correspond to those in (b). Reprinted from ref. 11 with permission for (a). 2015 American Chemical Society. Reprinted from ref. 12 with permission for (b). 2005 American Chemical Society.

thermal energy $k_BT$ ($k_B$: Boltzmann constant, $T$: temperature) even at room temperature.[10] It results in molecular-like optical properties rather than plasmonic ones. Recent progress in synthetic technique enables precise control of the number of constituent atoms (size) of Au clusters protected by thiolate ligands. Figure 1.2(a) shows evolution of optical absorption spectra of the dodecanethiolate-protected Au clusters, $Au_n(SC_{12}H_{25})_m$, as a function of $n$.[11] It is clearly seen that absorption due to the LSPR (~ 520 nm) disappears at $n \leq 144$ and quantized electronic transitions are observed instead. The size $n = 144$ also corresponds to a critical size for transition in the geometric structures; large $Au_n(SC_{12}H_{25})_m$ clusters with $n > 144$ commonly have fcc-based structures similar to the bulk Au, while small clusters with $n \leq 144$ prefer non-fcc-based structures (icosahedron or Marks decahedron). Figures 1.2(b) and (c) show the optical spectra and colors of smaller Au clusters protected by glutathione (GSH), $Au_n(SG)_m$, with sizes of $n$ = 10–39, respectively.[12] The spectra clearly demonstrate that the size difference by a few atoms drastically affects the optical properties. This fact obviously shows that the properties of the metal clusters cannot be predicted just by their diameters according to a simple scaling law. Therefore, metal clusters have a potential as novel functional materials or the building blocks with their sizes as tunable parameters.

### 1.1.2. Catalytic application of Au nanoparticles and clusters

Gold is widely known as one of the most stable and chemically inert metals under ambient conditions, which prompts it to be used for jewelry and coins. Thus it has been believed for a long time that Au is catalytically inactive. Contrary to such a common belief, Haruta and co-workers discovered in 1987 that AuNPs smaller than ~5 nm in

diameter supported on metal oxides acted as catalysts for oxidation of carbon monoxide even at low temperature as low as −70ºC.[13] Later the dependence of the particles diameters on oxidation catalysis was studied.[14] Figures 1.3(a) and (b) show an image of transmission electron microscopy (TEM) for AuNPs supported on $TiO_2$ and the correlation between catalytic activity (turnover frequencies based on surface Au atoms) of AuNPs and their diameters, respectively. It was revealed that smaller NPs show much higher activity. This discovery stimulated the development of highly active Au catalysts. Until now, numbers of catalytic reactions by AuNPs have been reported, including oxidation, hydrogenation, water-gas shift, nucleophilic additions of organic molecules and so on.[15,16]

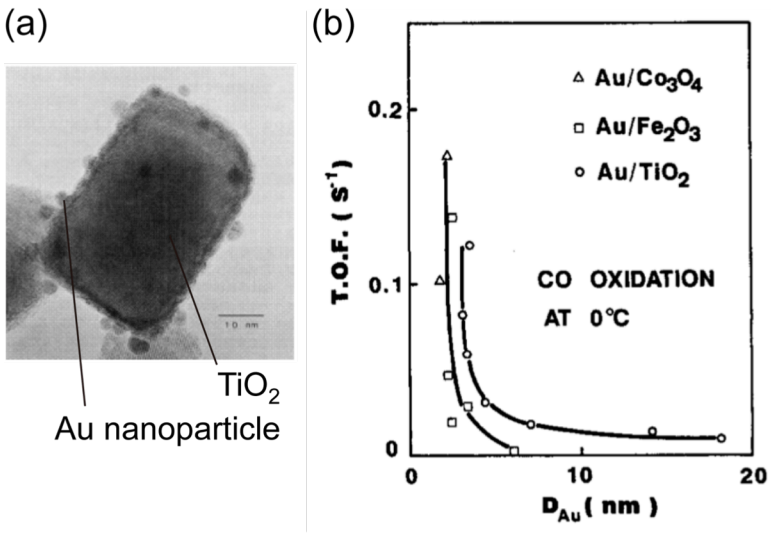


**Figure 1.3.** (a) TEM image of the $Au/TiO_2$ nanoparticle. The scale bar indicates 10 nm. (b) Turnover frequencies based on surface exposed gold atoms as a function of the mean diameters of gold in CO oxidation at 0ºC. Codes: triangle = $Au/Co_3O_4$, square = $Au/\alpha\text{-}Fe_2O_3$, circle = $Au/TiO_2$. Reprinted from ref. 14 with permission. 1997 Elsevier B. V.

Catalysis of the small Au clusters also has been extensively studied[17] and size-specific catalytic performances were revealed.[18,19] For example, Figure 1.4 shows the catalytic activity of $Au_n$ clusters with the atomically controlled sizes of $n$ = 10, 18, 25, 39, and ~85 supported on hydroxyapatite (HAP) for aerobic oxidation of cyclohexane.[20] The activity changes non-monotonously depending on the cluster size and shows a maximum at $n$ = 39, indicating the importance of the size control of the metal clusters at atomic level.

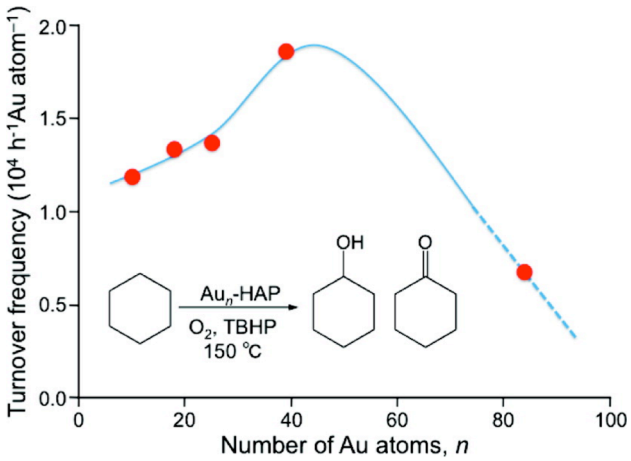


**Figure 1.4.** Turnover frequencies of Au clusters for aerobic oxidation of cyclohexane as a function of cluster size $n$. Reprinted from ref. 20 with permission. 2011 American Chemical Society.

### 1.1.3. Rational design of metal cluster catalysts

The discovery of Au catalysis by Haruta also led to fundamental studies on model systems to gain insights into size-specific catalysis. Previous experimental and theoretical studies on bare Au clusters with defined sizes and charge states revealed that

electronic structure not only governs its "magic" stability,[21–23] but also chemical reactivity with $O_2$, which is a key step of aerobic oxidation catalysis.[24–26] Figure 1.5(a) shows clear correlation between EA and reactivity toward $O_2$. The Au clusters with low

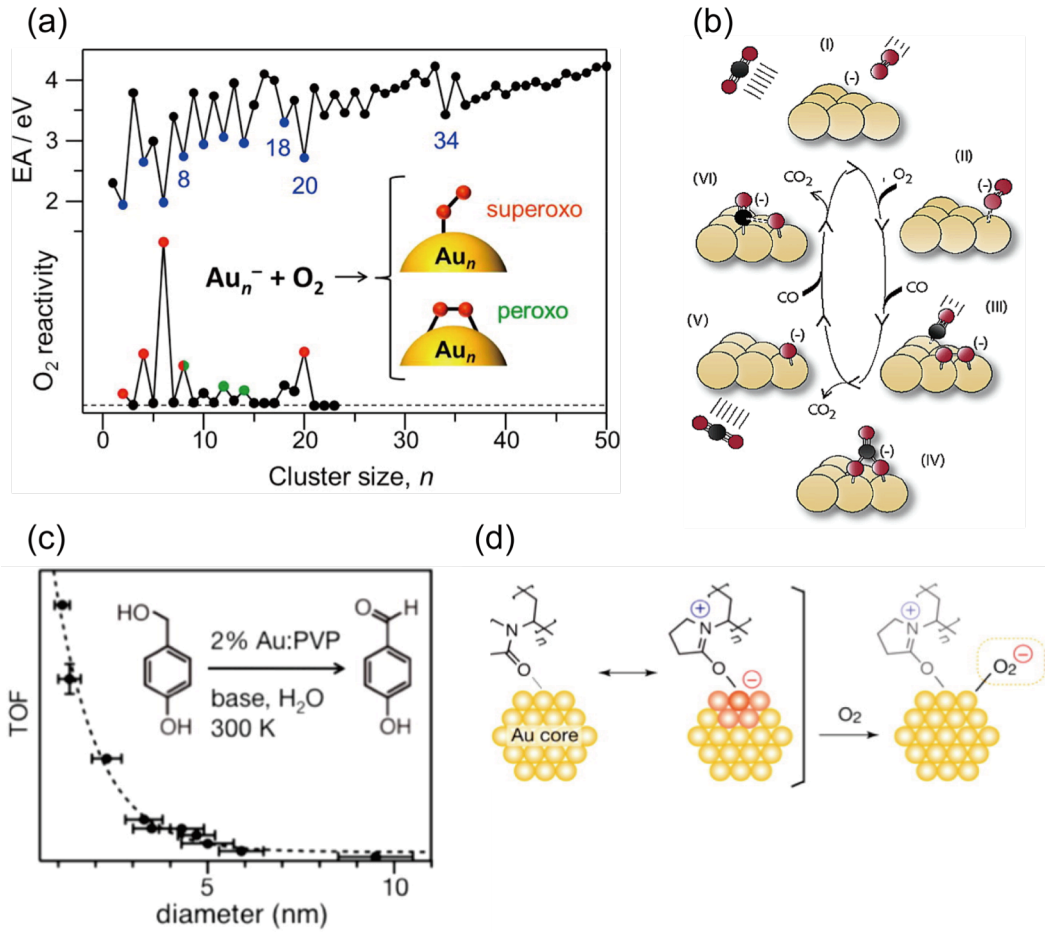


**Figure 1.5.** (a) Correlation between the EA of the $Au_n$ clusters and reactivity of $Au_n^-$ with $O_2$ in the gas phase. Red and green points indicate the cluster size where $O_2$ adsorbs $Au_n^-$ in a superoxo- and peroxo- form, respectively. (b) Schematic illustration of the reaction mechanism of $O_2$ with CO co-adsorbed on bare $Au_6^-$. (c) Dependence of the catalytic activity on the diameter of Au:PVP for the oxidation of 4-(hydroxymethyl)phenol. (d) Proposed mechanism for activation of $O_2$ by Au:PVP. Reprinted from ref. 18 with permission for (a), (c), (d). 2014 American Chemical Society. Reprinted from ref. 26 with permission for (b). 2002 American Chemical Society.

EA have high reactivity with $O_2$ when they are negatively charged. It indicates that $O_2$ is activated by electron transfer from the Au cluster anions, and that superoxo- or peroxo-like species thus formed oxidizes CO on the cluster surface.[27] For example, Figure 1.5(b) shows the proposed mechanism of CO oxidation on $Au_6^-$.[26] Although these results may not directly explain the origin of oxidation catalysis of Au catalysts in the real world[14–17,20,28–32] due to significant differences in the surrounding environments, they provide a design principle for Au-based oxidation catalysts; Au clusters must be sufficiently small and negatively charged for catalytic use in aerobic oxidation.[9]

Using this simple concept, oxidation catalysis of monodisperse Au clusters stabilized by polyvinylpyrrolidone (PVP) with various sizes has been studied.[18,33] Figure 1.5(c) shows that only small Au:PVP clusters with a diameter of 1–2 nm showed size-specific catalysis for aerobic oxidation of alcohols. Furthermore, the negative charge of Au core was revealed by Fourier transform infrared (FT-IR) spectroscopy on adsorbed CO, X-ray photoelectron spectroscopy (XPS) and X-ray absorption spectroscopy (XAS). From these results, the activation of $O_2$ through electron transfer by a negatively charged Au:PVP cluster is thought to be the key step in this oxidation (Figure 1.5(d)).[18,33] In other words, the key step for aerobic oxidation is closely similar for both bare and PVP-stabilized Au clusters. This correspondence demonstrates that metal cluster-based catalysts can be rationally designed and developed on the basis of guiding principles established using model catalytic systems.

## 1.2. Chemistry of atomic coinage metals

### 1.2.1. Isolated atomic coinage metals

As discussed in Section 1.1, metal clusters show size-specific physical and

chemical properties. In order to investigate such size dependency of the metal clusters, it is inevitably necessary to understand the properties at the small size limit, atoms. Especially investigations on isolated atoms in the gas phase will provide intrinsic properties of the elements. Chemical reactivity is one of the most important properties to be clarified for application as the catalysts. The gas phase reactions of atomic metal

**Table 1.1. Summary of Product Data for the Ion-Molecule Reactions of $Au^+$.[a]**

| ion + neutral reactants | primary products [assumed neutral] | secondary[a] products | fraction of product ion signal | estimated bond energy limit (kcal/mol) |
|---|---|---|---|---|
| $Au^+ + CH_4$ | → no reaction | | | |
| $Au^+ + CH_3CH_3$ | → $AuC_2H_4^+$ [+ $H_2$] | | 1.00 | $D°(Au^+–C_2H_4) > 32.7$ |
| $Au^+ + CH_3CH_2CH_3$ | → $C_3H_7^+$ [+ AuH] | | 0.93 | $D°(Au–H) > 54.3$ |
| | → $AuC_3H_6^+$ [+ $H_2$] | | 0.07 | |
| $Au^+ + (CH_3)_3CH$ | → $(CH_3)_3C^+$ [+ AuH] | | 0.99 | $D°(Au–H) > 56$ |
| | → $AuC_4H_8^+$ [+ $H_2$] | | 0.01 | |
| $Au^+ + (CH_3)_4C$ | → $(CH_3)_3C^+$ [+ $AuCH_3$] | | 1.00 | $D°(Au–CH_3) > 31$ |
| $Au^+ + CH_3(CH_2)_3CH_3$ | → $C_5H_{11}^+$ [+ AuH] | $C_3H_7^{+*}$ | 0.99 | |
| | → $AuC_5H_{10}^+$ [+ $H_2$] | | 0.01 | |
| $Au^+ + CH_3(CH_2)_4CH_3$ | → $C_6H_{13}^+$ [+ AuH] | $C_3H_7^{+*}$, $C_4H_9^{+*}$ | 0.99 | |
| | → $AuC_6H_{12}^+$ [+ $H_2$] | | 0.01 | |
| $Au^+ + CH_3(CH_2)_5CH_3$ | → $C_7H_{15}^+$ [+ AuH] | $C_4H_9^{+*}$ | 0.99 | |
| | → $AuC_7H_{14}^+$ [+ $H_2$] | | 0.01 | |
| $Au^+ + c\text{-}C_3H_6$ | → $C_3H_5^+$ [+ AuH] | $C_4H_7^{+*}$ | 0.73 | |
| |  | | 0.27 | |
| $Au^+ + c\text{-}C_5H_{10}$ | → $C_5H_9^+$ [+ AuH] | | 0.98 | $D°(Au–H) > 61.7$ |
| |  | | 0.01 | |
| | 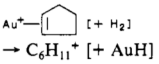 | | 0.01 | |
|  | → $C_6H_{11}^+$ [+ AuH] | | 0.99 | $D°(Au–H) > 60.4$ |
| | → $Au^+$ [+ $H_2$] | | 0.01 | |
| $Au^+ + CH_2{=}CH_2$ | → $AuC_2H_4^+$ | $AuC_4H_8^+$ | 1.00 | |
| $Au^+ + CH_3CH{=}CH_2$ | → $C_3H_5^+$ [+ AuH] | $C_4H_7^+$ | 0.85 | $D°(Au–H) > 62.9$ |
| | → $AuC_3H_6^+$ | $AuC_6H_{12}^+$ | 0.15 | |
| $Au^+ + C_6H_6$ | → $C_6H_6^+$ [+ Au] | | 0.06 | |
| | → $AuC_6H_6^+$ | $Au^+(C_6H_6)_2^+$ | 0.94 | |
| $Au^+ + C_6H_5CH_3$ | → $C_{H5}CH_3^+$ | | 0.83 | |
| | → $C_7H_7^+$ [+ AuH] | | 0.16 | $D°(Au–H) > 54.8$ |
| | → $AuC_7H_8^+$ | | 0.01 | |
| $Au^+ + C_6H_5CH_2CH_3$ | → $C_6H_5CH_2^+$ [+ $AuCH_3$] | | 0.02 | $D°(Au–CH_3) > 38.6$ |
| | → $C_6H_5C_2H_5^+$ [+ Au] | | 0.41 | |
| | → $C_6H_5C_2H_4$ [+ AuH] | | 0.41 | |
| | → $AuC_2H_4^+$ [+ $C_6H_6$] | | 0.08 | |
| | → $AuC_6H_6^+$ [+ $AuC_2H_4$] | | 0.05 | |
| | → $AuC_8H_{10}^+$ | | 0.03 | |
| $Au^+ + CH_3Cl$ | → $AuCH_2^+$ [+ HCl] | $AuC_2H_4^+$, $AuC_2H_4(CH_3Cl)^+$ | 0.94 | $D°(Au^+–CH_2) > 89.6$ |
| | → $Au(CH_3Cl)^+$ | $Au(CH_3Cl)_2^+$ | 0.06 | |
| $Au^+ + CH_3Br$ | → $AuCH_2^+$ [+ HBr] | $AuC_2H_4^+$, $AuC_2H_4(CH_3Br)^+$ | 0.70 | $D°(Au^+–CH_2) > 92.4$ |
| | → $Au(CH_3Br)^+$ | $Au(CH_3Br)_2^+$ | 0.29 | |
| | → $H_2CBr^+$ [+ AuH] | | 0.01 | $D°(Au–H) > 66.8$ |
| $Au^+ + CH_3I$ | → $AuCH_2^+$ [+ HI] | | 0.06 | $D°(Au^+–CH_2) \geq 95.0$ |
| | → $AuCH_3^+$ [+ I] | | 0.21 | $D°(Au^+–CH_3) > 56$ |
| | → $Au(CH_3I)^+$ | | 0.11 | |
| | → $AuI^+$ [+ $CH_3$] | | 0.52 | $D°(Au^+–I) > 56$ |
| | → $CH_2I^+$ [+ AuH] | | 0.10 | $D°(Au–H) > 65.9$ |
| $Au^+ + CH_3CN$ | → $Au(CH_3CN)^+$ | $Au(CH_3CN)_2^+$ | 1.00 | |
| $Au^+ + CHBr_3$ | → $CHBr_2^+$ [+ AuBr] | | 1.00 | $D°(Au–Br) > 36.3$ |
| $Au^+ + CCl_4$ | → $CCl_3^+$ [+ AuCl] | | 1.00 | $D°(Au–Cl) > 60.2$ |

[a] Secondary products with asterisk are unimolecular decomposition products. Reprinted from ref. 37 with permission. 1987 American Chemical Society.

ions and small molecules have been intensively studied.[34–36] The first report on Au ions dates back to late 1980s when Wilkins investigated the reaction of $Au^+$ with various small molecules including hydrocarbons and alkyl halides in the gas phase by means of Fourier transform ion cyclotron resonance mass spectrometry (FT-ICR-MS) as summarized in Table 1.1.[37] For example, the reactions with alkanes except methane and ethane predominantly exhibited hydride abstraction to form AuH, in competition with dehydrogenation. The reaction with $CH_3X$ (X = Cl, Br) mainly gave a gold-carbene complex $AuCH_2^+$ and an association product $Au(CH_3X)^+$. The reaction of $Au^-$ was not investigated intensively because of low reactivity. Taylor and co-workers further studied electronic state-resolved reaction of $Au^+$ with $CH_3X$ using a chromatographic technique,[38,39] and found that the electronic state of $Au^+$ greatly affects the reaction channels; $Au^+(^1S)$ typically undergoes elimination of HX leaving $AuCH_2^+$, whereas the reaction of $Au^+(^3D)$ results in other processes.

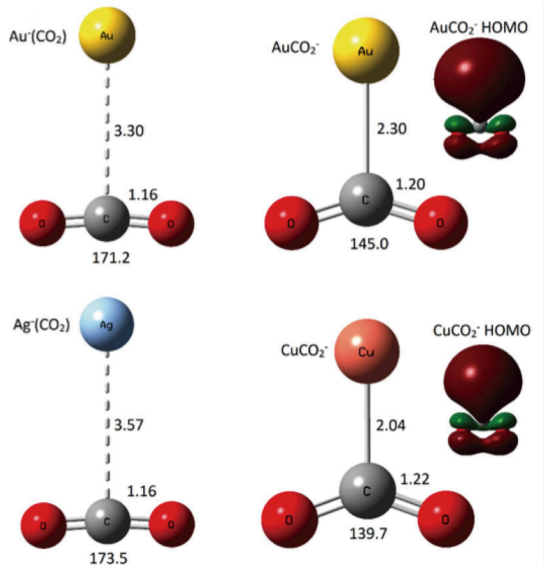


**Figure 1.6.** Calculated structures of chemisorbed and physisorbed $AuCO_2^-$, physisorbed $AgCO_2^-$, and chemisorbed $CuCO_2^-$. Bond distances and angles are shown in Å and degree, respectively. HOMOs of $AuCO_2^-$ and $CuCO_2^-$ are also presented. Reprinted from ref. 43 with permission. 2015 American Institute of Physics.

Au atom has an electronic configuration of $[Xe](4f)^{14}(5d)^{10}(6s)^1$: fully occupied d orbitals and a singly occupied s orbital similar to other coinage metals, silver (Ag)

and copper (Cu). Thus, the chemistry of Au, Ag, and Cu is often compared.[21,24,40–42] An example is reactions of $CO_2$ with $M^-$ (M = Cu, Ag, and Au),[43] studied by Bowen and co-workers. Photoelectron spectroscopy on the products $MCO_2^-$ revealed that $AuCO_2^-$ forms both chemisorbed and physisorbed isomers as shown in Figure 1.6. On the other hand, $AgCO_2^-$ and $CuCO_2^-$ forms only the physisorbed and the chemisorbed ones, respectively, showing the different reactivity among the coinage metals. The difference in product structures among coinage metal anions can also be seen in the reactions with $H_2O$ molecules, reported by Weber and co-workers.[44] Such examples provide the possibility of activity-control of the catalysts by the alternation of elements in the same group.

### 1.2.2. Single atom catalysts

Recently, metal atoms dispersed on solid supports, such as metal oxides, metal surfaces, and graphenes, have gained much attention as novel catalysts due to the maximized utilization efficiency of the metal atoms.[45,46] In 2011, Liu, Li, Zhang, and co-workers found that single Pt atoms supported on surfaces of iron oxide ($FeO_x$) nanocrystallites ($Pt_1/FeO_x$) exhibit quite high activity and stability for CO oxidation.[47] Such atomically-dispersed metal catalysts were named "single atom catalysts (SACs)" and this concept has been applied to other metals (e.g. Ir[48]). Gold is also a good candidate as SAC and several Au SAC have been developed including $Au_1/ZnO$ for methanol steam reforming reaction,[49] $Au_1M'$/zeolite (M' = Na or K) for water-gas shift reaction,[50] $Au_1$/ZnZrO for ethanol dehydrogenation,[51] and $Au_1/FeO_x$[52] and $Au_1/CeO_x$ (Figure 1.7)[53] for CO oxidation. Exploration of atom chemistry is expected to provide not only a benchmark for the cluster chemistry, but also key insights into development

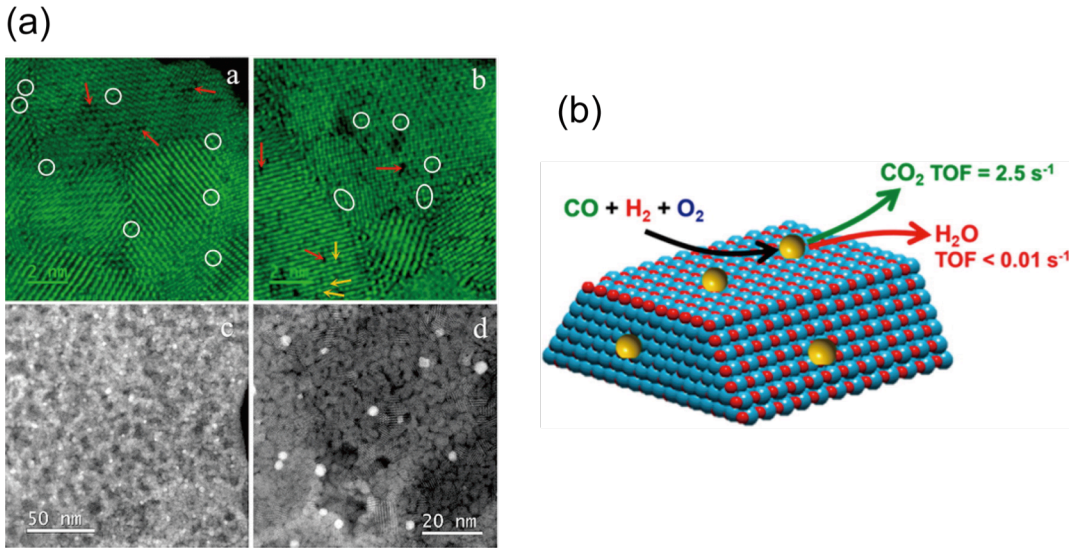


**Figure 1.7.** (a) High-angle annular dark-field scanning transmission electron microscopy (HAADF-STEM) images of $Au_1/CeO_x$ SAC (a, b; scale bar = 2 nm) and those of Au nanoparticle/$CeO_x$ (c, d; scale bars = 50 nm and 20 nm). White circles represent single Au atoms. Red arrows represent Ce vacancies of the support. (b) Graphical image of $Au_1/CeO_x$ SAC and its selective catalytic activity for CO oxidation. Reprinted from ref. 53 with permission. 2015 American Chemical Society.

of the single atom catalysts.

## 1.3. Carbon–halogen bond activation

The catalytic carbon−carbon (C−C) bond-forming reaction is one of the most useful transformations in synthetic chemistry for constructing a variety of carbon frameworks of target molecules. The C–C bond-forming reaction has been intensively studied since 1970s. Numbers of reactions established so far include Negishi,[54,55] Suzuki-Miyaura,[56,57] and Mizirogi-Heck coupling reactions,[58,59] for which Nobel Prize in Chemistry was awarded in 2010. Typical catalytic cycles of the C–C bond formation are composed of oxidative addition of organohalides R–X on organometallic catalysts,

transmetalation of R'Y to eliminate XY and reductive elimination of R–R' from the catalysts (Scheme 1.1).[60] Especially the oxidative addition process plays important roles as an initial step of the C–C bond formations, and corresponds to a rate determining step in many cases.[61]

**Scheme 1.1. Formal Catalytic Cycle of C–C Bond Formation Using Organohalide (R–X) as Substrates.**[60]

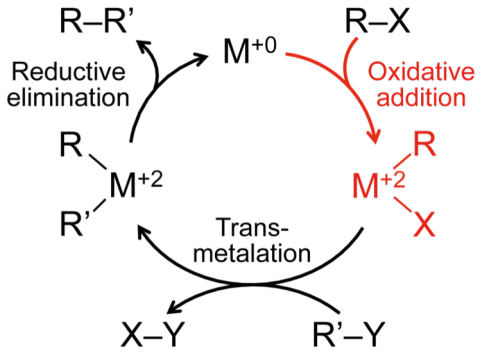


Recently, it has been reported that AuNPs and Au clusters catalyze a variety of C–C bond-formations[62] such as Suzuki-Miyaura,[63] Sonogashira,[64,65] and Ullmann reactions.[66] Scheme 1.2 shows the first report on Suzuki-Miyaura reaction catalyzed by poly 2-aminothiophenol (PATP)-stabilized Au clusters (Figure 1.8). These findings suggest that C(sp or $sp^2$)–X bonds can be activated by Au catalysts via oxidative addition. However, catalytic activation of C($sp^3$)–X bonds has been considered to be challenging due to the more electron-rich nature of the $sp^3$ carbons.[67] The oxidative addition process requires oxidation of the metal center, which simply indicates electron transfer from metal to substrate is necessary. It is expected that atoms or clusters of Au should have a potential to activate C($sp^3$)–X bond intrinsically via electron transfer in a similar manner to $O_2$

**Scheme 1.2. Suzuki-Miyaura Coupling of Chlorobenzene and Phenylboronic Acid Catalyzed by PATP-Stabilized Au Cluster.**[63]

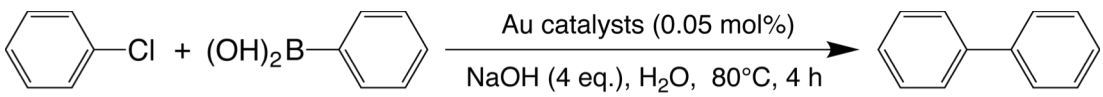

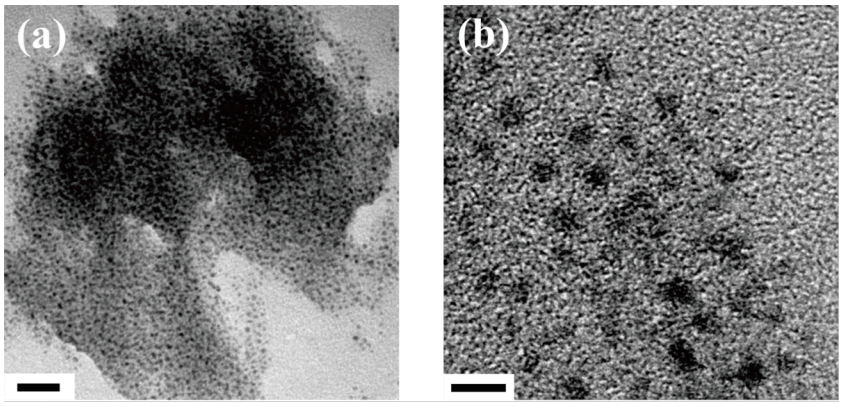


**Figure 1.8.** (a) TEM and (b) high-resolution (HR)-TEM images of PAPT-stabilized Au clusters. Scale bar: (a) 20 nm and (b) 4 nm. Reprinted from ref. 63 with permission. 2013 American Chemical Society.

activation (Section 1.1.3).

## 1.4. Experimental and theoretical techniques to study isolated systems

### 1.4.1. Mass spectrometry

As exemplified in Section 1.1.3, understanding of the chemical properties of model systems will provide guiding principles for rational design of the catalysts. Especially, investigations on isolated systems in the gas phase are expected to unravel their intrinsic properties without any perturbations from the surroundings, such as solvents, protecting ligands or supports.

The progress in a research field of gas phase reaction has been closely linked to development of mass spectrometric techniques.[24–27,37–44] Mass spectrometry (MS) is an analytical method to determine the mass-to-charge ratio ($m/z$) of ionic species.[68] Thus MS directly provides us the information of mass numbers or chemical compositions of

the reaction intermediates and products. The first mass spectra ("mass spectrograph") was recorded by Thomson in 1911.[69] Since then several types of MS based on different principles to separate the species with their *m*/*z* values have been developed. Table 1.2 lists the typical mass spectrometries usually used to investigate gas phase reactions.[68] Among others, time-of-flight (TOF)-MS (Figure 1.9), which is used in Chapters 2, 3, and 5, has following advantages:[68] (1) it is compatible with pulsed ion generation techniques, such as laser ablation methods, since the mass-analysis is conducted in pulses, (2) acquisition rate and high dynamic range are large since all the species generated in one pulse can be mass-analyzed in one pulse, (3) there is no limitation in principle on the detectable mass range, and (4) it can be designed and constructed easier and with lower cost as compared to other methods. TOF-MS was intensively developed and spread thanks to the improvement of mass-resolution according to a report by Wiley

**Table 1.2. Typical Mass Spectrometries and the Principles to Analyze Mass-to-Charge Ratio (*m*/*z*) Values.**

| Mass spectrometer | Principles |
|---|---|
| Quadrupole (Q)-MS | Difference in conditions of radio frequency electric fields in which ions can pass through. |
| Time-of-flight (TOF)-MS | Difference in times-of-flight of ions to pass through a constant distance with a constant kinetic energy. |
| Fourier transformed ion cyclotron resonance (FT-ICR)-MS | Difference in cyclotron resonant frequency (or Lorentz force) of ions in a constant magnetic field. |

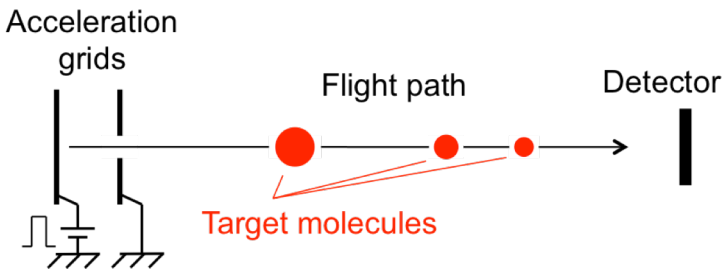


**Figure 1.9.** Schematic image of principle of TOF-MS.[67]

and McLaren,[70] which is discussed in detail in Chapter 2. MS has still been developed in these days, especially as a powerful tool to study large bio-molecules. Mass-resolution is still being improved ($m/\Delta m$ > 100,000),[71] and new MSs such as Orbitrap-MS[72] and nano-electromechanical systems (NEMS)-MS[73] have been developed recently.

### 1.4.2. Anion photoelectron spectroscopy

The electronic structures of target compounds can be studied by photoelectron spectroscopy (PES). When a substrate is irradiated with light with sufficient energy, an electron is ejected from the substrate due to photoelectric effect. By measuring the kinetic energy of the photoelectron ($E_K$), the electron binding energy ($E_B$) of this substrate can be determined based on the energy conservation law shown in eq. 1.2.

$$E_B = h\nu - E_K \tag{1.2}$$

where $h\nu$ represents photon energy of the light. In contrast to conventional optical absorption spectroscopy which determines the gaps between the energy levels, PES

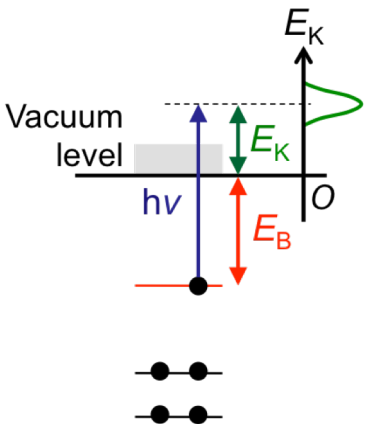


**Figure 1.10.** Schematic image of principle of photoelectron spectroscopy.

provides density of states of energy levels with respect to the vacuum level (Figure 1.10), which can be straightforwardly compared to theoretical calculations in many cases.

X-ray PES (XPS) developed by Siegbahn in 1957[74] determines binding energies of inner shell electrons. In contrast, ultraviolet PES (UPS), whose first report dates back to 1962 by Turner,[75] gives us the information of valence electrons, which is essential for chemical reactions. After these developments, PES has been applied to various samples including solids and gaseous molecules. By combining this technique to TOF-MS described above, it is possible to conduct PES on mass-separated ion beams. Especially since anions can be photodetached by visible or UV light, anion PES has been intensively studied using laser as the detachment light.[21,23,27,41,43]

As energy analyzers of anion PES, hemispherical electrostatic energy analyzer was mainly used at the beginning.[75,76] In 1984, Kruit and Read developed a magnetic bottle energy analyzer.[77] Three years later, Smalley and co-workers combined the magnetic bottle with TOF-MS,[78] which corresponds to the origin design of the PE spectrometer

used in Chapters 2 and 3. Smalley and co-workers then determined the EAs of coinage metal clusters with various sizes using TOF-MS-PES technique.[21] Their study finally played an essential role in elucidating the key step in $O_2$ activation by Au cluster anions as discussed in Section 1.1.3.[18]

As described above, anion PES is usually combined with TOF-MS. Since TOF-MS provides only chemical compositions of target molecules, in case structural isomers are contained in the sample we cannot distinguish them. However, if electronic structures sensitively change depending on geometric structures, PES is a promising method to determine the geometric structures.[79,80]

Recent development of PES includes velocity map imaging energy analyzer; it enabled us to obtain the information of angular momentum of the molecular orbitals.[81,82]

### 1.4.3. Matrix-isolation

Matrix-isolation technique is another method to study the isolated systems.[83] In this method, target species, including both neutral and ionic compounds, are trapped in inert matrix molecules such as $N_2$, Ne, and Ar, which are cooled down to several K, as schematically shown in Figure 1.11.[84] Owing to inertness of the matrix molecules, the reactive species such as reaction intermediates can be trapped, which enables us to probe the chemical reactions in detail. Since the matrices are at cryogenic temperature, the trapped species are vibrationally and rotationally in the ground state. Thus spectroscopy on matrix-isolated species, for example infrared (IR) spectroscopy, generally gives less structured and sharp signals, which is often directly compared to theoretical calculations for unambiguous assignments. An important advantage of the

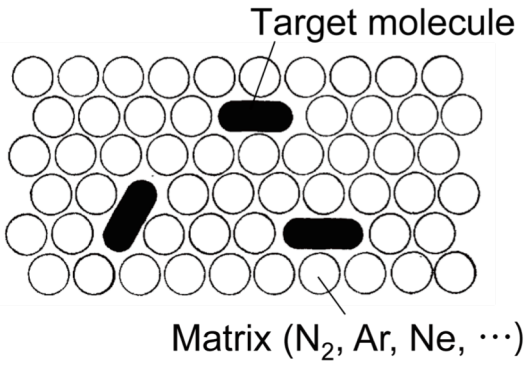


**Figure 1.11.** Schematic image of matrix-isolation technique. Reprinted from ref. 84 with permission.

matrix-isolation is that absorption spectroscopy of the isolated species can be conducted, which is not the case in the gas phase experiments where the density of target species is so low that action spectroscopy such as photo-dissociation spectroscopy has been intensively studied.[85–87]

The first report of matrix isolation spectroscopy dates back to 1954 reported by Pimentel and co-workers.[88] Since then, this technique was spread to many researchers. Especially Andrews and co-workers has been quite intensively studying the chemical reactions of metal atoms with organic molecules by combining the matrix-isolation technique with laser-ablation method to generate various kinds of metal atoms.[83,89]

### 1.4.4. Global reaction route mapping

In order to describe how a reaction proceeds, a concept "intrinsic reaction coordinate (IRC)" is helpful.[90] It was proposed by Fukui in 1970,[91] who was awarded for Nobel Prize in Chemistry in 1981. When we consider the potential energy surface of a reacting system, IRC corresponds to mass-weighted steepest descend path starting from a first-order saddle point on the potential energy surface. The saddle point

corresponds to a transition state (TS). The IRC shows representative reaction paths where no vibrations and rotations of the reacting system are assumed.[90]

Calculation of an IRC requires finding of a corresponding TS beforehand, which is greatly challenging. Although various methods have been developed to find TSs,[92] a good initial guess is necessary to let the calculation successfully converge to appropriate TSs. This situation hampers the discovery of novel reaction pathways based on the exploration of IRCs.

In 2004, Ohno and Maeda made a breakthrough in finding TSs or dissociation channels (DC) from a local minimum (LM) of the potential energy surface by means of a scaled hypersphere search (SHS) method.[93] The "guidepost"[94] for the calculation was a harmonic downward distortion (ADD), a potential energy lowering with respect to a harmonic potential, as shown in Figure 1.12.[95] By following ADDs from a LM structure,

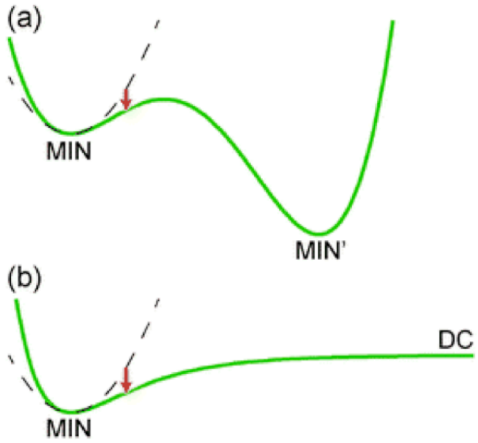


**Figure 1.12.** Schematic potential curves (solid line) and ADDs (red arrow) from the harmonic potential. A word "MIN" is used in the same meaning as LM in a text. (a) Along an isomerization path toward another MIN (MIN'). (b) Along a dissociation path toward a dissociation channel (DC). Reprinted from ref. 95 with permission. 2015 PCCP Owner Societies.

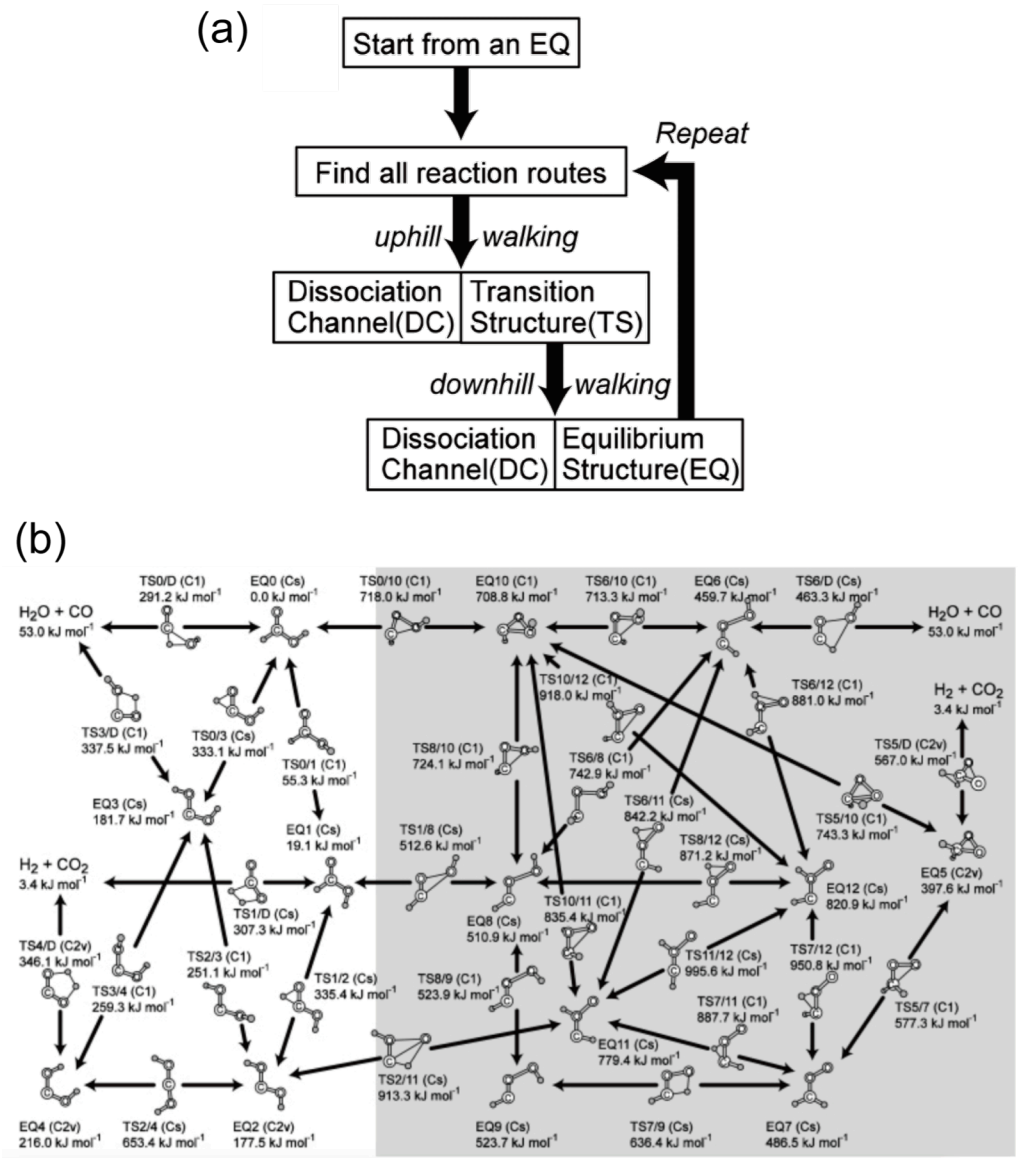


**Figure 1.13.** (a) An algorithm of global reaction route mapping. Uphill walking corresponds to ADDF calculations, and downhill walking corresponds to IRC calculations. A word "EQ" is used in the same meaning as LM in a text. The procedures can be repeated within finite processes until no new EQ is found. (b) Global reaction route map of $H_2CO_2$. Structures related to higher energy isomers are shaded in gray. Relative energies are shown with respect to the most stable isomer ($EQ_0$). The point group is shown in parentheses. Reaction routes (IRC) are shown by arrows with a direction TS → EQ. Reprinted from ref. 98 with permission. 2006 American Chemical Society.

they finally succeeded in obtaining approximate TSs systematically. This approach was named ADD following (ADDF) method. Since computational technique of IRC from a TS is well established,[96,97] which finally finds new LM structures, ADDF calculation can be repeated automatically until no new LM structure is found anymore (Figure 1.13(a)). It enables us to find all LMs and TSs once one chemical formula is given. It was named "Global reaction route mapping (GRRM)". Figure 1.13(b) shows an example of the global reaction route map.[98]

Until now, another TS-search technique called artificial force induced reaction (AFIR) method has also been developed.[99] The GRRM calculations has been widely and rapidly spread as a powerful tool to explore novel reaction pathways.

## 1.5. Aim and outline of the thesis

Coinage metals including Au are promising elements for novel catalysts. Especially AuNPs and Au clusters have been intensively developed as oxidation catalysts from both practical and fundamental aspects. Activation of C–X (X: halogen) bond via oxidative addition is another important reaction, which is often required in C–C bond-forming reaction, a fundamental process in organic synthesis. Although recent studies revealed that C(sp or $sp^2$)–X bonds can undergo the oxidative addition to AuNPs and Au clusters, catalytic activation of C($sp^3$)–X bonds of haloalkanes by coinage metal cluster catalysts has not been achieved yet.

The aim of the present work is to gain clues for further development of coinage metal catalysts for C–X bond activation. Especially, in order to rationally develop the cluster-based catalysts, a fundamental study on model catalytic systems to extract key factors in the reaction is a promising way thanks to the development in experimental

and theoretical techniques to study the isolated chemical systems. In this thesis, I investigate chemical reactions of the simplest haloalkane, methyl iodide ($CH_3I$), toward bare atomic coinage metals and small clusters to reveal whether they intrinsically have a potential to activate $C(sp^3)$–I bonds and to elucidate key properties to promote the oxidative addition. In Chapter 2, I investigate a reaction of $CH_3I$ with atomic $Au^-$ anion isolated in the gas phase, which affords the oxidative addition product $[CH_3–Au–I]^-$. I discuss the mechanism of this reaction and a possibility of successive C–C bond-forming reaction by the oxidative addition product $[CH_3–Au–I]^-$. In Chapter 3, I test the scope of the reaction to other coinage metals, Cu and Ag, and compare the thermodynamic stabilities of the oxidative addition products. In Chapter 4, I examine the reaction of $CH_3I$ with atomic Au in low-temperature Ne matrix, to examine the effect of the difference in charge state and the environment. Another purpose of this study is to directly observe the C–C bond formation product in neutral charge, which is difficult to detect in the gas phase system. In Chapter 5, I study the gas phase reaction of $CH_3I$ with small Au cluster anions, $Au_n^-$ ($n$ = 1–4), to examine the cluster size effect. I mainly discuss the reactivity of $Au_2^-$, which has the highest reactivity among $Au_n^-$ ($n$ = 1–4), focusing on the difference from $Au^-$ (Chapter 2) to reveal the factor which determines the preferential reaction mechanisms. In Chapter 6, I summarize the present work and discuss the future prospects as a concluding remark.

## References


1. Feynman, R. P. *Engineering and Science* **1960**, *23*, 22.
2. Daniel, M. C.; Astruc, D. *Chem. Rev.* **2004**, *104*, 293–346.
3. Wagner, F. E.; Haslbeck, S.; Stievano, L.; Calogero, S.; Pankhurst, Q. A.; Martinek, K. P. *Nature* **2000**, *407*, 691–692.
4. Shimizu, T.; Teranishi, T.; Hasegawa, S.; Miyake. M. *J. Phys. Chem. B* **2003**, 107, 2719–2724.
5. Buffat, P; Borel, J. P. *Phys. Rev. A* **1976**, *13*, 2287-2298.
6. Schmidt, M.; Kusche, R.; Kronmüller, W.; von Issendorff, B.; Haberland, H. *Phys. Rev. Lett.* **1997**, *79*, 99–102.
7. Iijima, S; Ichihashi, T. *Phys. Rev. Lett.* **1986**, *56*, 616–619.
8. Brack, M. *Rev. Mod. Phys.* **1993**, *65*, 677–732.
9. Tsukuda, T. *Bull. Chem. Soc. Jpn.* **2012**, *85*, 151–168.
10. Kubo, R. *J. Phys. Soc. Jpn.* **1962**, *17*, 975–986.
11. Negishi, Y.; Nakazaki, T.; Malola, S.; Takano, S.; Niihori, W.; Kurashige, W.; Yamazoe, S.; Tsukuda, T.; Häkkinen, H. *J. Am. Chem. Soc.* **2015**, *137*, 1206−1212.
12. Negishi, Y; Nobusada, K.; Tsukuda, T. *J. Am. Chem. Soc.* **2005**, *127*, 5261–5270.
13. Haruta, M.; Kobayashi, T.; Sano, H.; Yamada, N. *Chem. Lett.* **1987**, 405–408.
14. Haruta, M. *Catal. Today* **1997**, *36*, 153–166.
15. Corma, A.; Serna, P. *Science* **2006**, *313*, 332–334.
16. Hashmi, A. S. K.; Hutchings, G. J. *Angew. Chem., Int. Ed.* **2006**, *45*, 7896–7936.
17. Lewis, L. N. *Chem. Rev.* **1993**, *93*, 2693–2730.
18. Yamazoe, S.; Koyasu, K.; Tsukuda, T. *Acc. Chem. Res.* **2014**, *47*, 816–824.
19. Yamazoe, S.; Yoskamtorn, T.; Takano, S.; Yadnum, S.; Limtrakul, J.; Tsukuda, T. *Chem. Rec.* **2016**, *16*, 2338–2348.
20. Liu, T.; Tsunoyama, H.; Akita, T.; Xie, S.; Tsukuda, T. *ACS Catal*. **2011**, *1*, 2–6.
21. Taylor, K. J.; Pettiette-Hall, C. L.; Cheshnovsky, O.; Smalley, R. E. *J. Chem. Phys.* **1992**, *96*, 3319–3329.
22. de Heer, W. A. *Rev. Mod. Phys.* **1993**, *65*, 611–676.
23. Wang, L. M.; Wang, L. S. *Nanoscale* **2012**, *4*, 4038–4053.
24. Bernhardt, T. M. *Int. J. Mass Spectrom.* **2005**, *243*, 1–29.
25. Yoon, B.; Koskinen, P.; Huber, B.; Kostko, O.; von Issendorff, B.; Häkkinen, H.; Moseler, M.; Landman, U. *ChemPhysChem* **2007**, *8*, 157–161.
26. Wallace, W. T.; Whetten, R. L. *J. Am. Chem. Soc.* **2002**, *124*, 7499–7505.
27. Pal, R.; Wang, L. M.; Pei, Y.; Wang, L. S.; Zeng, X. C. *J. Am. Chem. Soc.* **2012**,

*134*, 9438–9445.
28. Della Pina, C.; Falletta, E.; Prati, L.; Rossi, M. *Chem. Soc. Rev.* **2008**, *37*, 2077–2095.
29. Corma, A.; Garcia, H. *Chem. Soc. Rev.* **2008**, *37*, 2096–2126.
30. Fierro-Gonzalez, J. C.; Gates, B. C. *Chem. Soc. Rev.* **2008**, *37*, 2127–2134.
31. Takei, T.; Akita, T.; Nakamura, I.; Fujitani, T.; Okumura, M.; Okazaki, K.; Huang, J.; Ishida, T.; Haruta, M. *Adv. Catal.* **2012**, *55*, 1–126.
32. Zhang, Y.; Cui, X.; Shi, F.; Deng, Y. *Chem. Rev.* **2012**, *112*, 2467–2505.
33. Tsunoyama, H.; Ichikuni, N.; Sakurai, H.; Tsukuda, T. *J. Am. Chem. Soc.* **2009**, *131*, 7086–7093.
34. Squires, R. R. *Chem. Rev.* **1987**, *87*, 623−646.
35. Eller, K.; Schwarz, H. *Chem. Rev.* **1991**, *91*, 1121−1177.
36. Zhao, X.; Koyanagi, G. K.; Bohme, D. K. *J. Phys. Chem. A* **2006**, *110*, 10607−10618.
37. Chowdhury, A. K.; Wilkins, C. L. *J. Am. Chem. Soc.* **1987**, *109*, 5336–5343.
38. Taylor, W. S.; May, J. C.; Lasater, A. S. *J. Phys. Chem. A* **2003**, *107*, 2209–2215.
39. Taylor, W. S.; Matthews, C. C.; Hicks, A. J.; Fancher, K. G.; Chen, L. C. *J. Phys. Chem. A* **2012**, *116*, 943–951.
40. Häkkinen, H.; Moseler, M.; Landman, U. *Phys. Rev. Lett.* **2002**, *89*, 033401.
41. Kim, Y. D. *Int. J. Mass Spectrom.* **2004**, *238*, 17–31.
42. Roithová, J.; Schröder, D. *Coord. Chem. Rev.* **2009**, *253*, 666−677.
43. Zhang, X.; Lim, E.; Kim, S. K.; Bowen, K. H. *J. Chem. Phys.* **2015**, *143*, 174305.
44. Schneider, H.; Boese, A. D.; Weber, J. M. *J Chem. Phys.* **2005**, *123*, 84307.
45. Yang, X.; Wang, A.; Qiao, B.; Li, J.; Liu, J.; Zhang, T. *Acc. Chem. Res.* **2013**, *46*, 1740−1748.
46. Liu, J. *ACS Catal.*, **2017**, *7*, 34–59.
47. Qiao, B.; Wang, A.; Yang, X.; Allard, L. F.; Jiang, Z.; Cui, Y.; Liu, J.; Li, J.; Zhang, T. *Nat. Chem.* **2011**, *3*, 634–641.
48. Lin, J.; Wang, A.; Qiao, B.; Liu, X.; Yang, X.; Wang, X.; Liang, J.; Li, J.; Liu, J.; Zhang, T. *J. Am. Chem. Soc.* **2013**, *135*, 15314.
49. Gu, X. K.; Qiao, B. T.; Huang, C. Q.; Ding, W. C.; Sun, K. J.; Zhan, E. S.; Zhang, T.; Liu, J. Y.; Li, W. X. *ACS Catal.* **2014**, *4*, 3886–3890.
50. Yang, M.; Li, S.; Wang, Y.; Herron, J. A.; Xu, Y.; Allard, L. F.; Lee, S.; Huang, J.; Mavrikakis, M.; Flytzani-Stephanopoulos, M. *Science* **2014**, *346*, 1498–1501.
51. Wang, C.; Garbarino, G.; Allard, L. F.; Wilson, F.; Busca, G.; Flytzani-Stephanopoulos, M. *ACS Catal.* **2016**, *6*, 210–218.

52. Qiao, B.; Liang, J. X.; Wang, A.; Xu, C. Q.; Li, J.; Zhang, T.; Liu, J. J. *Nano Res.* **2015**, *8*, 2913–2924.
53. Qiao, B.; Liu, J.; Wang, Y. G.; Lin, Q.; Liu, X.; Wang, A.; Li, J.; Zhang, T.; Liu, J. *ACS Catal.* **2015**, *5*, 6249–6254.
54. King, A. O.; Okukado, N.; Negishi, E. *J. Chem. Soc., Chem. Commun.* **1977**, 683–684.
55. Negishi, E.; King, A. O.; Okukado, N. *J. Org. Chem.* **1977**, *42*, 1821–1823.
56. Miyaura, N.; Suzuki, A. *J. Chem. Soc., Chem. Commun.* **1979**, 866–867.
57. Miyaura, N.; Yamada, K.; Suzuki, A. *Tetrahedron Lett.* **1979**, *20*, 3437–3440.
58. Mizoroki, T.; Mori, K.; Ozaki, A. *Bull. Chem. Soc. Jpn.* 1971, 44, 581.
59. Heck, R. F.; Nolley, Jr., J. P. *J. Org. Chem.* **1972**, *37*, 2320–2322.
60. Hartwig, J. F. *Organotransition Metal Chemistry: From Bonding to Catalysis*; University Science Books: California, 2010.
61. Stille, J. K.; Lau, K. S. Y. *Acc. Chem. Res.* **1977**. *10*, 434.
62. Li, G. Jin, R. *Nanotechnol. Rev.* **2012**, *2*, 529–545.
63. Han, J.; Liu, Y.; Guo, R. *J. Am. Chem. Soc.* **2009**, *131*, 2060–2061.
64. Karimi, B.; Esfahani, F. K. *Chem. Commun.* **2011**, *47*, 10452–10454.
65. Kyriakou, G.; Beaumont, K. S.; Humphrey, S. M.; Antonetti, C.; Lambert, R. M. *ChemCatChem* **2010**, *2*, 1444–1449.
66. Corma, A.; Juárez, R.; Boronat, M.; Sánchez, F.; Iglesias, M.; García, H. *Chem. Commun.* **2011**, *47*, 1446–1448.
67. Frisch, A. C.; Beller, M. *Angew. Chem., Int. Ed.* **2005**. *44*, 674–688.
68. Gross, J. H. *Mass Spectrometry: A Text Book*; Springer: Heidelberg, 2004.
69. Thomson, J. J. *Philos. Mag.* **1911**, *21*, 225–249.
70. Wiley, W. C.; McLaren, I. H. *Rev. Sci. Instrum.* **1955**, *26*, 1150–1157.
71. Xian, F.; Hendrickson, C. L.; Marshall, A. G. *Anal. Chem.* **2012**, *84*, 708–719.
72. Makarov, A; Denisov, E; Kholomeev, A; Balschun, W; Lange, O; Strupat, K; Horning, S. *Anal. Chem.* **2006**, *78*, 2113–2120.
73. Sage, E.; Brenac, A.; Alava, T.; Morel, R. Dupré, C.; Hanay, M. S.; Roukes, M. L.; Duraffourg, L.; Masselon, C.; Hentz, S. *Nat. Commun.* **2015**, *6*, 6482.
74. Nordling, C; Sokolowski, E; Siegbahn, K. *Phys. Rev.* **1957**, *105*, 1676–1677.
75. Leopold, D. G.; Murray, K. K.; Miller, A. E. S.; Lineberger, W. C. *J. Chem. Phys.* **1985**, *83*, 4849–4865.
76. Ho, J.; Ervin, K. M. Lineberger, W. C. *J. Chem. Phys.* **1990**, *93*, 6987–7002.
77. Kruit, P.; Read, F. H. *J. Phys. E.* **1983**, *16*, 313–324.

78. Cheshnovsky, G.; Yang, S. H.; Pettiette, C. L.; Craycraft, M. L.; Smalley, R. E. *Rev. Sci. Instrum.* **1987**, *58*, 2131–2137.
79. Häkkinen, H.; Yoon, B.; Landman, U.; Li, X.; Zhai, H. J.; Wang, L. S. *J. Phys. Chem. A* **2003**, *107*, 6168−6175.
80. Li, J. Li, X.; Zhai, H. J.; Wang, L. S. *Science* **2003**, *299*, 864-867.
81. Bartels, C.; Hock, C.; Huwer, J.; Kuhnen, R.; Schwöbel, J.; von Issendorff, B. *Science* **2009**, *323*, 1323.
82. León, I.; Yang, Z.; Liu, H. T.; Wang, L. S. *Rev. Sci. Instrum.* **2014**, *85*, 083106.
83. Andrews, L.; Moskovits, M. *Chemistry and Physics of Matrix-Isolated Species*; Elsevier: North Holland, 1989.
84. Dunkin, I. R. *Chem. Soc. Rev.* **1980**, *9*, 1–23.
85. Wako, H.; Ishiuchi, S.; Kato, D.; Féraud, G.; Dedonder-Lardeux, C.; Jouvetb, C.; Fujii, M. *Phys. Chem. Chem. Phys.* **2017**, *19*, 10777–10785.
86. Ebata, T.; Inokuchi, Y. *Chem. Rec.* **2016**, *16*, 1034–1053.
87. Terasaki, A. *J. Phys. Chem. A* **2007**, *111*, 7671–7689.
88. Whittle, E.; Dows, D. A.; Pimentel, G. C. *J. Chem. Phys.* **1954**, *22*, 1943.
89. Andrews, L.; Citra, A. *Chem. Rev.* **2002**, *102*, 885–911.
90. Fukui, K. *Acc. Chem. Res.* **1981**, *14*, 363–368.
91. Fukui, K. *J. Phys. Chem.* **1970**, *74*, 4161–4163.
92. Jensen, F. *Introduction to Computational Chemistry: 2nd Edition*, Wiley: Chichester, 2007.
93. Ohno, K.; Maeda, S. *Chem. Phys. Lett.* **2004**, *384*, 277–282.
94. Ohno, K. *Chem. Rec.* **2016**, *16*, 2198–2218.
95. Maeda, S.; Ohno, K. Morokuma, K. *Phys. Chem. Chem. Phys.* **2013**, *15*, 3683–3701.
96. Page, M; McIver Jr., J. W. *J. Chem. Phys.* **1988**, *88*, 922–935.
97. Page, M.; Doubleday Jr., C; McIver Jr., J. W. *J. Chem. Phys.* **1990**, *93*, 5634–5642.
98. Ohno, K.; Maeda, S. *J. Phys. Chem. A* **2006**, *110*, 8933–8941.
99. Maeda, S.; Harabuchi, Y.; Takagi, M.; Taketsugu, T.; Morokuma, K. *Chem. Rec.* **2016**, *16*, 2232–2248.

# Chapter 2.

# Reaction of $CH_3I$ with $Au^-$ in the gas phase

A major part of this chapter has been published in the following paper.

Muramatsu, S.; Koyasu, K.; Tsukuda, T. *J. Phys. Chem. A* **2016**, *120*, 957–963.

## 2.1. Introduction

As described in Chapter 1, recent studies revealed that Au nanoparticles and clusters can catalyze a variety of important and useful coupling reactions forming carbon–carbon bonds,[1] including Suzuki-Miyaura,[2] Sonogashira,[3,4] and Ullmann reactions.[5] These findings suggest that C(sp or $sp^2$)–X (X = halogen) bonds can be activated by Au catalysts via oxidative addition. In contrast, catalytic activation of C($sp^3$)–X bonds has gained less attention because of difficulties resulting from the more electron-rich $sp^3$ carbon compared to sp or $sp^2$ carbons.[6] It is important to understand whether Au clusters can activate the C($sp^3$)–X bonds in organohalides for future development of Au-based catalysts for coupling reactions.

As an initial step toward this goal, in this chapter I focus on the simple gas phase reaction between the atomic gold anion ($Au^-$) and methyl iodide ($CH_3I$) with the expectation that $Au^-$ is more nucleophilic than Au(0), Au(I), and Au(III) species commonly used for gold catalysis.[7] The first question I addressed was whether $Au^-$ can activate the C–I bond of $CH_3I$. Wilkins previously reported the production of $I^-$ by the nucleophilic attack of $Au^-$ on $CH_3I$.[8] However, it was not clear whether Au–$CH_3$ bond was formed because neutral products were not characterized. In this study, I conducted the reaction under high-pressure helium and successfully isolated the adduct of $Au^-$ and $CH_3I$ by collisional cooling. Photoelectron spectroscopy and theoretical calculations demonstrated that Au is inserted in the C–I bond of $CH_3I$. The second question concerns the mechanism of insertion of Au into the C–I bond of $CH_3I$. Two mechanisms have been proposed for the oxidative addition of haloalkanes to a metal atom (Scheme 2.1):[9–11] eq. 2.1 in Scheme 2.1 is the direct oxidative insertion into the C–X bond and eq. 2.2 is the $S_N2$ reaction followed by migration of the leaving $X^-$. The mechanism is important

from the viewpoint of asymmetric synthesis because the stereochemistry of the central carbon is retained in eq. 2.1, while it is inverted in eq. 2.2. A theoretical study based on the global reaction route mapping (GRRM) method[12,13] revealed that formation of the adduct $[I–Au–CH_3]^-$ occurred via the $S_N2$ route (eq. 2.2). I finally propose that another $CH_3I$ molecule undergoes oxidative addition to the $[I–Au–CH_3]^-$ adduct to yield the coupling product $C_2H_6$ and $AuI_2^-$.

**Scheme 2.1. Proposed Mechanism of Oxidative Addition of Haloalkanes to a Metal Atom.**

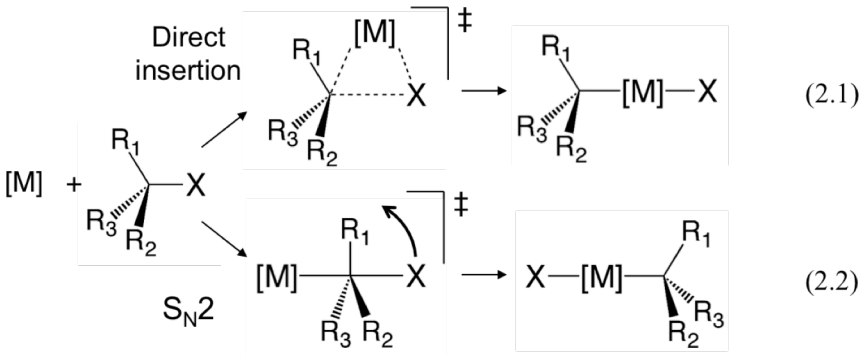


## 2.2. Methods

### 2.2.1. Experiment

#### 2.2.1.1. General description of apparatus

The apparatus used in this study is schematically shown in Figure 2.1.[14] It consists of four parts: a laser ablation ion source,[15] a reaction cell, a Wiley-McLaren type linear time-of-flight mass spectrometer (TOF-MS)[16] with a flight length of 1.59 m, and a magnetic bottle type time-of-flight photoelectron spectrometer (MB-PES)[17,18] with a flight length of 1.07 m. The chambers are evacuated by three turbo molecular pumps

differentially, to achieve base pressures of typically ~1 × $10^{-4}$ and ~7 × $10^{-8}$ Pa at the source chamber and the photodetachment chamber, respectively. Under the experimental conditions, the pressures were kept below ~2 × $10^{-2}$ and ~1 × $10^{-5}$ Pa, respectively. The experiments were conducted at 10 Hz. All the pulse sequences described below were controlled by digital delay generators (Stanford Research Systems, DG645).

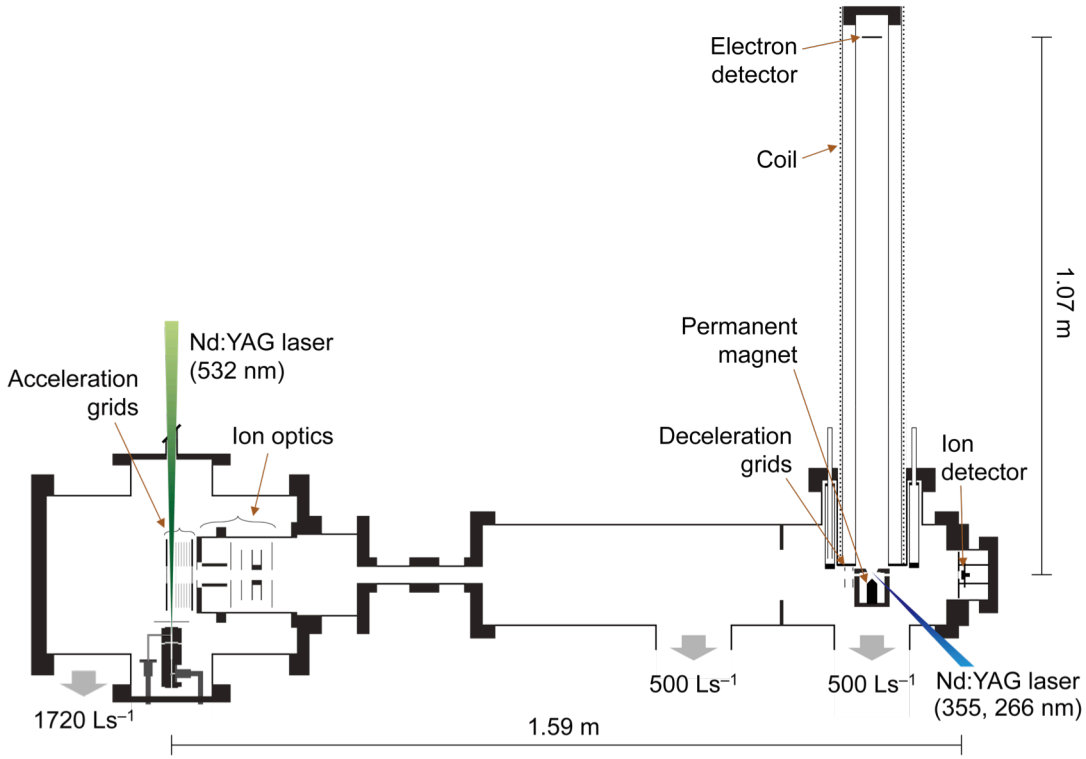


**Figure 2.1.** The experimental setup. Gray allows represent evacuation by turbo molecular pumps with the pumping speeds indicated.

### 2.2.1.2. Generation of $Au^-$ ions and reaction

The ion source and the reaction cell are shown in Figure 2.2. The $Au^-$ anion was

generated by irradiating with a focused second harmonic output from a Nd:YAG laser (Spectra-Physics, INDI-HG) with typical pulse energy of 10–50 mJ/pulse onto a rotating and translating gold target rod (Nilaco, purity: 99.95%, diameter: 2 mm, length: 20 mm). The generated $Au^-$ anions were introduced into a channel (diameter: 2 mm, length: 80 mm) by a flow of helium gas (purity: 99.999%) with backing pressure of 4.0–10 atm supplied through a pulsed valve (Parker Hannifin, series 9, injection orifice: 0.8 mm, pulse width 200–300 μs). Then, the $Au^-$ anions were allowed to react with $CH_3I$ (Wako Pure Chemical Industries, purity: 99.5%) or *t*-butyl iodide (*t*-$C_4H_9I$, Tokyo Chemical Industry, purity 97%) injected into the reaction cell by another pulse valve with/without dilution with helium gas (0–1.5 atm). All the chemicals were used without further purification.

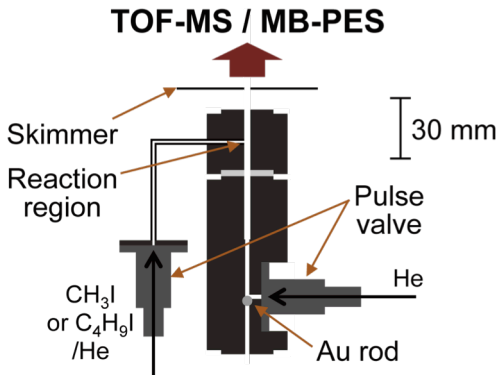


**Figure 2.2.** Laser ablation ion source and reaction cell.

### 2.2.1.3. Mass spectrometry

The chemical compositions of the reaction products were studied by Wiley-McLaren type TOF-MS. The ions with mass of *m* and charge number of *z* undergo two-step acceleration to pass through a field-free region with a constant distance to a

detector (Figures 2.1 and 2.3). The time-of-flight of the ion, $t$, follows eq. 2.3,[16]

$$t = \left(\frac{m}{2ze(sE_1 + d_2E_2)}\right)^{\frac{1}{2}} \left( 2k_0^{\frac{1}{2}}s + \frac{2k_0^{\frac{1}{2}}}{k_0^{\frac{1}{2}} + 1} d_2 + d_3 \right) \tag{2.3}$$

where $k_0$ is represented as eq. 2.4.

$$k_0 = \frac{sE_1 + d_2E_2}{sE_1} \tag{2.4}$$

The constant $e$ is an elementary charge, $E_1$ and $E_2$ are uniform electric fields at each acceleration region, $d_1$, $d_2$, and $d_3$ are distances of each acceleration region and the field free region, and $s$ represents an initial position of the ion, respectively (Figure 2.3). Equation 2.3 indicates that ions with different $m/z$ are separated based on the time-of-flight. The mass-resolution of the Wiley-McLaren type TOF-MS reaches maximum when eq. 2.5 is satisfied.[16]

$$d_3 = 2sk_0^{\frac{3}{2}} \left( 1 - \frac{1}{k_0 + k_0^{\frac{1}{2}}} \frac{d_2}{s} \right) \tag{2.5}$$

Since $k_0$ is a function of the ratio $E_2/E_1$ (eq. 2.4), the mass-resolution can be tuned by the ratio of voltages applied to the repeller and extractor grids (Figure 2.3).

After the reaction (Section 2.2.1.2), the anionic species were extracted perpendicularly to the initial beam direction and accelerated up to 4.0 keV by a pulsed

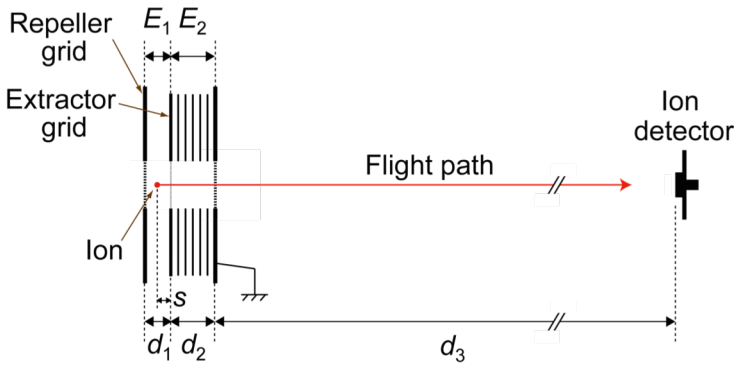


**Figure 2.3.** Schematic image of Wiley-McLaren type TOF-MS.

electric field (Behlke, HTS 61-03-GSM, pulse duration: ~200 μs, pulse rise time: ~400 ns). In order to optimize the mass-resolution, the voltage ratio of the repeller and extractor grids was tuned (eq. 2.5) by resistors connected between the grids, which however results in elongation of pulse rise time of the extractor grid to ~1 μs. The accelerated anions were then mass-separated and detected by a microchannel plate (Hamamatsu Photonics, F4655-12). The signals were recorded and accumulated by a digital oscilloscope (Tectronix, TDS 580D) for typically 200–1,000 laser shots. The mass-resolution ($m/\Delta m$) of this spectrometer was ~340 at $m/z$ = 200. Although the resolution at higher $m/z$ region is actually low (~100 at $m/z$ = 450) in this setup due to the long pulse rise time of the extractor grid, it does not affect the assignment of the mass peaks and discussions in this study.

### 2.2.1.4. Photoelectron spectroscopy

Electronic structures of mass-separated anions were studied by PES. The electron binding energy $E_B$ of a target anion is examined by kinetic energy ($E_K$) of the photoelectron produced by irradiation with laser light (photon energy = $hv$) on the anion

by eqs. 2.6 and 2.7.

$$E_{\mathrm{B}} = h\nu - E_{\mathrm{K}} \tag{2.6}$$

$$E_{\mathrm{K}} = \frac{1}{2} m_{\mathrm{e}} \left(\frac{l}{t}\right)^2 \tag{2.7}$$

where $m_{\mathrm{e}}$, $l$, and $t$ represent mass of electron, flight path length of the photoelectron (1.07 m, Figure 2.1), and TOF of the photoelectron, respectively.

In the measurement of photoelectron spectra, magnitude of the ion-acceleration voltage for TOF-MS was lowered to 1.2–2.4 kV, and the anion of interest after mass-separation was decelerated by a pulsed electric field (0.67–2.0 × $10^5$ V·$m^{-1}$, pulse duration: 300–800 ns, Behlke, HTS 151-03-GSM) at 38 mm upstream from photodetachment region, to suppress Doppler broadening of the spectra.[19] Then it was irradiated with an unfocused 3rd (355 nm, 3.50 eV) or 4th (266 nm, 4.66 eV) harmonic output from another Nd:YAG laser (Spectra-Physics, INDI40) with < 5 mJ/pulse. The detached photoelectrons were collected by an inhomogeneous magnetic field produced by a cylindrical permanent magnet (~1000 G) fitted with a soft iron tip and guided by a weak field (~40 G) produced by a solenoid coil (number of turns: ~1000 $m^{-1}$, current: 3.5 A) to a microchannel plate (El-Mul, Double MCP 33). The signals were amplified 5-fold by a preamplifier (Stanford Research Systems, SR445) and counted by a multichannel scalar (Stanford Research Systems, SR430) with a time bin of 5 ns. The photoelectron spectra were obtained by accumulations of 10,000–20,000 laser shots, after background subtraction in case of measurements at 266 nm. The photoelectron kinetic energies were obtained from TOF of photoelectrons (eq. 2.7) and were

calibrated against the known photoelectron peaks of $I^-$ (ref. 20) and $Au^-$;[21] $I^-$ anion was generated by the dissociative electron attachment on $CH_3I$ molecular beams.[22] The TOF spectra were converted to the energy spectra according to eq. 2.8,

$$\tilde{I}(E)dE = \frac{m_e l^2}{t^3} I(t)dt \tag{2.8}$$

where $E$ represents binding energy of the photoelectron, $\tilde{I}(E)$ and $I(t)$ represent binding energy- and TOF-dependent photoelectron counts, respectively. The coefficient $\frac{m_e l^2}{t^3}$ is Jacobian factor for changing coordinates. The spectra are shown after smoothing by averaging the photoelectron counts of neighboring three points. The resolution of the MB-PES was ~120 meV for electrons with a kinetic energy of 1.0 eV.

### 2.2.2. Computation

#### 2.2.2.1. Calculation of structural candidates

Electronic and geometrical structures of the detected species were studied by density functional theory (DFT) calculations using Gaussian 09[23] program. The hybrid functional B3LYP[24,25] was used for all calculations in this section. Basis sets used were LanL2dz for Au[26] and I[27] atoms, and 6-31+G(d,p) for H and C atoms.[28–31] In energy calculations using self-consistent field, the convergence criterion was set to $10^{-8}$ a. u. (atomic units) for the total electronic energy (with an input code of "scf=tight"). In numerical integrations, ultrafine grids were used, which have 75 radial shells and 302 angular points in every shell ("int=ultrafine").

Structural optimizations based on berny algorithm[32] were carried out starting from

various initial structures with the tight convergence criteria; the maximum and a root mean square (RMS) of forces are $1.5 \times 10^{-5}$ and $1.0 \times 10^{-5}$ a. u., respectively. The maximum and an RMS of displacements are $6.0 \times 10^{-5}$ and $4.0 \times 10^{-5}$ a. u., respectively ("opt=tight"). Frequency calculations were conducted to check whether the optimized structure was a local minimum structure (LM). Total electronic energy of each calculated structure is shown after vibrational zero-point energy (ZPE) correction. In order to compare the calculated structures to the experimentally obtained photoelectron spectra, the electron vertical detachment energy (VDE) of each LM was estimated from the energy difference between the ground state of the anion and that of neutral for the anion structure. In the calculations of VDE, the vibrational ZPE was not considered since it is physically meaningless for the structures at non-stationary points on a potential energy surface. Atomic charges were evaluated by natural population analysis based on natural bond orbitals (NBOs).[33]

#### 2.2.2.2. Reaction pathway exploration

In order to gain insights into reaction mechanisms, I explored the transition state structures (TSs) and intrinsic reaction coordinates (IRCs)[34,35] using Gaussian 09[23] and GRRM11[12,13,36–39] programs. In Gaussian 09, TSs were obtained by structural optimization[32] followed by frequency calculation to confirm that the optimized structure corresponds to the first order saddle point of the potential energy surface. In GRRM11, TSs were explored without any intuition since the calculations were started from the LMs obtained in Section 2.2.2.1 using the anharmonic downward distortion following (ADDF)[12,13] method. In ADDF method, I searched for anharmonic downward distortions (ADDs) around LMs, a potential energy lowering with respect to a harmonic

potential (Figure 1.12, Chapter 1). It gives rough directions along the reaction pathway, which enables to find good guesses of TSs by following the maximal-ADD paths.

Although the convergence criteria are slightly different between the programs, the obtained TS structures were identical to each other within the energy of 1 meV. All the IRC calculations were performed using GRRM11, by local quadratic approximation (LQA) method.[40,41]

## 2.3. Results and discussion

### 2.3.1. Oxidative addition of $CH_3I$ to $Au^-$

#### 2.3.1.1. Formation of adduct product $AuCH_3I^-$

Figure 2.4 shows typical mass spectra before (a) and after (b) the reaction of $Au^-$ with $CH_3I$. Under the reaction conditions employed in this study, the mass peak of $Au^-$

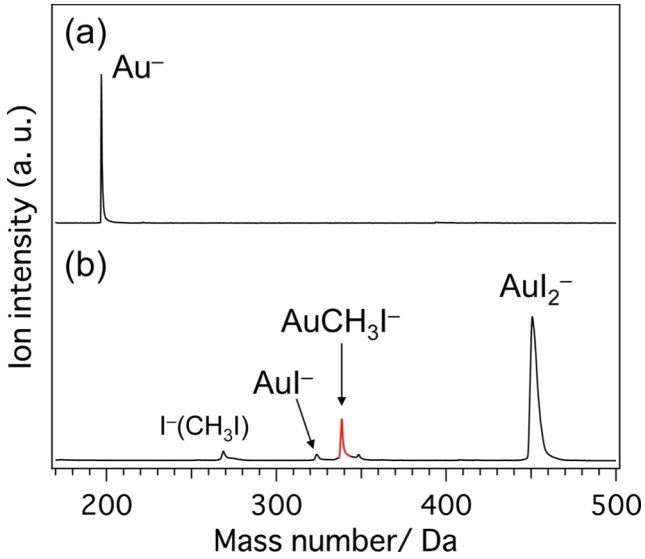


**Figure 2.4.** Mass spectra before (a) and after (b) the reaction of $Au^-$ with $CH_3I$.

completely disappears while $AuCH_3I^-$ and $AuI_2^-$ are observed as major products. A small amount of $AuI^-$ is also observed. The absence of $Au_n^-$ ($n \geq 2$) in Figure 2.4(a) indicates that $AuCH_3I^-$ is formed by the reaction of monomeric $Au^-$ and $CH_3I$, as shown in eq. 2.9.

$$Au^- + CH_3I \rightarrow AuCH_3I^- \qquad (2.9)$$

The same reaction was studied previously by Wilkins in a different experimental setup, in which only $I^-$ was observed by a slow $S_N2$ displacement reaction.[8] Successful observation of the $AuCH_3I^-$ adduct in this study is due to the effective cooling by multiple collisions. In contrast, production of $AuI_2^-$ requires at least two $CH_3I$ molecules, while $AuX_2^-$ (X = Cl or Br) can be generated by reactions of $Au^-$ with a single molecule of $CHX_3$.[8] Actually, the intensity of $AuI_2^-$ is reduced more than that of $AuCH_3I^-$ when the pressure of $CH_3I$ in the reaction cell is reduced by lowering the temperature of the $CH_3I$ reservoir as shown in Figure 2.5.

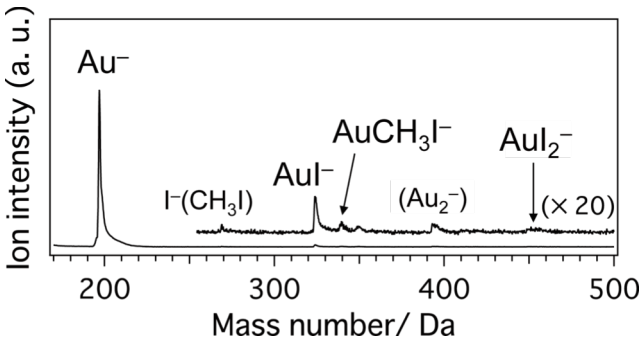


**Figure 2.5.** Mass spectrum recorded on the condition that temperature of the $CH_3I$ reservoir was lowered by liquid nitrogen.

### 2.3.1.2. Structural determination of $AuCH_3I^-$

The photoelectron spectrum of mass-selected $AuCH_3I^-$ (kinetic energy: ~1.3 keV) recorded at 266 nm (photon energy: 4.66 eV) shown in Figure 2.6 exhibits three peaks. The VDE values of peaks $\mathbf{X_1}$ and $\mathbf{X_2}$ were determined to be 2.41 ± 0.10 and 3.96 ± 0.03 eV by fitting with a Gaussian function. Quantitative analysis of the VDE of the peak observed at ~4.2 eV was not conducted because of ambiguity in the peak position due to limited collection efficiency of slow photoelectrons and serious background noise in the energy region above 4 eV. The intensity ratio of bands $\mathbf{X_1}$ and $\mathbf{X_2}$ could be changed with the pressure of the carrier gas in the ion source, as discussed in detail in Chapter 3, which implies they are assigned to structural isomers.

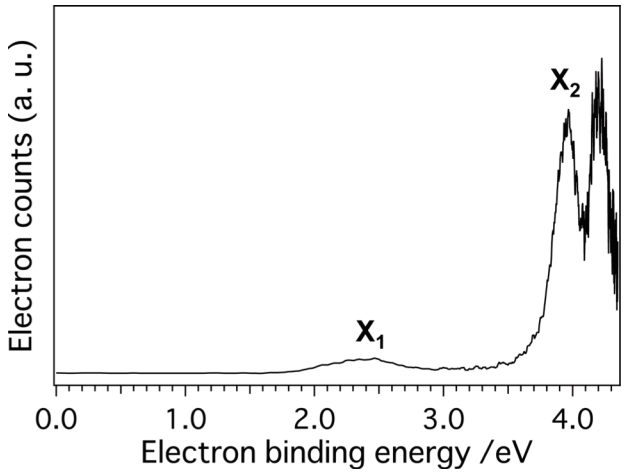


**Figure 2.6.** Photoelectron spectrum of $AuCH_3I^-$ recorded at 266 nm.

Structure candidates for $AuCH_3I^-$ giving photoelectron bands $\mathbf{X_1}$ and $\mathbf{X_2}$ were studied by DFT calculations. Table 2.1 summarizes the obtained local minimum structures for $AuCH_3I^-$ (**1**–**3**). In structure **1**, $Au^-$ is weakly bonded to the I atom of

$CH_3I$ ($[Au–I–CH_3]^-$). Structure **2** can be viewed as an ion-neutral complex ($[AuCH_3\cdots I^-]$), where the $I^-$ anion is electrostatically bound to a polar molecule $AuCH_3$. Structure **3** is the most stable structure, in which the Au atom is inserted into the C–I bond of $CH_3I$ ($[I–Au–CH_3]^-$). The electronic charge originally localized on Au is distributed throughout the framework in **3**. The VDE values of each structure were calculated and are listed in Table 2.1. Comparison between the experimental and theoretical VDE values led us to assign bands $\mathbf{X_1}$ and $\mathbf{X_2}$ to structures **1** and **3**, respectively. The large exothermicity (2.49 eV) associated with the formation of **3** from $Au^-$ and $CH_3I$ is dissipated by collision with high-pressure He. The intense band of $\mathbf{X_2}$ in Figure 2.6 is consistent with high stability of structure **3**. Formation of **3** can be

**Table 2.1. Calculated Stable Structures for $AuCH_3I^-$.**

| Structure[a] | $\Delta E$ /eV[b] | VDE /eV[c] |
|---|---|---|
| 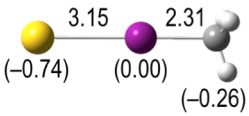 $[Au–I–CH_3]^-$ (**1**) | –0.43 | 2.59 |
| 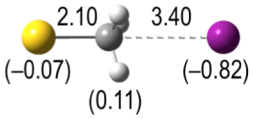 $[AuCH_3\cdots I^-]$ (**2**) | –1.19 | 3.35 |
| 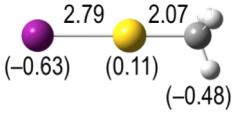 $[I–Au–CH_3]^-$ (**3**) | –2.49 | 4.02 |

[a] Numbers with/without parentheses indicate NBO charges/bond lengths (Å), respectively. [b] Relative total electronic energy with respect to $Au^-$ + $CH_3I$. [c] Vertical detachment energy. Color codes: yellow = Au, purple = I, gray = C, white = H.

viewed as oxidative addition of $CH_3I$ to $Au^-$, since I and $CH_3$ fragments from $CH_3I$ are bonded to Au and the formal charge on Au is increased from –1.00 |e| to +0.11 |e|. To the best of our knowledge, this is the first demonstration that C($sp^3$)–I can be activated by oxidative addition to $Au^-$, although the production of the Cu analogue, $[CH_3CuI]^-$, was reported in the gas phase reaction between $[CH_3CuCH_3]^-$ and allyl iodide.[42]

### 2.3.1.3. Reaction mechanism

In order to obtain an insight into the reaction mechanism, I calculated the potential energy profiles along the IRCs[43] for the formation of **1**–**3** from $Au^-$ and $CH_3I$ (eq. 2.9).

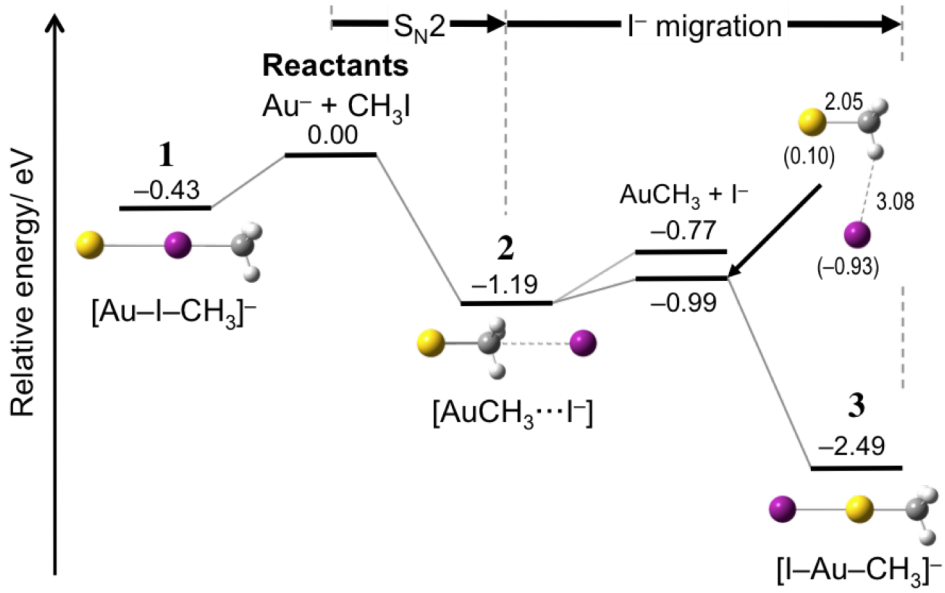


**Figure 2.7.** Energy profile of the reaction pathway for the formation of $AuCH_3I^-$ (**1**–**3**) from $Au^-$ and $CH_3I$. Numbers with/without parentheses in TS between **2** and **3** indicate NBO charges/bond lengths (Å), respectively. Color codes: yellow = Au, purple = I, gray = C, white = H. Gray solid lines represent intrinsic reaction coordinates (IRCs) between structures.

Figure 2.7 shows the energy profile of the overall reaction pathways for **1**–**3** that are calculated to be energetically most favorable by the GRRM11 program, where all the ADD following was conducted around structures **1**–**3**. During ADDF calculations, various less stable LMs were newly found ($\Delta E$ > 0.5 eV with respect to $Au^-$ + $CH_3I$), whose ADDs were not followed because of the computational cost.

Structure **1** can be formed without any potential barrier via direct approach of $Au^-$ to the I atom of $CH_3I$. On the other hand, structure **2** can be formed via the attack of $Au^-$ on the methyl group of $CH_3I$ without any barrier. Figure 2.8 shows a more detailed energy profile and NBO charges for the formation of **2** along the reaction coordinate (Au–C distance). When $Au^-$ approaches $CH_3I$ at a distance of 2.64 Å, the $CH_3$ group

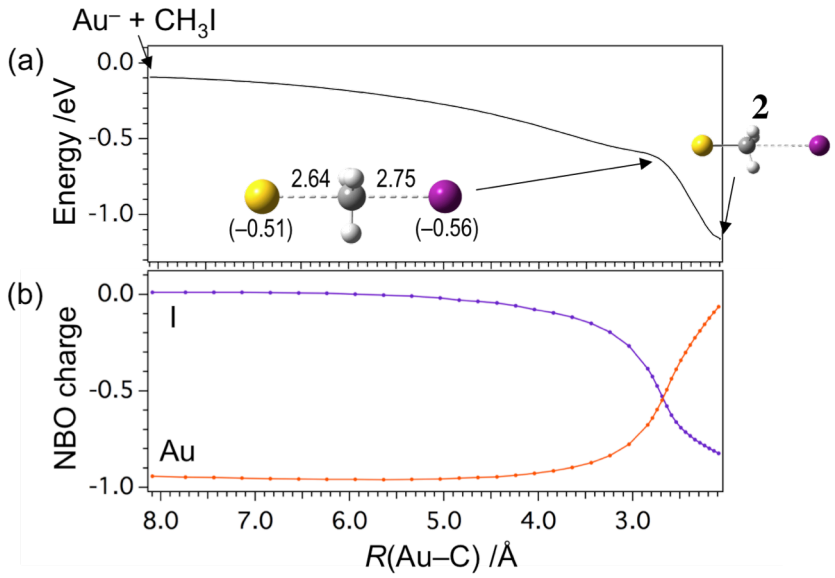


**Figure 2.8.** Profiles of (a) energy and (b) NBO charge of Au and I atoms along the reaction pathway to form structure **2** from $Au^-$ and $CH_3I$ at the distance of ~ 8 Å. The distance between Au and C atoms is adopted as the reaction coordinate. Energies are shown with respect to the reactants at infinite distance. Inset shows the structure at the coordinate where the methyl group becomes planer.

becomes planar and the negative charge is distributed over the Au and I atoms (Inset of Figure 2.8(a)). Then, formation of the Au–C bond associated with the Walden inversion of the $CH_3$ group proceeds concertedly with the release of $I^-$. Therefore, this step can be viewed as a bimolecular nucleophilic substitution ($S_N2$) reaction. The structure of the TS located between **2** and **3** suggests that migration of the I atom of **2** leads to conversion into **3**. Migration of the I atom of **2** is energetically more favorable than dissociation into $AuCH_3 + I^-$ because the TS for the $I^-$ migration step is located below the dissociation limit. The internal migration of $I^-$ is induced by the positive charge on

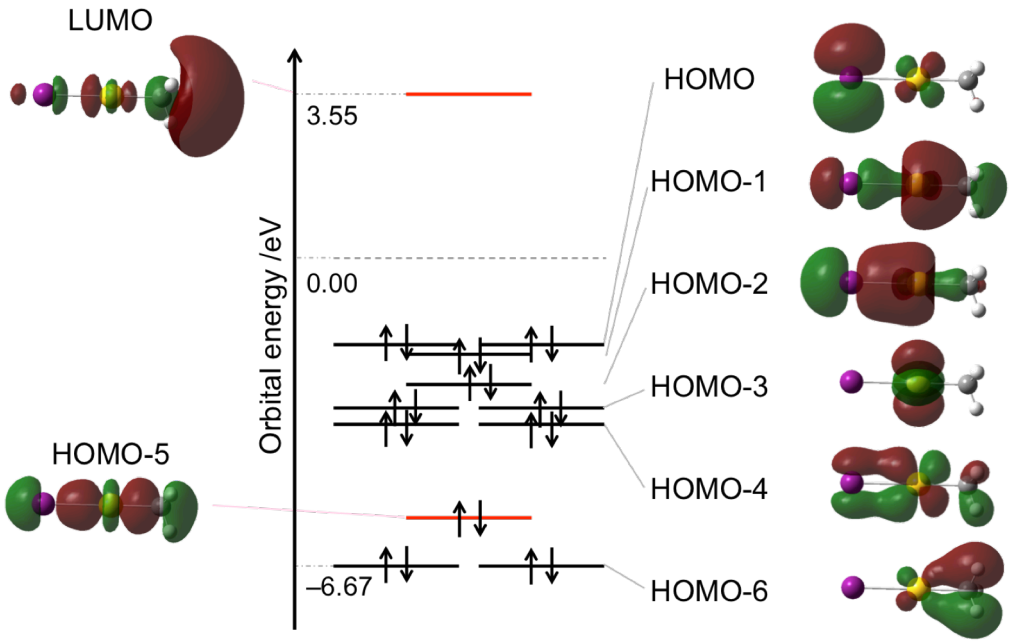


**Figure 2.9.** Energy levels and charge density surfaces of the molecular orbitals of $[I–Au–CH_3]^-$. The isodensity value is 0.03 |e|. HOMO-2, HOMO-4 are bonding orbitals between Au and I atoms, while the corresponding antibonding orbitals are also occupied (HOMO-1, HOMO respectively). Stability of $[I–Au–CH_3]^-$ mainly comes from accommodation of the electrons into strong bonding orbital HOMO-5, counterpart of which lies in higher energy level (LUMO).

the Au atom in the $AuCH_3$ unit (+0.19 |e|), and strong bonding between the 5d orbital of Au and 5p orbital of the I atom (Figure 2.9), as proposed previously for the insertion of Au into the C–X bond.[44,45] This mechanism is consistent with a previous proposal that eq. 2.2 in Scheme 2.1 is preferred over direct insertion (eq. 2.1) with an increase in the negative charge on the metal.[10] The insertion mechanism of $Au^-$ into the $CH_3$–I bond reminds us of the formation of $CH_3CO_2I^-$ in the reaction of $(CO_2)_n^-$ with $CH_3I$.[22]

### 2.3.2. Steric effect on oxidative addition

#### 2.3.2.1. Computational results

As shown in Figure 2.7, the oxidative addition of $CH_3I$ to $Au^-$ is exothermic by 2.49 eV. This down-hill energy profile explains the dominant production of $[I–Au–CH_3]^-$ (**3**). In order to support further the insertion mechanism, I examined the structure of $AuC_4H_9I^-$ formed by the reaction between $Au^-$ and a sterically demanding alkyl iodide, *t*-$C_4H_9I$. Optimized structures of $AuC_4H_9I^-$ along with their VDE values are summarized in Table 2.2. Structures **4**, **6**, and **7** can be described as $[Au–I–C_4H_9]^-$, $[AuC_4H_9\cdots I^-]$, and $[I–Au–C_4H_9]^-$, respectively. These structures (**4**, **6**, and **7**) are counterparts of structures **1**, **2**, and **3** for $AuCH_3I^-$, respectively. In addition to structures **4**, **6**, and **7**, I obtain a new structure **5**, whose counterpart is not found in $AuCH_3I^-$. Structure **5** can be viewed as an ion-neutral complex $[Au^-\cdots C_4H_9I]$, in which *t*-$C_4H_9I$ is bound to $Au^-$ by pointing the dipole moment to maximize an electrostatic attractive force.

Figure 2.10 shows the energy profiles calculated for the formation of structures **5**–**7**. The energy profile for the reaction of $Au^-$ and $CH_3I$ is also shown for comparison. The reaction mechanism for $Au^-$ + *t*-$C_4H_9I$ is similar to that of $Au^-$ + $CH_3I$ and composed of

the sequential reaction of $S_N2$ and $I^-$ migration. However, there is a substantial difference. A potential barrier in the $S_N2$ step emerges, resulting in stabilization of the ion-neutral complex, [$Au^-\cdots C_4H_9I$] (**5**). The structure of the TS located between **5** and **6**, shown in Figure 2.10, indicates that the four carbon atoms from *t*-$C_4H_9$ are arranged in a

**Table 2.2. Calculated Stable Structures for $AuC_4H_9I^-$.**

| Structure[a] | $\Delta E$ /eV[b] | VDE /eV[c] |
|---|---|---|
| 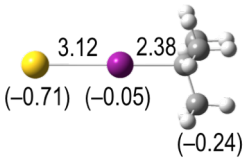 [Au–I–$C_4H_9$]$^-$ (**4**) | –0.39 | 2.45 |
| 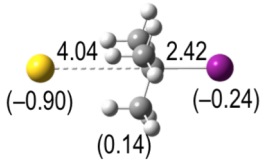 [$Au^-\cdots C_4H_9I$] (**5**) | –0.64 | 2.81 |
| 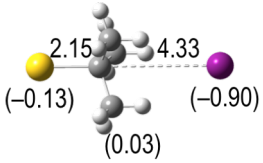 [$AuC_4H_9\cdots I^-$] (**6**) | –1.16 | 3.43 |
| 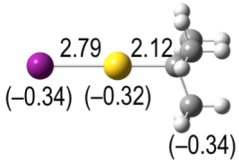 [I–Au–$C_4H_9$]$^-$ (**7**) | –2.20 | 3.67 |

[a] Numbers with/without parentheses indicate NBO charges/bond lengths (Å), respectively. [b] Relative total electronic energy with respect to $Au^-$ + *t*-$C_4H_9I$. [c] Vertical detachment energy. Color codes: yellow = Au, purple = I, gray = C, white = H.

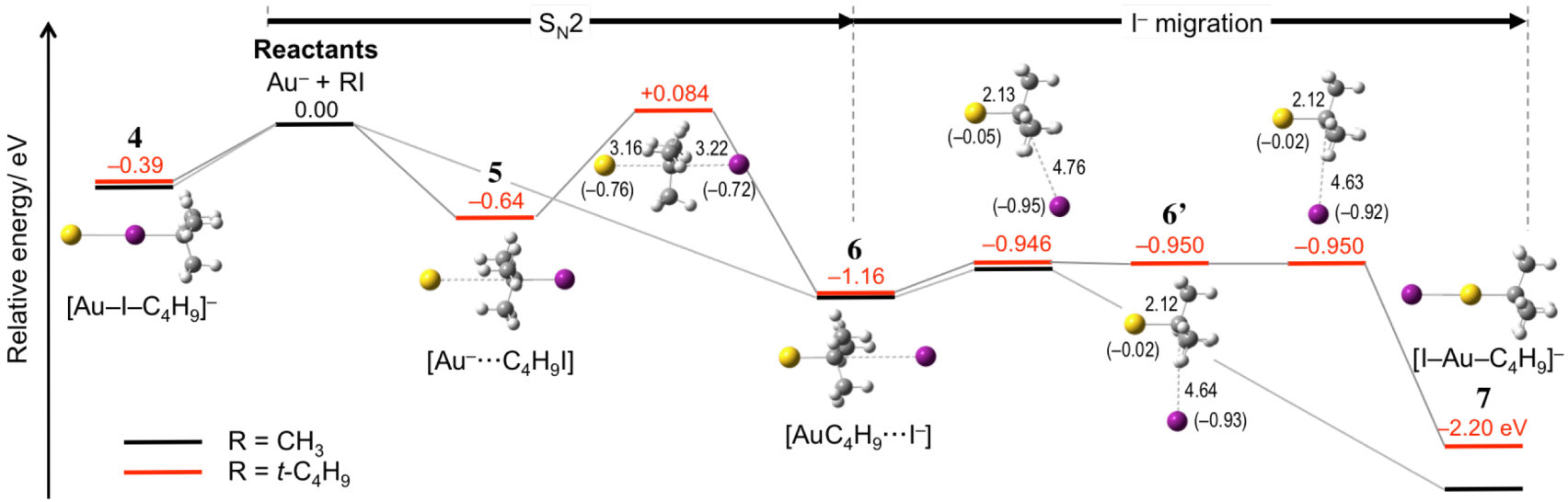


**Figure 2.10.** Overall reaction pathway for stable structures of $AuC_4H_9I^-$ (red) and $AuCH_3I^-$ (black). Atom colors, bond distances, and NBO charges are represented in the same manner as in Table 2.1. Only the structures and energies of $AuC_4H_9I^-$ are explicitly shown.

planar configuration. Since the energy level of the TS is located above that of the reactants, $Au^-$ + *t*-$C_4H_9I$, structure **5** may be formed under the present experimental conditions in which efficient collisional cooling is operative. A new ion-neutral complex, [$AuC_4H_9\cdots I^-$] (**6**'), is found along the $I^-$ migration pathway. However, two TSs adjacent to **6**' are located at nearly the same energy. The overall barrier height associated with $I^-$ migration (from **6** to **7**) is comparable to that in the reaction of $CH_3I$ (~0.2 eV). These results indicate that the bulky *t*-$C_4H_9$ group does not significantly affect the $I^-$ migration step.

### 2.3.2.2. Photoelectron spectra of $AuC_4H_9I^-$

The adduct $AuC_4H_9I^-$ is produced by the reaction of $Au^-$ and *t*-$C_4H_9I$. The mass spectrum after the reaction is shown in Figure 2.11, and photoelectron spectra of $AuC_4H_9I^-$ recorded at 355 and 266 nm are shown in Figures 2.12(a) and (b), respectively. Two bands $\mathbf{X_2}$ and $\mathbf{X_3}$ with electron binding energies of 2.77 ± 0.03 and 3.78 ± 0.03 eV, respectively, are observed in addition to a small band $\mathbf{X_1}$ centered at

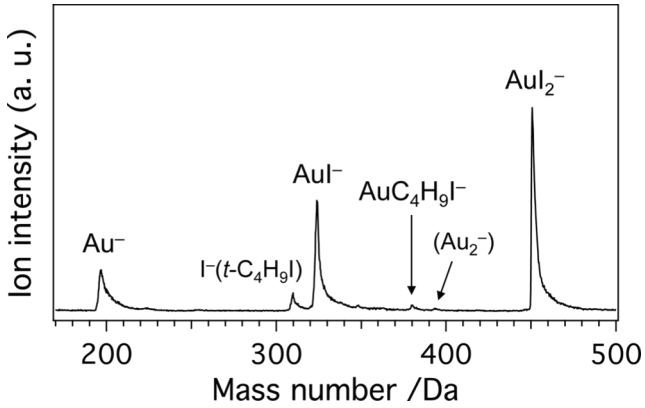


**Figure 2.11.** Mass spectra after the reaction of $Au^-$ with *t*-$C_4H_9I$.

~2.4 eV. The most remarkable difference from the spectrum of $AuCH_3I^-$ is the observation of band $\mathbf{X_2}$. Band $\mathbf{X_2}$ can be assigned to the ion-neutral complex [$Au^-$ $\cdots C_4H_9I$] (**5**) with a calculated VDE value of 2.81 eV (Table 2.2). This assignment is supported by the fact that peak $\mathbf{X_2}$ has a sharp profile comparable to that of $Au^-$ (Figure 2.12(c)), and is shifted toward a higher binding energy by ~0.5 eV, typical for ion-dipole interaction. The formation of structure **5**, which is located along the potential surface shown in Figure 2.10 provides a direct evidence that the oxidative addition proceeds via $S_N2$ mechanism (eq. 2.2). Band $\mathbf{X_3}$ is assigned to the most stable structure **7** rather than structure **6** since the reaction with $CH_3I$ did not produce structure **2** (Figure

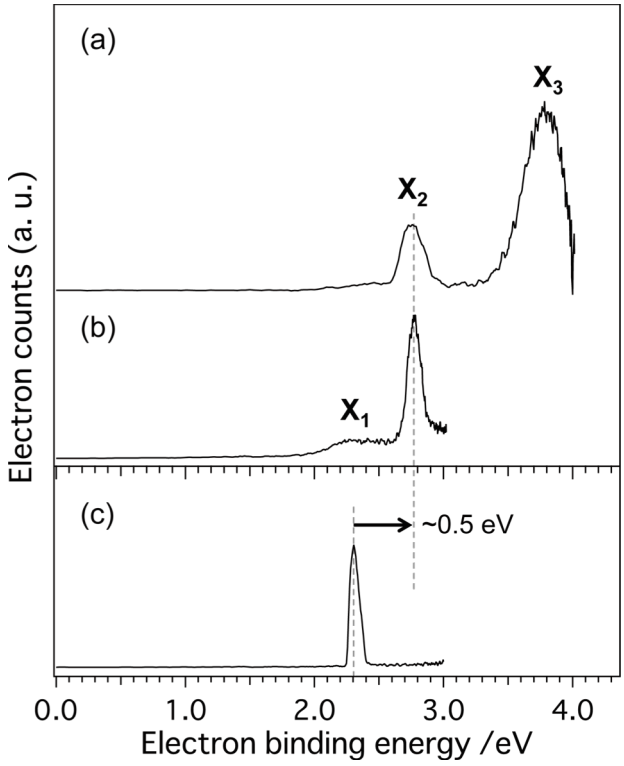


**Figure 2.12.** Photoelectron spectra of (a) $AuC_4H_9I^-$ at 355 nm, (b) $AuC_4H_9I^-$ at 266 nm and (c) $Au^-$ at 355 nm. A sharp peak in (c) is assigned to the photodetachment represented as $Au^0$ ($^2S_{1/2}$) $\leftarrow$ $Au^-$ ($^1S_0$).

2.7), which corresponds to the ion-neutral complex at the exit channel of $S_N2$. The smaller electron binding energy for band $\mathbf{X_3}$ in Figure 2.12 compared to that for band $\mathbf{X_2}$ in Figure 2.6 is consistent with the smaller VDE value for **7** (3.67 eV) than that for **3** (4.02 eV). Band $\mathbf{X_1}$ at ~2.4 eV is assigned to structure **4**. These experimental and theoretical results support our conclusion that the oxidative addition of $CH_3I$ to $Au^-$ proceeds via nucleophilic attack of $Au^-$ on $CH_3I$ and subsequent migration of $I^-$.

### 2.3.3. Formation of $C_2H_6$ via sequential oxidative addition of $CH_3I$

Finally, I consider the formation mechanism of the major product $AuI_2^-$ observed in Figure 2.4(b). There are two possible pathways for the formation of $AuI_2^-$ from $Au^-$ and two $CH_3I$ molecules. The first possibility is a sequential abstraction of I atoms as shown in eq. 2.10.

$$Au^- + 2CH_3I \rightarrow AuI^- + CH_3 + CH_3I \rightarrow AuI_2^- + 2CH_3 \qquad (2.10)$$

Formally, $Au^-$ abstracts the I atom from $CH_3I$ to from $AuI^-$ in the first step and $AuI^-$ thus formed successively abstracts the I atom from another $CH_3I$. The energy diagram of eq. 2.10 is shown in Figure 2.13(a). Although the first step was calculated to be slightly endothermic by 0.15 eV, the overall process becomes exothermic by 1.02 eV since the second step was calculated to be exothermic by 1.17 eV. There are two possible pathways for formation of $AuI^-$: abstraction of I atom of $CH_3I$ by $Au^-$ via intermediate **1** and Au–C bond dissociation of oxidative addition product **3** (Figure 2.7). The former pathway is more plausible since $AuI^-$ was formed efficiently in the reaction of $Au^-$ + *t*-$C_4H_9I$ (Figure 2.11) in which oxidative addition was sterically suppressed.

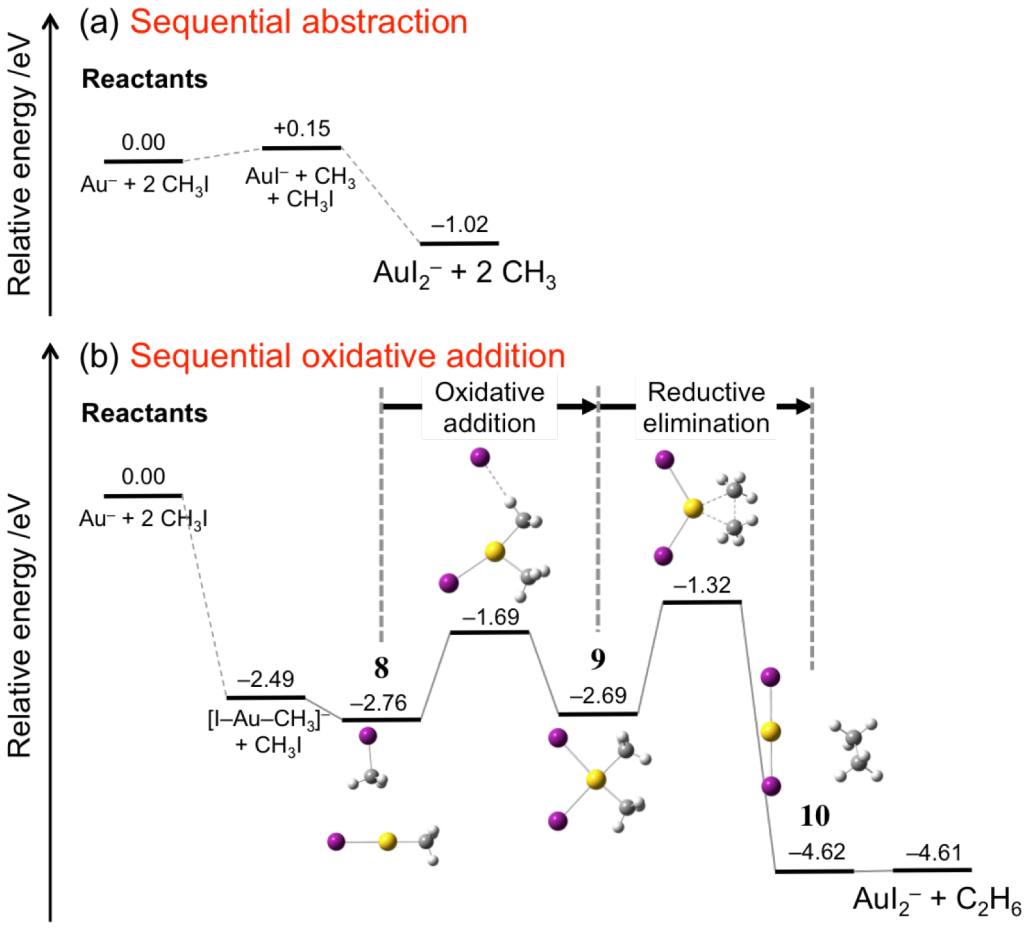


**Figure 2.13.** Energy profiles of formation of $AuI_2^-$ from $Au^-$ and two $CH_3I$ molecules. (a) The sequential I abstraction pathway shown in eq. 2.10 and (b) the sequential oxidative addition pathway shown in eq. 2.11. Energies are relative to those of $Au^- + 2CH_3I$.

The IRCs of the second step could not be determined because I could not obtain any intermediate structure including $[I–Au–I–CH_3]^-$, in which $AuI^-$ is weakly bonded to the I atom of $CH_3I$, within the level of the calculations in this study.

The second possibility for the formation of $AuI_2^-$ involves sequential oxidative addition of two $CH_3I$ molecules onto $Au^-$ as described in eq. 2.11.

$$Au^- + 2CH_3I \rightarrow [I–Au–CH_3]^- + CH_3I \rightarrow AuI_2^- + C_2H_6 \qquad (2.11)$$

In the second step, $CH_3I$ is oxidatively added to $[I–Au–CH_3]^-$ followed by reductive elimination of two $CH_3$ ligands in the form of $C_2H_6$. The energy diagram of eq. 2.11 is shown in Figure 2.13(b). The overall process was calculated to be largely exothermic by

**Table 2.3. Calculated Stable Structures for $AuC_2H_6I_2^-$.**

| Structure[a] | $\Delta E$ /eV[b] |
|---|---|
| 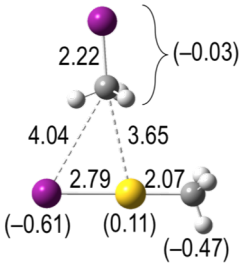 $[(CH_3I)\cdots(I–Au–CH_3)^-]$ (**8**) | –2.76 |
| 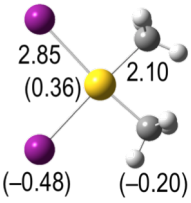 $[I_2–Au–(CH_3)_2]^-$ (**9**) | –2.69 |
| 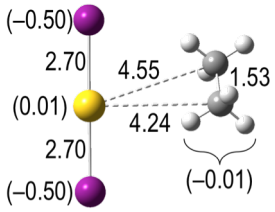 $[AuI_2^-\cdots(C_2H_6)]$ (**10**) | –4.62 |

[a] Numbers with/without parentheses indicate NBO charges/bond lengths (Å), respectively. [b] Relative total electronic energy with respect to $Au^- + 2CH_3I$. Color codes: yellow = Au, purple = I, gray = C, white = H.

4.61 eV, mainly due to formation of a C–C bond between two $CH_3$ ligands. A theoretical survey reveals that the second step of eq. 2.11 proceeds via several stable structures **8**–**10** and TSs as shown in Figure 2.13(b). Details of structural parameters (bond lengths and net charges on each atom) for structures **8**–**10** are summarized in Table 2.3. The conversion from **8** to **10** can be separated into two sequential steps: formation of **9** via oxidative addition of the second $CH_3I$ molecule to $[I–Au–CH_3]^-$ and reductive elimination of $C_2H_6$ from **9** leaving $AuI_2^-$. In the former step, the second $CH_3I$ weakly bound by $AuCH_3I^-$ in **8** undergoes oxidative addition via $S_N2$ attack and $I^-$ migration in a similar way to that of the first $CH_3I$ (Figure 2.7). However, the structure of the TS between **8** and **9** suggests the Walden inversion of the $CH_3$ group and migration of $I^-$ proceed simultaneously, in contrast to the sequential steps in the reaction of the first $CH_3I$. A similar mechanism was reported previously in a Pd-mediated oxidative addition.[9,10] In the latter step, structure **9** is converted to $AuI_2^-$ while releasing $C_2H_6$ as a coupling product. In the TS between **9** and **10**, two $CH_3$ ligands are located at a close distance to form a C–C bond.

At present, it cannot be concluded which pathway, eq. 2.10 or 2.11, is more dominant because their key intermediates such as $[I–Au–I–CH_3]^-$ and $[I_2–Au–(CH_3)_2]^-$ were not detected experimentally. However, from the thermodynamic and kinetic viewpoints, eq. 2.11 is more favorable than eq. 2.10 especially in the reaction with $CH_3I$, whereas eq. 2.11 is less important in the reaction with *t*-$C_4H_9I$ because of the steric hindrance by the bulky alkyl group.

## 2.4. Summary

In this chapter, I demonstrated that $Au^-$ is oxidatively inserted into the C–I bond in

$CH_3I$ to form a stable complex $[I–Au–CH_3]^-$. Theoretical studies of the reaction pathway indicated that this insertion proceeds in a sequential mechanism: nucleophilic attack of $Au^-$ on $CH_3I$, followed by migration of the leaving $I^-$ back to Au. This mechanism was verified by studying the steric effect. Sterically demanding *t*-$C_4H_9I$ increases the potential barrier for the $S_N2$ step, resulting in the photoelectron spectroscopic observation of the ion-neutral complex $[Au^-\cdots C_4H_9I]$. I theoretically considered two mechanisms of the $AuI_2^-$ formation from $Au^-$ and two $CH_3I$ molecules: (1) sequential abstraction of two I atoms from two $CH_3I$ molecules by $Au^-$ and (2) sequential oxidative addition of two $CH_3I$ molecules onto $Au^-$ followed by reductive elimination of $C_2H_6$. The latter pathway is energetically and kinetically more favorable, suggesting that $Au^-$ induces the C–C coupling reaction of $CH_3I$.

## References


1. Li, G.; Jin, R. *Nanotechnol. Rev.* **2012**, *2*, 529–545.
2. Han, J.; Liu, Y.; Guo, R. F. *J. Am. Chem. Soc.* **2009**, *131*, 2060–2061.
3. Kyriakou, G.; Beaumont, K. S.; Humphrey, S. M.; Antonetti, C.; Lambert, R. M. *ChemCatChem* **2010**, *2*, 1444–1449.
4. Corma, A.; Juárez, R.; Boronat, M.; Sánchez, F.; Iglesias, M.; García, H. *Chem. Commun.* **2011**, *47*, 1446–1448.
5. Karimi, B.; Esfahani, F. K. *Chem. Commun.* **2011**, *47*, 10452–10454.
6. Frisch, A. C.; Beller, M. *Angew. Chem., Int. Ed.* **2005**. *44*, 674–688.
7. Hashmi, A. S. K.; Hutchings, G. J. *Angew. Chem., Int. Ed.* **2006**, *45*, 7896–7936.
8. Chowdhury, A. K.; Wilkins, C. L. *J. Am. Chem. Soc.* **1987**, *109*, 5336–5343.
9. Bickelhaupt, F. M.; Ziegler, T.; von Ragué Schleyer, P. *Organometallics* **1995**, *14*, 2288–2296.
10. de Jong, G. T.; Bickelhaupt, F. M. *J. Chem. Theory Comput.* **2007**, *3*, 514–529.
11. Stille, J. K.; Lau, K. S. Y. *Acc. Chem. Res.* **1977**, *10*, 434–442.
12. Maeda, S.; Ohno, K. Morokuma, K. *Phys. Chem. Chem. Phys.* **2013**, *15*, 3683–3701.
13. Ohno, K. *Chem. Rec.* **2016**, *16*, 2198–2218.
14. Watanabe, T.; Tsukuda, T. *J. Phys. Chem. C* **2013**, *117*, 6664–6668.
15. Dietz, T. G.; Duncan, M. A.; Smalley, R. E. *J. Chem. Phys.* **1981**, *74*, 6511–6512.
16. Wiley, W. C.; McLaren, I. H. *Rev. Sci. Instrum.* **1955**, *26*, 1150–1157.
17. Kruit, P.; Read, F. H. *J. Phys. E.* **1983**, *16*, 313–324.
18. Cheshnovsky, G.; Yang, S. H.; Pettiette, C. L.; Craycraft, M. L.; Smalley, R. E. *Rev. Sci. Instrum.* **1987**, *58*, 2131–2137.
19. Markovich, G.; Pollack, S.; Giniger, R. Cheshnovsky, O. *J. Chem. Phys.* **1994**, *101*, 9344–9353.
20. Arnold, D. W.; Bradforth, S. E.; Kim, E. H. Neumark, D. M. *J. Chem. Phys.* **1995**, *102*, 3493–3509.
21. Handschuh, H.; Ganteför, G.; Bechthold, P. S.; Ebernhardt, W. A *J. Chem. Phys.* **1994**, *100*, 7093.
22. Tsukuda, T.; Saeki, M.; Iwata, S.; Nagata, T. *J. Phys. Chem. A* **1997**, *101*, 5103–5110.
23. Frisch, M. J.; Trucks, G. W.; Schlegel, H. B.; Scuseria, G. E.; Robb, M. A.; Cheeseman, J. R.; Scalmani, G.; Barone, V.; Mennucci, B.; Petersson, G. A.; Nakatsuji, H.; Caricato, M.; Li, X.; Hratchian, H. P.; Izmaylov, A. F.; Bloino, J.;

Zheng, G.; Sonnenberg, J. L.; Hada, M.; Ehara, M.; Toyota, K.; Fukuda, R.; Hasegawa, J.; Ishida, M.; Nakajima, T.; Honda, Y.; Kitao, O.; Nakai, H.; Vreven, T.; Montgomery, J. A., Jr.; Peralta, J. E.; Ogliaro, F.; Bearpark, M.; Heyd, J. J.; Brothers, E.; Kudin, K. N.; Staroverov, V. N.; Kobayashi, R.; Normand, J.; Raghavachari, K.; Rendell, A.; Burant, J. C.; Iyengar, S. S.; Tomasi, J.; Cossi, M.; Rega, N.; Millam, J. M.; Klene, M.; Knox, J. E.; Cross, J. B.; Bakken, V.; Adamo, C.; Jaramillo, J.; Gomperts, R.; Stratmann, R. E.; Yazyev, O.; Austin, A. J.; Cammi, R.; Pomelli, C.; Ochterski, J. W.; Martin, R. L.; Morokuma, K.; Zakrzewski, V. G.; Voth, G. A.; Salvador, P.; Dannenberg, J. J.; Dapprich, S.; Daniels, A. D.; Farkas, Ö.; Foresman, J. B.; Ortiz, J. V.; Cioslowski, J.; Fox, D. J. Gaussian 09, Revision C.01/D.01, Gaussian, Inc., Wallingford CT, 2013.

24. Becke, A. D. *J. Chem. Phys.* **1993**, *98*, 5648–5652.
25. Lee, C.; Yang, W.; Parr, R. G. *Phys. Rev. B: Condens. Matter Mater. Phys.* **1988**, *37*, 785–789.
26. P. J. Hay and W. R. Wadt, *J. Chem. Phys.* **1985**, *82*, 299–310.
27. Wadt, W. R; Hay, P. J. *J. Chem. Phys.* **1985**, *82*, 284–298.
28. Ditchfield, R.; Hehre, W. J.; Pople, J. A. *J. Chem. Phys.* **1971**, *54*, 724–728.
29. Hehre, W. J.; Ditchfield, R.; Pople, J. A. *J. Chem. Phys.* **1972**, *56*, 2257–2261.
30. Hariharan, P. C.; Pople, J. A. *Theo. Chim. Acta.* **1973**, *28*, 213–222.
31. Clark, T.; Chandrasekhar, J.; Spitznagel, G. W.; Schleyer, P. v. R. *J. Comp. Chem.* **1983**, *4*, 294–301.
32. Peng, C.; Ayala, P. Y.; Schlegel, H. B.; Frisch, M. J. *J. Comp. Chem.* **1996**, *17*, 49–56.
33. Reed, A. E.; Curtiss, L. A.; Weinhold, F. *Chem. Rev.* **1988**, *88*, 899–926.
34. Fukui, K. *J. Phys. Chem.* **1970**, *74*, 4161–4163.
35. Fukui, K. *Acc. Chem. Res.* **1981**, *14*, 363–368.
36. Ohno, K.; Maeda, S. *Chem. Phys. Lett.* **2004**, *384*, 277–282.
37. Maeda, S.; Ohno, K. *J. Phys. Chem. A* **2005**, *109*, 5742–5753.
38. Ohno, K.; Maeda, S. *J. Phys. Chem. A* **2006**, *110*, 8933–8941.
39. Maeda, S.; Ohno, K. *J. Phys. Chem. A* **2007**, *111*, 4527–4534.
40. Page, M; McIver Jr., J. W. *J. Chem. Phys.* **1988**, *88*, 922–935.
41. Page, M.; Doubleday Jr., C; McIver Jr., J. W. *J. Chem. Phys.* **1990**, *93*, 5634–5642.
42. Rijs, N. J.; Yoshikai, N.; Nakamura, E.; O'Hair, R. A. J. *J. Am. Chem. Soc.* **2012**, *134*, 2569–2580.
43. Strictly speaking, an IRC cannot be defined between **1** (or **2**) and the reactants ($Au^-$ + $CH_3I$) because a pair of the reactants is not located at a stationary point on the

potential energy surface. Thus, we herein considered the steepest descent path on the surface with mass-weighted coordinates, or meta-IRC (Tachibana, A.; Fukui, K. *Theor. Chim. Acta.* **1978**, *49*, 321–347.), from the pair of the reactants at a distance of ~8.0 Å.

44. Cho, H. G.; Andrews, L. *Inorg. Chem.* **2011**, *50*, 10319–10327.
45. Liu, H. T.; Xiong, X. G.; Dau, P. D.; Wang, Y. L.; Huang, Y. L.; Li, J.; Wang, L. S. *Nat. Commun.* **2013**, *4*, 2223.

# Chapter 3.

# Reaction of $CH_3I$ with other coinage metal anions, $Cu^-$ and $Ag^-$

A major part of this chapter has been published in the following paper.

Muramatsu, S.; Koyasu, K.; Tsukuda, T. *Chem. Lett.* **2017**, *46*, 676–679.

## 3.1. Introduction

Gas phase reactions of coinage metal (M = Cu, Ag, and Au) ions with small molecules have been studied extensively since the late 1970s[1–5] to gain fundamental insight into the catalytic performance of their organometallic complexes. Most of the studies have focused on the $M^+$ cations and much less is known about the reactivity of the $M^-$ anions because they are an exotic species in conventional chemistry.[6] However, several examples suggest the potential of $M^-$ as an interesting chemical species.[7–9] For instance, the reaction of dimethylmetallates $[CH_3MCH_3]^-$ (M = Cu, Ag) with allyl iodide ($CH_2$=$CHCH_2I$) yields $CH_3$–$C_3H_5$ via cross-coupling reaction.[7] In Chapter 2, I found that methyl iodide ($CH_3I$) undergoes oxidative addition to $Au^-$ to yield $[CH_3–Au–I]^-$, where an Au atom is inserted into the carbon–iodine (C–I) bond of $CH_3I$. I further proposed based on theoretical calculations that the oxidative addition proceeds via nucleophilic attack by $Au^-$ on $CH_3I$, followed by migration of the leaving $I^-$ to Au. In this chapter, I investigate the scope of this new reaction to anions of other coinage metals (Cu and Ag). Photoelectron spectroscopy (PES) and density functional theory (DFT) calculations show that Grignard reagent-like structures $[CH_3–M–I]^-$ are commonly formed in the reaction of $M^-$ and $CH_3I$, regardless of M.

## 3.2. Methods

### 3.2.1. Experiment

#### 3.2.1.1. Apparatus

The apparatus used in this study is shown in Figure 3.1. Basically it is the same as the apparatus shown in Figure 2.1 (Chapter 2) while some parts including the magnetic bottle were modified, which are described in detail in Section 3.2.1.2.

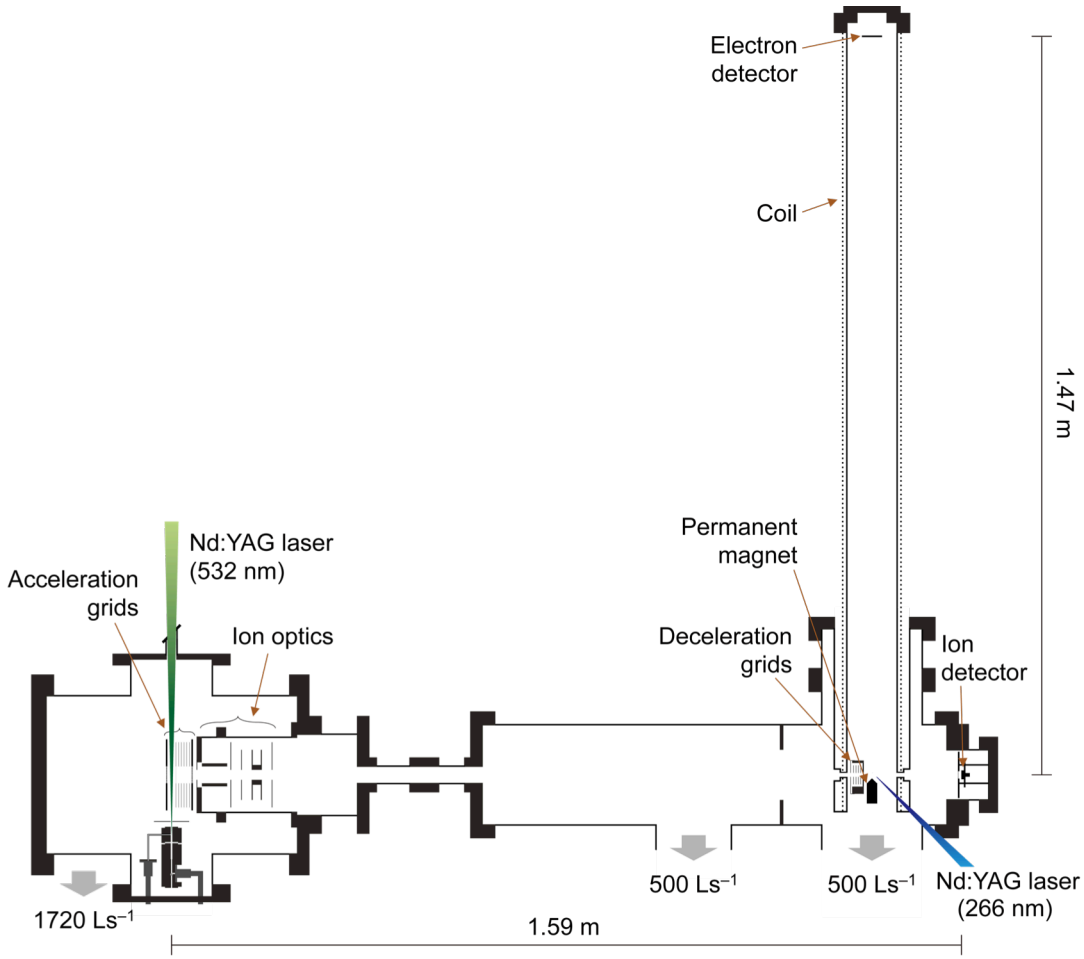


**Figure 3.1.** The experimental setup. Gray allows represent evacuation by turbo molecular pumps with the pumping speeds indicated.

### 3.2.1.2. Experimental procedure

The atomic coinage metal anion $M^-$ (M = Cu, Ag, Au) was generated by irradiating with a focused second harmonic output from a Nd:YAG laser (Spectra-Physics, INDI40) with typical pulse energy of 10–100 mJ/pulse onto a rotating and translating target rod of copper (Nilaco, purity: 99.99%, diameter: 5 mm, length: 18 mm), silver (Nilaco, purity: 99.99%, diameter: 5 mm, length: 18 mm) and gold (Nilaco, purity:

99.95%, diameter: 2 mm, length: 20 mm), respectively. The generated coinage metal anion $M^-$ containing a small amount of $M_2^-$ (typical ratio <5%) was introduced into a channel (diameter: 2 mm, length: 80 mm) by a flow of helium gas (purity: 99.999%) with backing pressure of 4.0–10 atm supplied through a pulsed valve (Parker Hannifin, series 9, injection orifice: 0.8 mm, pulse width 200–300 μs). Then, the generated ions were allowed to react with $CH_3I$ (Wako Pure Chemical Industries, purity: 99.5%) injected into the reaction cell by another pulse valve with/without dilution with helium gas (0–5.0 atm). The chemicals were used without further purification.

After the reaction, the anionic species were extracted perpendicularly and accelerated up to 3.0 keV by a pulsed electric field (DEI, PVX-4140, pulse duration: 10 μs, pulse rise time: ~50 ns), and analyzed by TOF-MS. The ratio of grid voltages was tuned[10] by the two identical power suppliers individually connected to each grid, which suppress the elongation of pulse rise time of the extractor grid as referred to in Chapter 2. The anions were detected by a microchannel plate (Hamamatsu Photonics, F4655-12). The signals were recorded and accumulated by a digital oscilloscope (Tectronix, TDS 580D) for typically 200–1000 laser shots. Resolution of the TOF-MS was ~400 at $m/z$ = 200 and ~340 at $m/z$ = 450; the improvement of the resolution compared to Chapter 2 is mainly attributed to short pulse rise time of the power suppliers of ion extractions.

Photoelectron spectra were recorded using a modified magnetic bottle. Magnitude of the acceleration voltage was set to 1.2–3.0 kV, and the anion of interest after mass-separation was decelerated by a pulsed electric field[11] (0–1.75 × $10^5$ $V \cdot m^{-1}$, pulse duration: 500 ns, Behlke, HTS 151-03-GSM) at 19 mm upstream from photodetachment region. Then it was irradiated with an unfocused 4th (266 nm, 4.66 eV) harmonics output from another Nd:YAG laser (Spectra-Physics, GCR-130) with

<0.4 mJ/pulse. The detached photoelectrons were guided by a magnetic field produced by a permanent magnet (~1000 G) and a solenoid coil (~40 G, number of turns: ~670 $m^{-1}$, current: 5.2 A) to a microchannel plate (El-Mul, Double MCP 33) located at 1.47 m from the photodetachment region. The signals were amplified 5-fold by a preamplifier (Stanford Research Systems, SR445) and counted by a multichannel scalar (Stanford Research Systems, SR430). The photoelectron spectra were obtained by

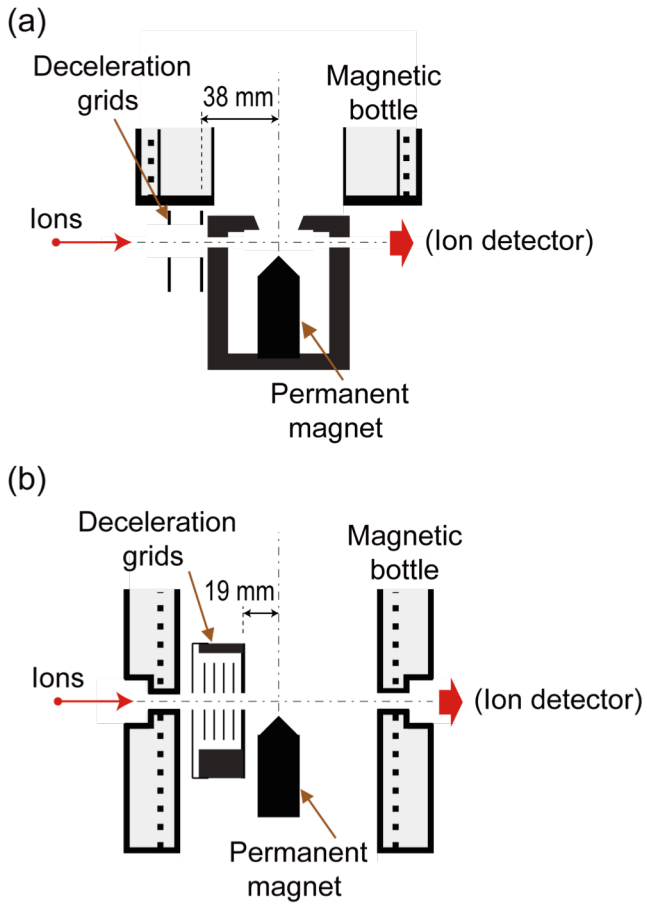


**Figure 3.2**. Expanded view of ion deceleration region and photodetachment region. (a) Previous setup in Chapter 2 and (b) current setup. Atmospheric pressure areas are hatched in gray while the other areas are evacuated to <~$10^{-5}$ Pa.

accumulations of 10,000–20,000 laser shots after background subtraction. The obtained spectra were smoothed by averaging the photoelectron counts of neighboring three points. The photoelectron kinetic energies were calibrated against the known photoelectron peaks of $I^-$ (ref. 12) generated by the dissociative electron attachment on $CH_3I$ molecules.[13] The resolution of the MB-PES was ~50 meV for electrons with a kinetic energy of 1.0 eV. The improvement of the resolution compared to Chapter 2 (Figure 3.2(a)) is mainly attributed to effective deceleration of anions due to the modified deceleration grids (Figure 3.2(b)); (1) five grids were stacked in parallel to

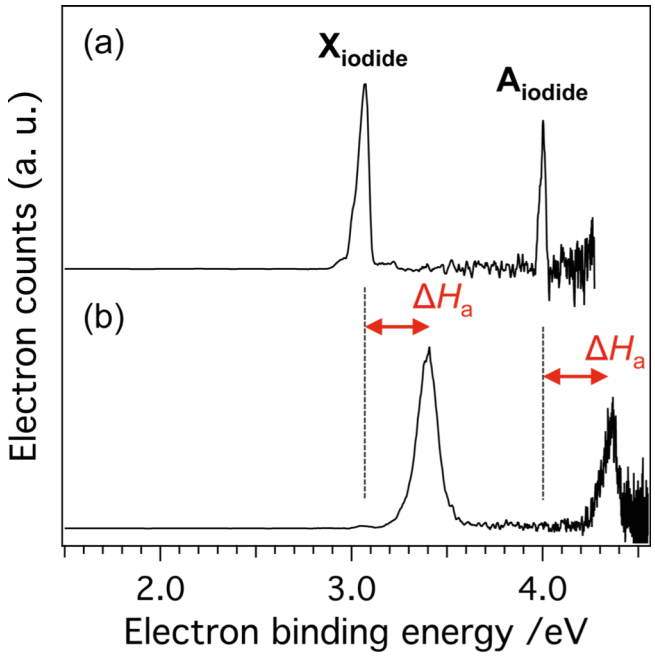


**Figure 3.3**. Photoelectron spectra of (a) $I^-$ and (b) $I^-(CH_3I)$ recorded at 266 nm. Two peaks in panel (a), $\mathbf{X_{iodide}}$ and $\mathbf{A_{iodide}}$, correspond to photodetachment represented as $I^0$ ($^2P_{3/2}$) ← $I^-$ ($^1S_0$) and $I^0$ ($^2P_{1/2}$) ← $I^-$ ($^1S_0$), respectively. Panel (b) exhibits a doublet pattern similar to that in panel (a), with identical blue shifts by $\Delta H_a$ ~ 0.38 eV. $\Delta H_a$ corresponds to binding enthalpy attributed to ion-dipole interaction.[14]

produce uniform pulsed electric field and (2) distance between deceleration region and photodetachment region was reduced to 19 mm to minimize the broadening of the ion bunch. Another important improvement is that length of the coil was increased to cover the photodetachment region, which is expected to produce smooth magnetic field (Figure 3.2(b)). The new magnetic bottle has enough sensitivity at higher binding energy region (> ~4 eV), which was confirmed by quantitative reproduction of a photoelectron spectrum of $I^-(CH_3I)$ as shown in Figure 3.3.[14]

### 3.2.2. Computation

Electronic and geometrical structures of the detected species were studied by density functional theory (DFT) calculations using Gaussian 09 program.[15] The hybrid functional B3LYP[16,17] was used for all calculations in this chapter. Basis sets used were aug-cc-pVTZ-PP for Cu, Ag, Au, and I atoms, and aug-cc-pVTZ for H and C atoms[18–20] (from the EMSL Basis Set Exchange Database[21,22]).

Structural optimization[23] was carried out followed by frequency calculations to check whether the optimized structure was a local minimum structure (LM). Total electronic energy of each calculated structure is shown with vibrational zero-point energy (ZPE) correction. The electron vertical detachment energy (VDE) of each LM was estimated from the energy difference between the ground state of the anion and that of neutral for the anion structure without ZPE correction. Atomic charges for LMs and TSs were evaluated by natural population analysis based on natural bond orbitals (NBOs).[24] The reaction pathways (transition state structures (TSs) and intrinsic reaction coordinates (IRCs)) were explored using Gaussian 09[15] and GRRM11[25–28] programs.

## 3.3. Results and discussion

### 3.3.1. Oxidative addition of $CH_3I$ to $M^-$ (M = Cu, Ag, Au)

#### 3.3.1.1. Formation of adduct product $MCH_3I^-$

Figures 3.4(a)–(c) show typical mass spectra after the reactions of $M^-$ (M = Cu, Ag, and Au) with $CH_3I$. The $M^-$ reactants almost disappear after the reaction. In addition to the major products $I^-$ and $MI_2^-$,[29,30] the adduct species $MCH_3I^-$ is commonly produced in all the metals. The assignment of $MCH_3I^-$ is confirmed by the comparison of isotope patterns experimentally observed and theoretically calculated as shown in Figure 3.5. Wilkins previously reported that $I^-$ was exclusively produced via slow $S_N2$ attack by $Au^-$ on $CH_3I$.[5] The key to the successful observation of $MCH_3I^-$ adducts in our

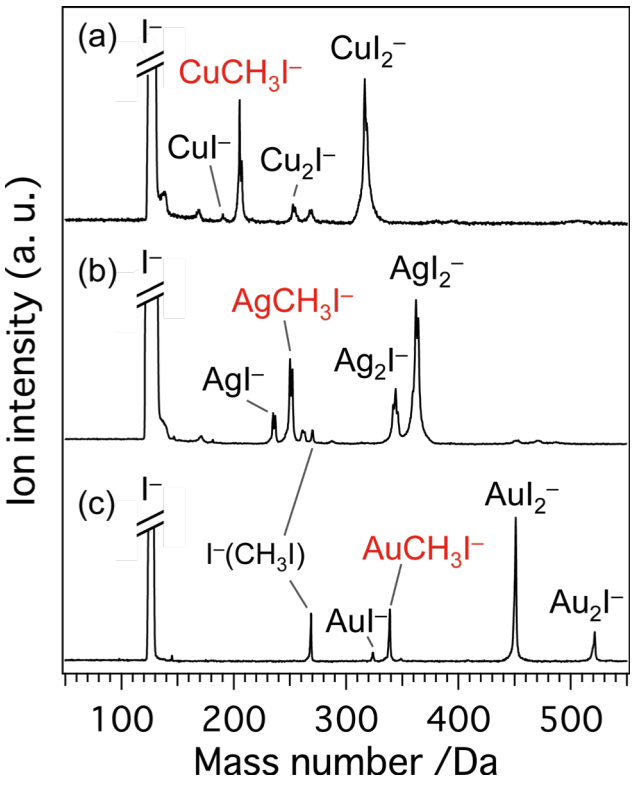


**Figure 3.4.** Mass spectra of gas phase reaction products of $CH_3I$ and (a) $Cu^-$, (b) $Ag^-$, (c) $Au^-$.

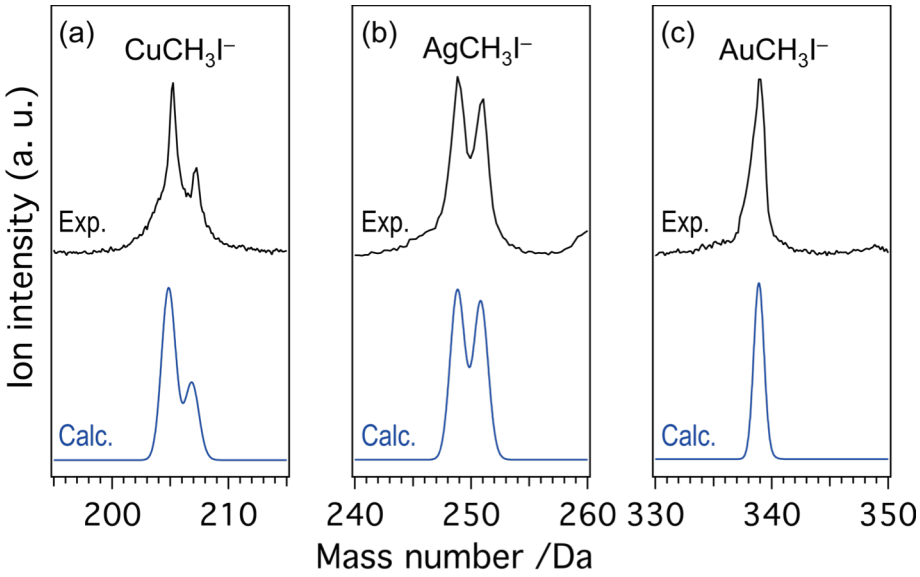


**Figure 3.5.** Comparison of isotopic patterns of mass peaks of $MCH_3I^-$ experimentally observed (black) and theoretically calculated (blue). M = (a) Cu, (b) Ag, (c) Au.

experiment is effective cooling of the reaction products via multiple collisions in the gas cell, as discussed in Chapter 2.

### 2.3.1.2. Structural determination of $MCH_3I^-$

Electronic structures of the $MCH_3I^-$ products were studied by PES. Figures 3.6(a), (b), and (c) show typical photoelectron spectra of $MCH_3I^-$ with M = Cu, Ag, and Au, respectively. The spectra exhibit a weak and broad band ($\mathbf{X_1}$) at the low binding energy region (1.8–2.5 eV), followed by strong and sharp bands ($\mathbf{X_2}$, **A**, ...) at the high binding energy region (>3.5 eV). Similar spectral patterns between $MCH_3I^-$ (M = Cu, Ag, Au) suggest a common structure motif regardless of M. Table 3.1 summarizes the band positions determined by fitting the spectra with Gaussian functions. The peak-top positions of the fitting Gaussian functions are regarded as VDE; the VDEs for the bands

$\mathbf{X_1}$ are 1.81, 2.03, 2.45 eV for M = Cu, Ag, and Au, respectively. The VDE value increases with an increase in the mass of the metal. This trend is also observed for the bands $\mathbf{X_2}$. The VDE values for the $\mathbf{X_1}$, $\mathbf{X_2}$, **A**, and **B** bands are summarized in Table 3.1.

Table 3.2 summarizes the optimized structures of $MCH_3I^-$. Three types of local minimum structures were obtained. The optimized structures of $AuCH_3I^-$ are nearly the same as those in Chapter 2 where smaller basis sets were used. For all metals, the most

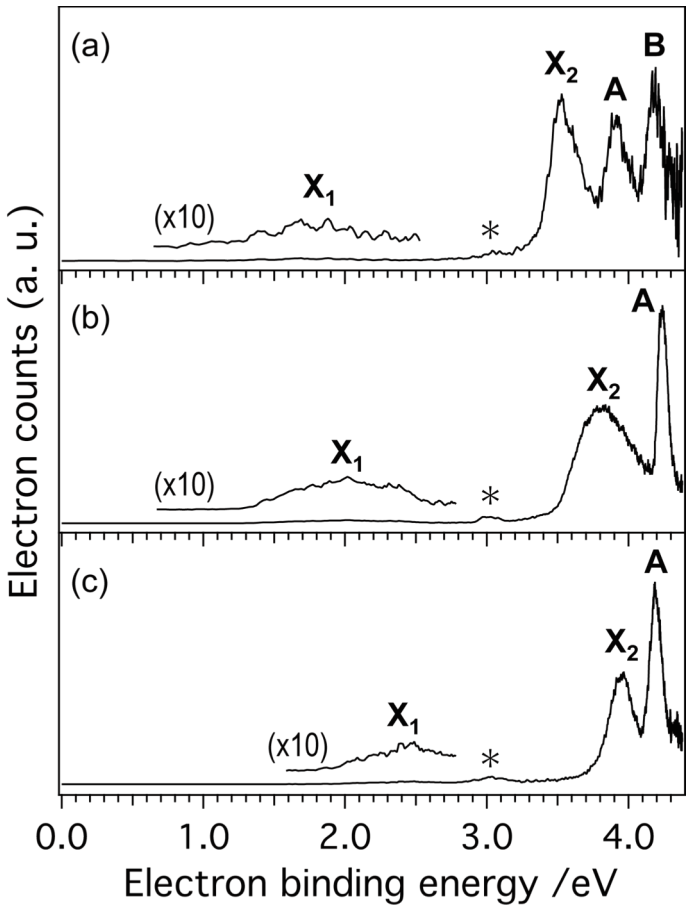


**Figure 3.6**. Photoelectron spectra of (a) $CuCH_3I^-$, (b) $AgCH_3I^-$, (c) $AuCH_3I^-$. The peaks with asterisks originate from $I^-$ contaminated in the mass-selected $MCH_3I^-$ beams (see text for more detail).

**Table 3.1. Experimental Vertical Detachment Energies (VDEs) for $MCH_3I^-$ (M = Cu, Ag, Au).**

| Products | $VDE_{exp}$ /eV | | | |
|---|---|---|---|---|
| | **$X_1$** | **$X_2$** | **A** | **B** |
| $CuCH_3I^-$ | 1.81 | 3.53 | 3.91 | 4.19 |
| $AgCH_3I^-$ | 2.03 | 3.82 | 4.24 | - |
| $AuCH_3I^-$ | 2.45 | 3.95 | 4.19 | - |

stable structures are described as $[CH_3–M–I]^-$, in which the metal atom is inserted into the C–I bond of $CH_3I$ in a linear configuration. In this structure, the NBO charges on M = Cu, Ag, and Au were calculated to be 0.28|e|, 0.28|e|, and 0.09|e|, respectively. Since the NBO charges on M increase from –1.0|e| after the reaction, $[CH_3–M–I]^-$ can be viewed as oxidative addition products. The second most stable isomers are ion-neutral complexes $[I^-\cdots CH_3M]$, in which the $CH_3M$ molecule is electrostatically bound to $I^-$ while pointing its dipole moment. The least stable isomers are $[CH_3–I–M]^-$, in which $CH_3I$ is coordinated to the metal from the I side. The electronic charge is distributed over the molecular framework and, as a result, the C–I bond is slightly elongated compared to that of $CH_3I$ (2.16 Å).

The relative intensity of bands $\mathbf{X_1}$ and $\mathbf{X_2}$ was dependent on the source conditions, such as the pressure of the carrier gas and dilution gas in the $CH_3I$ reservoir, as shown in Figure 3.7. This observation led us to assign bands $\mathbf{X_1}$ and $\mathbf{X_2}$ to structural isomers. The experimental VDE values of the more intense $\mathbf{X_2}$ bands monotonically increase in the order of Cu, Ag, and Au (Table 3.1). This trend was not reproduced by the calculated VDE values of the second most stable isomers $[I^-\cdots CH_3M]$, but by those of

the most stable isomers $[CH_3–M–I]^-$. In addition, the VDEs calculated for $[CH_3–M–I]^-$ agree with the experimental values of $\mathbf{X_2}$ within the energy of 0.2 eV. Based on these considerations, we assigned the $\mathbf{X_2}$ bands to the most stable isomers $[CH_3–M–I]^-$. On

**Table 3.2. Structural Candidates for $MCH_3I^-$ (M = Cu, Ag, Au).**[a]

| | $[CH_3–Cu–I]^-$ | $[I^-\cdots CH_3Cu]$ | $[CH_3–I–Cu]^-$ |
|---|---|---|---|
| Structure | 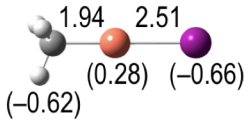 | 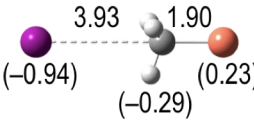 | 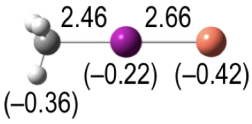 |
| $\Delta E$ /eV | 0 | 1.70 | 2.81 |
| Exothermicity /eV[b] | 3.47 | 1.77 | 0.66 |
| $VDE_{calc}$ /eV[c] | 3.43 | 3.32 | 1.83 |
| $VDE_{exp}$ /eV[c] | 3.53 ($\mathbf{X_2}$) | | 1.81 ($\mathbf{X_1}$) |
| | $[CH_3–Ag–I]^-$ | $[I^-\cdots CH_3Ag]$ | $[CH_3–I–Ag]^-$ |
| Structure | 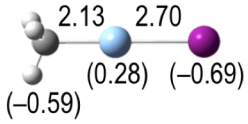 | 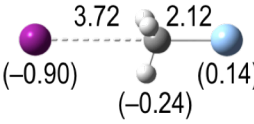 | 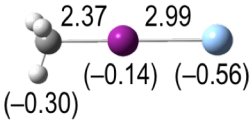 |
| $\Delta E$ /eV | 0 | 1.55 | 2.25 |
| Exothermicity /eV[b] | 2.72 | 1.17 | 0.47 |
| $VDE_{calc}$ /eV[c] | 3.78 | 3.15 | 1.83 |
| $VDE_{exp}$ /eV[c] | 3.82 ($\mathbf{X_2}$) | | 2.03 ($\mathbf{X_1}$) |
| | $[CH_3–Au–I]^-$ | $[I^-\cdots CH_3Au]$ | $[CH_3–I–Au]^-$ |
| Structure | 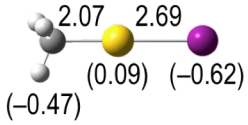 | 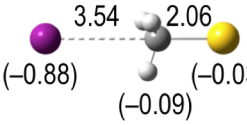 | 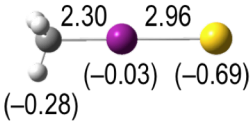 |
| $\Delta E$ /eV | 0 | 1.43 | 2.13 |
| Exothermicity /eV[b] | 2.59 | 1.16 | 0.46 |
| $VDE_{calc}$ /eV[c] | 4.06 | 3.58 | 2.60 |
| $VDE_{exp}$ /eV[c] | 3.95 ($\mathbf{X_2}$) | | 2.45 ($\mathbf{X_1}$) |

[a] Numbers with and without parentheses indicate the NBO charges of M, I and $CH_3$ and the bond lengths in units of Å, respectively. [b] With respect to $M^-$ + $CH_3I$ with ZPE correction. [c] Electron vertical detachment energy. Color codes: brown = Cu, blue = Ag, yellow = Au, purple = I, gray = C, white = H.

the other hand, the much weaker $\mathbf{X_1}$ bands were assigned to the least stable isomers $[CH_3–I–M]^-$ based on their calculated VDE values. The VDE values of bands **A** and **B** are significantly larger than those calculated for the remaining isomers $[I^-\cdots CH_3M]$. Thus, they are probably associated with electron detachment from the most dominant isomers $[CH_3–M–I]^-$ to form the corresponding neutral species in electronically excited states. Especially assignments of bands **A** are supported by the constant intensity ratio of bands $\mathbf{X_2}$ and **A** under the different source conditions as shown in Figure 3.7. Namely, photoelectron bands of the second most stable isomers $[I^-\cdots CH_3M]$ were not observed. The absence of $[I^-\cdots CH_3M]$ is attributed to a low activation barrier for the migration of $I^-$ to M as discussed later (Figure 3.10).

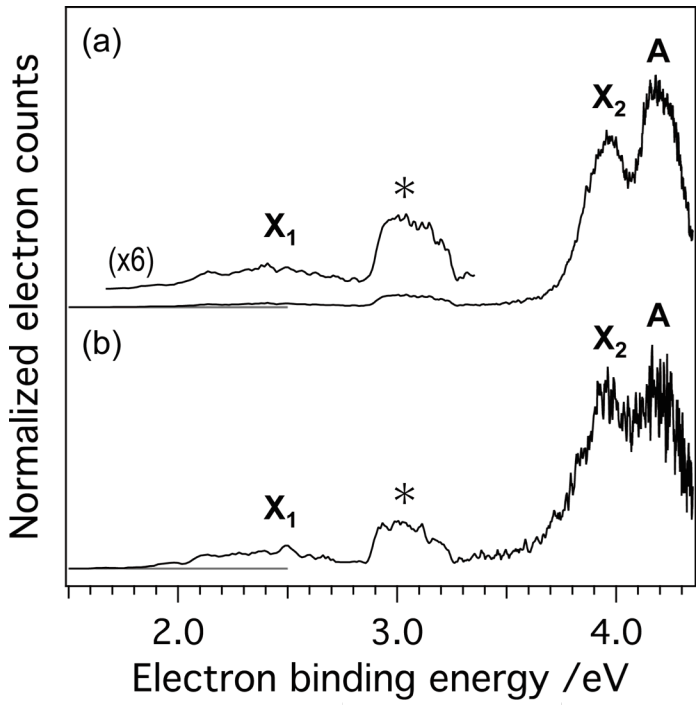


**Figure 3.7**. Photoelectron spectra of $AuCH_3I^-$ recorded under different source conditions. The pressure of He used for carrier gas and for diluting $CH_3I$ vapor in a reservoir was (a) 0.5 and 0.0 MPa, (b) 0.65 and 0.5 MPa, respectively. Spectral intensities are normalized at the band $\mathbf{X_2}$.

Small peaks can be seen at ~3.1 eV marked with the asterisks in Figures 3.6(a)–(c). These were assigned to $I^-$ (electron affinity of I atom: 3.06 eV[31]) contained in the mass-selected $MCH_3I^-$ beam. Two scenarios are possible for the contamination of the $MCH_3I^-$ beam with $I^-$: (1) unimolecular dissociation of $MCH_3I^-$ during the flight in the field-free region of the TOF mass spectrometer, or (2) photodissociation of $MCH_3I^-$ induced by the photodetachment laser. The more plausible scenario was identified by studying the laser power dependence of the photoelectron band intensity at ~3.1 eV since the number of photons involved is different for the above processes. The intensity ratio between the peaks of $I^-$ and the others was not dependent on the laser fluence, as

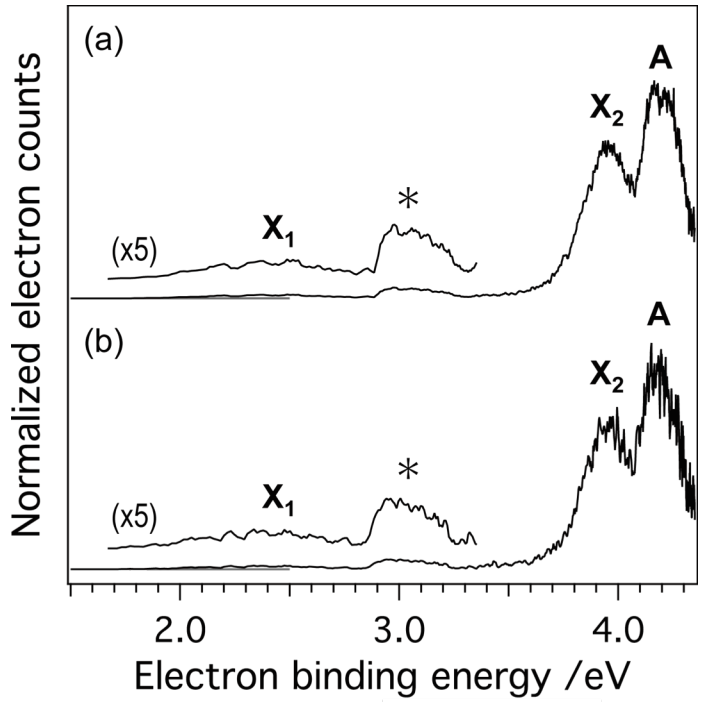


**Figure 3.8**. Photoelectron spectra of $AuCH_3I^-$ recorded under different fluences of the photodetachment laser; (a) ~2.6 and (b) ~0.3 mJ/cm$^2$·pulse. Spectral intensities are normalized at the band $\mathbf{X_2}$.

shown in Figures 3.8(a) and (b). This result indicates that $I^-$ contaminated the beam via unimolecular dissociation of $MCH_3I^-$. This conclusion is supported by the detection of a neutral counterpart (most probably $AuCH_3^0$) in the unimolecular dissociation of $AuCH_3I^-$ by applying a retarding electric field in front of the detector as shown in

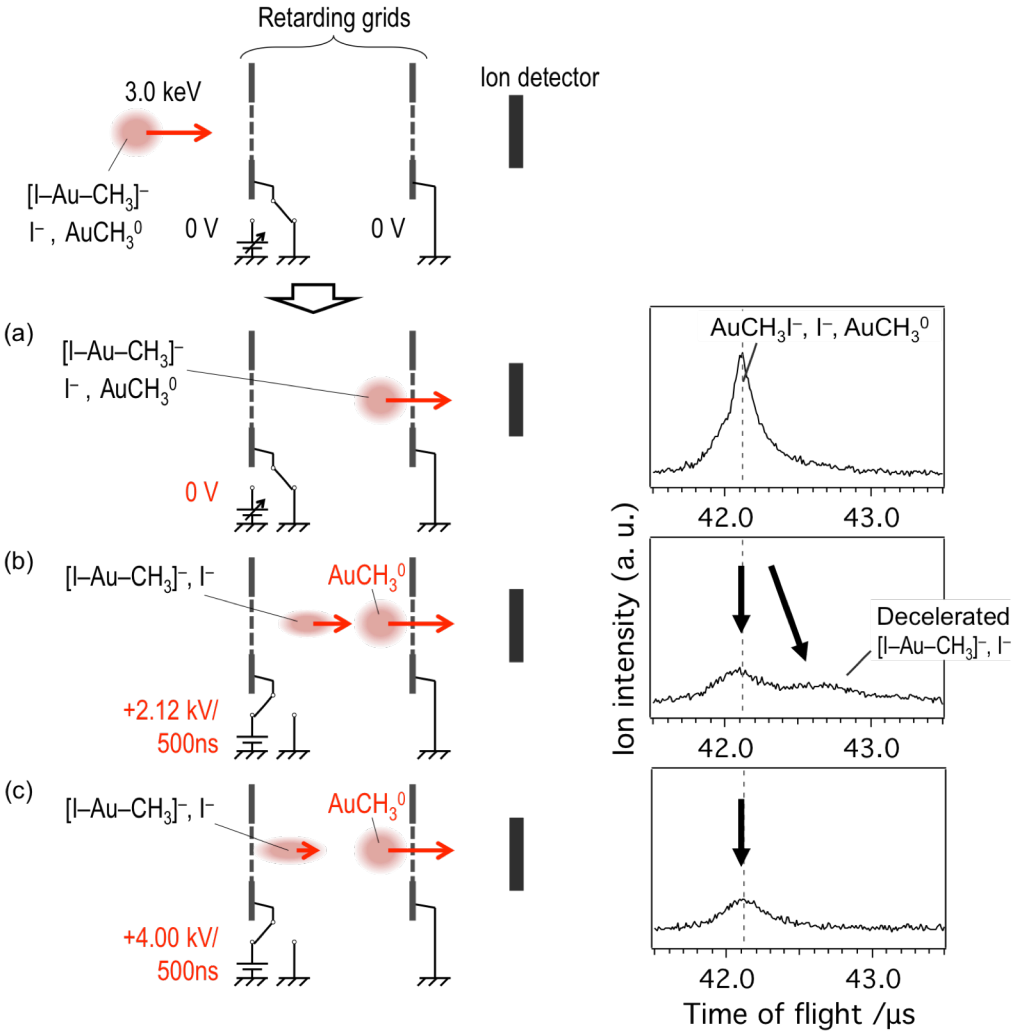


**Figure 3.9.** Time-of-flight mass spectra after deceleration of ion bunch of $AuCH_3I^-$ by applying retarding fields in front of the detector (see Figure 3.1). Schematic illustration of deceleration is shown in the column on the left. Kinetic energy of the initial $AuCH_3I^-$ ions was 3.0 keV. Deceleration voltage and pulse duration are (a) 0 V / 0 s, (b) 2.12 kV / 500 ns, (c) 4.00 kV / 500 ns. Dotted line indicates the position of $AuCH_3I^-$ peak in panel (a).

Figure 3.9. The occurrence of unimolecular dissociation suggests that $MCH_3I^-$ was produced via highly exothermic processes.

### 3.3.1.3. Reaction mechanism

This section focuses on the formation mechanism of the main products $[CH_3–M–I]^-$. Figure 3.10 shows the energy profiles calculated for the formation of $[CH_3–M–I]^-$ via eq. 3.1 along IRCs.

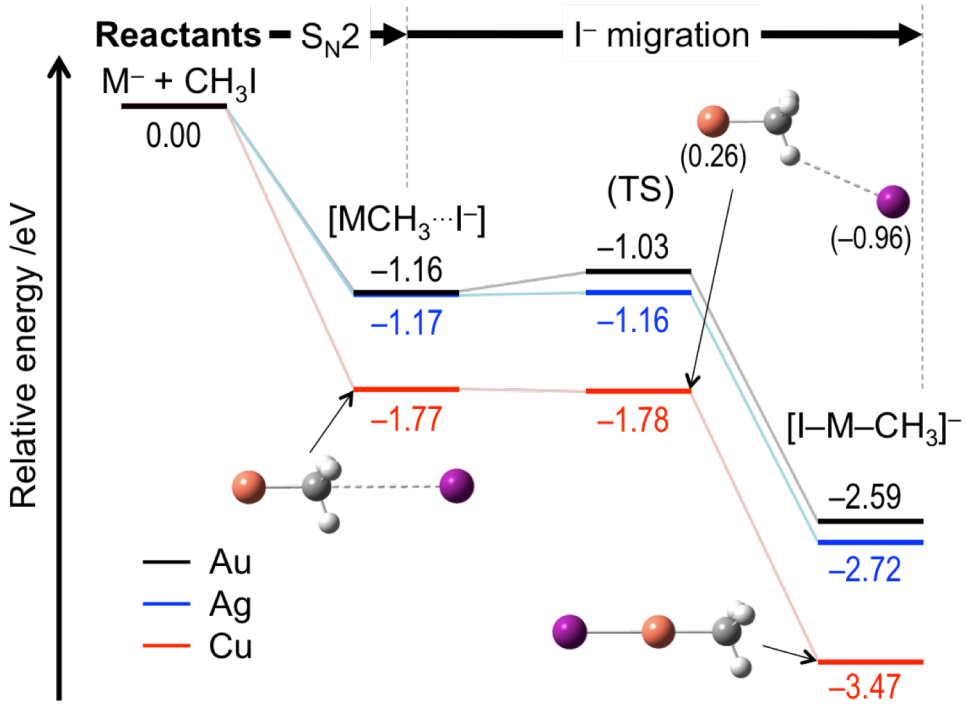


**Figure 3.10.** Energy profiles along the formation pathway of $[I–M–CH_3]^-$ from $M^-$ + $CH_3I$. TS represents a transition state. All energies are ZPE-corrected and shown with respect to $M^-$ + $CH_3I$. Black, blue and red represent M = Au, Ag, and Cu, respectively. Each structure is connected by IRCs. Optimized structures of Cu complexes are shown as an example. Note that intermediates and products are described as $[MCH_3\cdots I^-]$ and $[I–M–CH_3]^-$, respectively, to demonstrate the reaction mechanism. Color codes: brown = Cu, purple = I, gray = C, white = H.

$$M^- + CH_3I \rightarrow [CH_3\text{–}M\text{–}I]^- \quad (3.1)$$

Similar to the previous study for $[CH_3\text{–}Au\text{–}I]^-$ in Chapter 2, it was indicated that $[CH_3\text{–}M\text{–}I]^-$ (M = Cu, Ag) products are also formed via the intermediates $[MCH_3\cdots I^-]$, followed by migration of the leaving $I^-$ to M. Figure 3.11 shows that the electronic energy profile as a function of the distance between $M^-$ and $CH_3I$ has barrierless

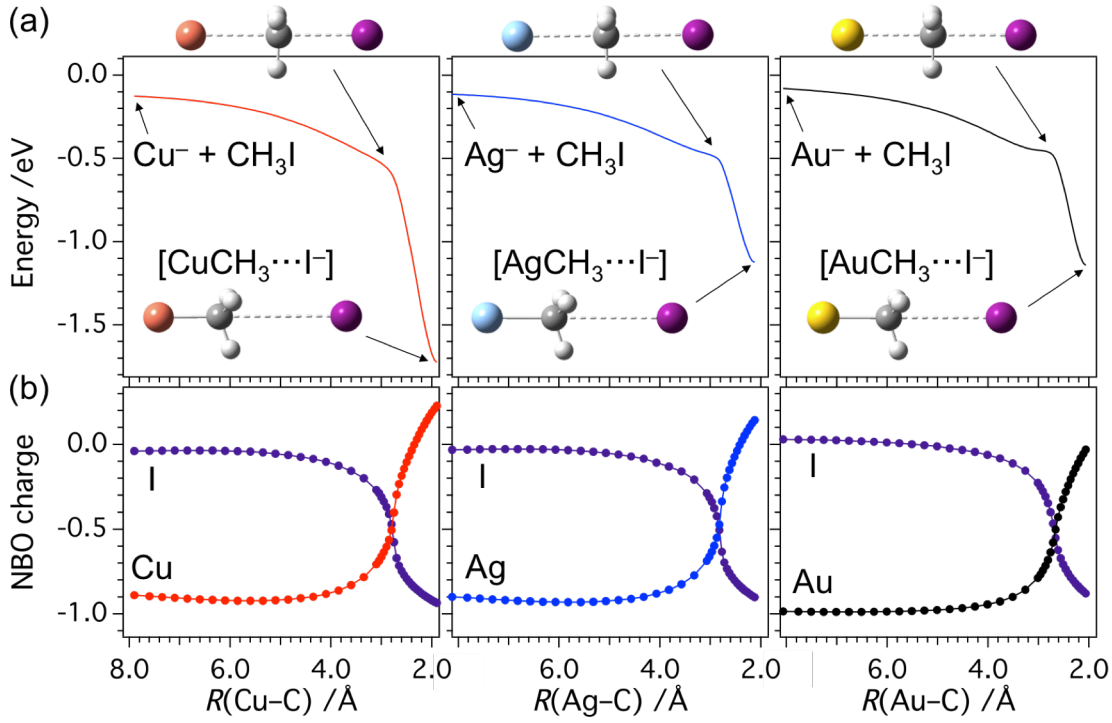


**Figure 3.11.** Profiles of (a) electronic energies without ZPE correction and (b) NBO charges of M (M = Cu, Ag, Au) and I atoms as a function of the distance between M and C atoms ($R$(M–C)). Energies are shown with respect to the reactants ($M^- + CH_3I$) at the infinite distance. Insets show the structures of $[M\cdots CH_3\cdots I]^-$ in which the methyl group is planer and $[MCH_3\cdots I^-]$ in which $MCH_3$ is bound by $I^-$. Note that the formula $[MCH_3\cdots I^-]$ is used to indicate the steric inversion via $S_N2$ process. Color code: brown = Cu, blue = Ag, yellow = Au, purple = I, gray = C, white = H.

feature and that the NBO charge on $M^-$ is transferred to I atom at a certain distance. These results suggest that the formation of $[MCH_3\cdots I^-]$ proceeds via nucleophilic attack by $M^-$ against $CH_3I$. The barrier heights for the $I^-$ migration are negligibly smaller than the exothermicity associated with the formation of the $[MCH_3\cdots I^-]$ intermediates via the $S_N2$ step. This implies that the migration step proceeds efficiently and explains the absence of bands of $[MCH_3\cdots I^-]$ in the photoelectron spectra. The barrierless profiles in total suggest that $[CH_3–M–I]^-$ is easily formed when $CH_3I$ encounters $M^-$.

### 3.3.2. Comparison of stability of the products

The high stability of $[CH_3–M–I]^-$ products is explained by the large exothermicity in the formation processes of eq. 3.1. Especially, the order of the exothermicity, which is formally identical to dissociation energy to $M^- + CH_3I$, is considered to reflect the relative thermodynamic stability between the products; it increases in the order of Au < Ag < Cu as listed in Table 3.2. Previous theoretical study on neutral $[CH_3–M–X]$ complexes (X = F, Cl, Br and I)[32] showed that the stability is in the order of $[CH_3–Ag–X] < [CH_3–Au–X] < [CH_3–Cu–X]$ on the basis of exothermicity in the formation from $M + CH_3X$. The difference in the order between neutral and anionic states can be understood from electron affinity of M; the small electron affinity of Ag (1.30 eV[33]) compared to Au (2.31 eV[34]) makes $Ag^-$ anion less stable and easy to form $[CH_3–Ag–I]^-$ with larger exothermicity. The quite high stability of $[CH_3–Cu–I]^-$ can be explained from the two aspects: (1) the highest stability in the neutral state and (2) the lowest electron affinity of Cu (1.24 eV[33]) among the coinage metals.

The metal-inserted structures of $[CH_3–M–I]^-$ remind us of the typical Grignard reagent $CH_3–Mg–I$. The thermodynamic stability of $CH_3MgI$ with respect to $Mg + CH_3I$

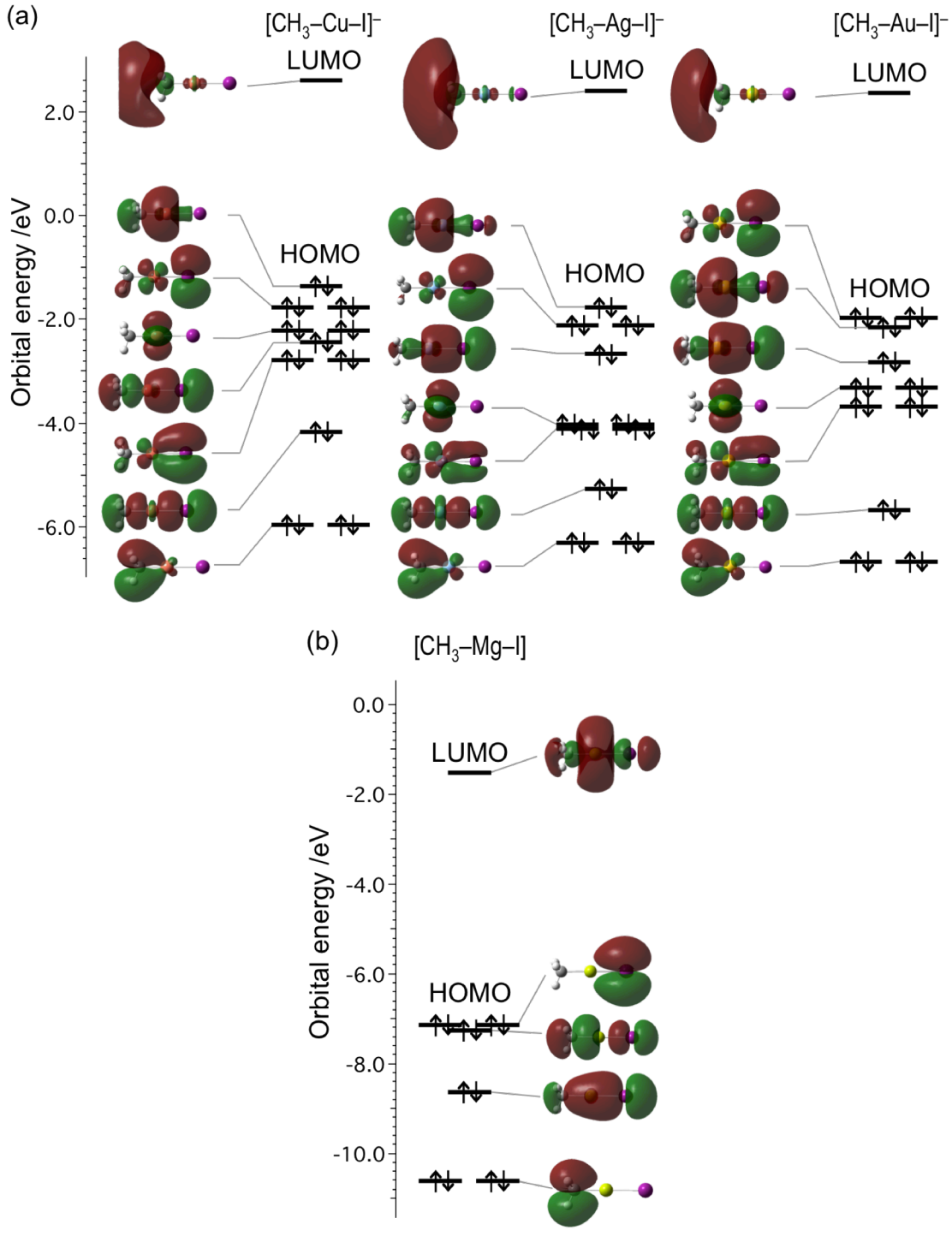


**Figure 3.12.** Energy levels and charge density surfaces of the Kohn-Sham orbitals of (a) $[CH_3–M–I]^-$ (M = Cu, Ag, Au) and (b) $CH_3MgI$. The isodensity value is 0.015 for LUMO of $[CH_3–Ag–I]^-$, 0.018 for LUMOs of $[CH_3–Cu–I]^-$ and $[CH_3–Au–I]^-$, and 0.020 for the other orbitals.

was obtained as 2.14 eV by DFT calculations at the same computational level (B3LYP/aug-cc-pVTZ-PP for I and aug-cc-pVTZ for C, H, and Mg). That is, the thermodynamic stabilities of $[CH_3–M–I]^-$ (M = Au, Ag, and Cu) are larger than that of $CH_3MgI$. Figures 3.12(a) and (b) compare the frontier Kohn-Sham orbitals of $[CH_3–M–I]^-$ and $CH_3MgI$. The d orbitals of the Cu/Ag atoms are mainly involved in the bonding with I and $CH_3$ ligands, similar to Au atom as discussed in Chapter 2 (Figure 2.9). In contrast, Mg atom makes bonds with the ligands using 2s orbitals. The high stability of $[CH_3–M–I]^-$ is considered to arise from the strong interaction between the d orbitals of the coinage metal atoms and the I and $CH_3$ ligands; the considerable overlaps of 5d orbitals of Au with halogen atoms[35] and alkynyl (C≡CH) ligands[36] are reported for similar compounds. A $[CF_3AuX]^-(PPh_4)^+$ compound was recently synthesized in the condensed phase and single-crystal X-ray diffraction confirmed the linear C–Au–X structure in $[CF_3AuX]^-$.[37,38]

It is known that the $CH_3$ group in $CH_3MgI$ has a carbanionic nature, which is essential to the C–C bond formation in Grignard reactions. NBO charges on the $CH_3$ group of $[CH_3–M–I]^-$ were calculated to be −0.62|e|, −0.59|e|, and −0.47|e| for M = Cu, Ag, and Au, respectively (Table 3.2). These values are comparable to that of $CH_3MgI$ (−0.65|e|). The carbanionic nature of the $CH_3$ group of $[CH_3–M–I]^-$ suggests that the C–C bond forming reaction is possible by the subsequent reductive elimination. In Chapter 2, it was theoretically proposed that $[CH_3–Au–I]^-$ undergoes a nucleophilic attack on $CH_3I$ followed by C–C bond formation to yield $C_2H_6$.

## 3.4. Summary

I conclude from the experimental and theoretical results that Grignard reagent-like

coinage metal complexes $[CH_3–M–I]^-$ (M = Cu, Ag, Au) are formed by the gas phase reactions between $M^-$ and $CH_3I$, regardless of M. Similar chemical properties of $M^-$ are due to the common electronic configuration; fully occupied d orbitals and two s electrons represented as $(n–1)d^{10}(ns)^2$ ($n$ = 4, 5, and 6 for Cu, Ag, and Au, respectively). DFT calculations showed that the thermodynamic stability increases in the order of $[CH_3–Au–I]^- < [CH_3–Ag–I]^- < [CH_3–Cu–I]^-$, which is significantly greater than that of the conventional Grignard reagent $CH_3MgI$. The large stability of $[CH_3–M–I]^-$ is attributed to the strong bonding interaction of the d orbitals of metals with I and $CH_3$ ligands. The anionic nature of the $CH_3$ group in $[CH_3–M–I]^-$ suggests that the C–C bond forming reaction can be promoted as in the alkylation reactions by Grignard reagents. This study suggests that $[R–M–I]^-$ can be a useful reagent in organic synthesis.

## References


1. Burnier, R. C.; Carlin, T. J.; Reents, W. D., Jr.; Cody, R. B.; Lengel, R. K.; Freiser, B. S. *J. Am. Chem. Soc.* **1979**, *101*, 7127–7129.
2. McLuckey, S. A.; Schoen, A. E.; Cooks, R. G. *J. Am. Chem. Soc.* **1982**, *104*, 848–850.
3. Jones, R. W.; Staley, R. H. *J. Phys. Chem.* **1982**, *86*, 1669–1674.
4. Weil, D. A.; Wilkins, C. L. *J. Am. Chem. Soc.* **1985**, *107*, 7316–7320.
5. Chowdhury, K. Wilkins, C. L. *J. Am. Chem. Soc.* **1987**, *109*, 5336–5343.
6. Jansen, M. *Chem. Soc. Rev.* **2008**, *37*, 1826–1835.
7. Rijs, N. J.; Yoshikai, N.; Nakamura, E.; O'Hair, R. A. J. *J. Am. Chem. Soc.* **2012**, *134*, 2569–2580.
8. Kimble, M. L.; Castleman, A. W., Jr.; Mitrić, R.; Bürgel, C.; Bonačić-Koutecký, V. *J. Am. Chem. Soc.* **2004**, *126*, 2526–2535.
9. Li, X. N.; Yuan, Z.; He, S. G. *J. Am. Chem. Soc.* **2014**, *136*, 3617–3623.
10. Wiley, W. C.; McLaren, I. H. *Rev. Sci. Instrum.* **1955**, *26*, 1150–1157.
11. Markovich, G.; Pollack, S.; Giniger, R. Cheshnovsky, O. *J. Chem. Phys.* **1994**, *101*, 9344–9353.
12. Arnold, D. W.; Bradforth, S. E.; Kim, E. H. Neumark, D. M. *J. Chem. Phys.* **1995**, *102*, 3493–3509.
13. Tsukuda, T.; Saeki, M.; Iwata, S.; Nagata, T. *J. Phys. Chem. A*, **1997**, *101*, 5103–5110.
14. Cyr, D. M.; Scarton, M. G.; Johnson, M. A. *J. Chem. Phys.* **1993**, *99*, 4869–4872.
15. Frisch, M. J.; Trucks, G. W.; Schlegel, H. B.; Scuseria, G. E.; Robb, M. A.; Cheeseman, J. R.; Scalmani, G.; Barone, V.; Mennucci, B.; Petersson, G. A.; Nakatsuji, H.; Caricato, M.; Li, X.; Hratchian, H. P.; Izmaylov, A. F.; Bloino, J.; Zheng, G.; Sonnenberg, J. L.; Hada, M.; Ehara, M.; Toyota, K.; Fukuda, R.; Hasegawa, J.; Ishida, M.; Nakajima, T.; Honda, Y.; Kitao, O.; Nakai, H.; Vreven, T.; Montgomery, J. A., Jr.; Peralta, J. E.; Ogliaro, F.; Bearpark, M.; Heyd, J. J.; Brothers, E.; Kudin, K. N.; Staroverov, V. N.; Kobayashi, R.; Normand, J.; Raghavachari, K.; Rendell, A.; Burant, J. C.; Iyengar, S. S.; Tomasi, J.; Cossi, M.; Rega, N.; Millam, J. M.; Klene, M.; Knox, J. E.; Cross, J. B.; Bakken, V.; Adamo, C.; Jaramillo, J.; Gomperts, R.; Stratmann, R. E.; Yazyev, O.; Austin, A. J.; Cammi, R.; Pomelli, C.; Ochterski, J. W.; Martin, R. L.; Morokuma, K.; Zakrzewski, V. G.; Voth, G. A.; Salvador, P.; Dannenberg, J. J.; Dapprich, S.; Daniels, A. D.; Farkas, Ö.; Foresman, J. B.; Ortiz, J. V.; Cioslowski, J.; Fox, D. J.

Gaussian 09, Revision C.01/D.01, Gaussian, Inc., Wallingford CT, 2013.
16. Becke, A. D. *J. Chem. Phys.* **1993**, *98*, 5648–5652.
17. Lee, C.; Yang, W.; Parr, R. G. *Phys. Rev. B: Condens. Matter Mater. Phys.* **1988**, *37*, 785–789.
18. Dunning, T. H., Jr. *J. Chem. Phys.* **1989**, *90*, 1007–1023.
19. Kendall, R. A.; and Dunning, T. H., Jr.; Harrison, R. J. *J. Chem. Phys.* **1992**, *96*, 6796–6806.
20. Peterson, K. A. Puzzarini, C. *Theor. Chem. Acc.* **2005**, *114*, 283–296.
21. Feller, D. *J. Comp. Chem.* **1996**, *17*, 1571–1586.
22. Schuchardt, K. L.; Didier, B. T.; Elsethagen, T.; Sun, L.; Gurumoorthi, V.; Chase, J.; Li, J.; Windus, T. L. *J. Chem. Inf. Model.* **2007**, *47*, 1045–1052.
23. Peng, C.; Ayala, P. Y.; Schlegel, H. B.; Frisch, M. J. *J. Comp. Chem.* **1996**, *17*, 49–56.
24. Reed, A. E.; Curtiss, L. A.; Weinhold, F. *Chem. Rev.* **1988**, *88*, 899–926.
25. Ohno, K.; Maeda, S. *Chem. Phys. Lett.* **2004**, *384*, 277–282.
26. Maeda, S.; Ohno, K. *J. Phys. Chem. A* **2005**, *109*, 5742–5753.
27. Ohno, K.; Maeda, S. *J. Phys. Chem. A* **2006**, *110*, 8933–8941.
28. Maeda, S.; Ohno, K. *J. Phys. Chem. A* **2007**, *111*, 4527–4534.
29. Schröder, D.; Brown, R.; Schwerdtfeger, P.; Wang, X. B.; Yang, X.; Wang, L. S.; Schwarz, H. *Angew. Chem., Int. Ed.* **2003**, *42*, 311–314.
30. Wang, Y. K.; Wang, X. B.; Xing, X. P.; Wei, F.; Li, J.; Wang, L. S. *J. Phys. Chem. A* **2010**, *114*, 11244–11251.
31. Peláez, R. J.; Blondel, C.; Delsart, C.; Drag, C. *J. Phys. B: At. Mol. Opt. Phys.* **2009**, *42*, 125001.
32. Huang, Z.; Yuan, Y.; Sun, L.; Wang, X.; Li, Y. *RSC Adv.* **2016**, *87*, 84016–84024.
33. Bilodeau, R. C.; Scheer, M.; Haugen, H. K. *J. Phys. B: At. Mol. Opt. Phys.* **1998**, *31*, 3885–3891.
34. Hotop, H.; Lineberger, W. C. *J. Phys. Chem. Ref. Data* **1985**, *14*, 731–750.
35. Cho, H. G.; Andrews, L. *Inorg. Chem.* **2011**, *50*, 10319–10327.
36. Liu, H. T.; Xiong, X. G.; Dau, P. D.; Wang, Y. L.; Huang, Y. L.; Li, J.; Wang, L. S. *Nat. Commun.* **2013**, *4*, 2223.
37. Martínez-Salvador, S.; Falvello, L. R.; Martín, A.; Menjón, B. *Chem. Sci.* **2015**, *6*, 5506–5510.
38. Baya, M.; Pérez-Bitrián, A.; Martínez-Salvador, S.; Casas, J. M.; Menjón, B.; Orduna, J. *Chem. Eur.* **2017**, *23*, 1512–1515.

# Chapter 4.

# Reaction of $CH_3I$ with Au in solid neon matrix

A major part of this chapter has been published in the following paper.

Muramatsu, S.; Wu, X.; Chen, M.; Zhou, M.; Tsukuda, T.
*J. Phys. Chem. A* **2017**, *121*, 8408–8413.

## 4.1. Introduction

In Chapter 2, I demonstrated that $Au^-$ reacts with $CH_3I$ in the gas phase to form a gold-inserted anionic species $[CH_3–Au–I]^-$. I further proposed based on mass spectrometry and theoretical calculations that $[CH_3–Au–I]^-$ anion reacts with another $CH_3I$ to produce $C_2H_6$ via the C–C bond formation on a reaction intermediate $[(CH_3)_2–Au–I_2]^-$. It suggests that $Au^-$ can mediate homocoupling reactions of organohalide molecules. However, effects of charge state of Au and solvents (or third body) on homocoupling reactions have not been addressed because of the limitation of our experimental method based on mass spectrometry. Furthermore, neither the intermediate $[(CH_3)_2–Au–I_2]^-$ nor final coupling product $C_2H_6$ were directly detected in that study.

Matrix-isolation,[1] a well-developed technique to trap reaction intermediates for the spectroscopic measurements is a powerful tool to study reactions of metal atoms/ions and organic molecules. Especially an advantage of this technique is that we can trigger the reactions in the matrix by external stimuli such as heat and light.[2] For example, previous studies on Au atoms isolated in solid equimolar mixture of CO and $O_2$ at 10 K forms an Au(II) complex $OCAuO_2CO$, which was converted to $CO_2$ (eq. 4.1) by raising temperature to 30–40 K[3] and UV light irradiation.[4]

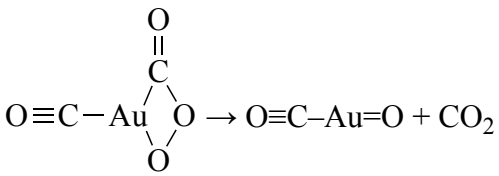


(4.1)

With regard to carbon–halogen bond activation, it has been intensively studied and

revealed by infrared (IR) spectroscopy that [$CH_3$–M–X] is formed in the reaction of various metal atoms (e. g., M = Ni, Pd, Pt, Cu, Ag and Au) and $CH_3X$ (X = F, Cl or Br).[5–7] The [$CH_3$–M–X] product corresponds to an oxidative addition product formed as a reaction intermediate in a conventional catalytic cycle of the C–C bond formation. However, chemical properties of [$CH_3$–M–X] toward subsequent reactions have been scarcely studied. Few examples include isomerization to methylidene ($CH_2$=MHX) and methylidyne (CH≡$MH_2X$)[6,7] and dissociation into small fragments such as $CH_2$–M–X, M–$CH_2X$, $CH_2X$–M and CX–MH.[5,6] To the best of our knowledge, there is no report on utilization of [$CH_3$–M–X] for the C–C bond formation in matrix-isolation studies.

In this chapter, I investigated the possibility of homocoupling reactions of $CH_3I$ on atomic Au in solid neon matrix. IR spectroscopy and density functional theory (DFT) calculations revealed that unprecedented product [$(CH_3)_2$–Au–$I_2$] was formed in addition to [$CH_3$–Au–I]. I found that visible light irradiation of [$(CH_3)_2$–Au–$I_2$] produced $C_2H_6$. These results demonstrate that Au atoms can mediate $C_2H_6$ production through electronically excited states formed by the irradiation with visible light.

## 4.2. Methods

### 4.2.1. Experiment

Figure 4.1 shows the schematic diagram of the apparatus used in this study for matrix-isolation IR spectroscopy.[8,9] Au atoms were generated by irradiating with the focused fundamental output of a Nd:YAG laser (Continuum, Minilite II) with typical pulse energy of 10–20 mJ/pulse at 10 Hz repetition onto a rotating gold target disk. The ablated Au atoms and $CH_3I$ (0.05%)/Ne gas mixture supplied at a rate of ~6 mmol/h were co-deposited for 30 min onto a CsI substrate kept at ~4 K by a closed-cycle helium

refrigerator. The $CH_3I$ liquid was purified by freeze-pump-thaw cycles prior to the experiment. After the sample preparation, the CsI substrate was rotated by 90º and Fourier transform infrared (FT-IR) absorption spectra of the products formed during the deposition were measured in the range of 4000–450 $cm^{-1}$ at a resolution of 0.5 $cm^{-1}$ (Bruker, VERTEX 80 V) using a liquid nitrogen cooled HgCdTe (MCT) detector. After the spectrum of the initial reaction products was recorded, the samples were annealed

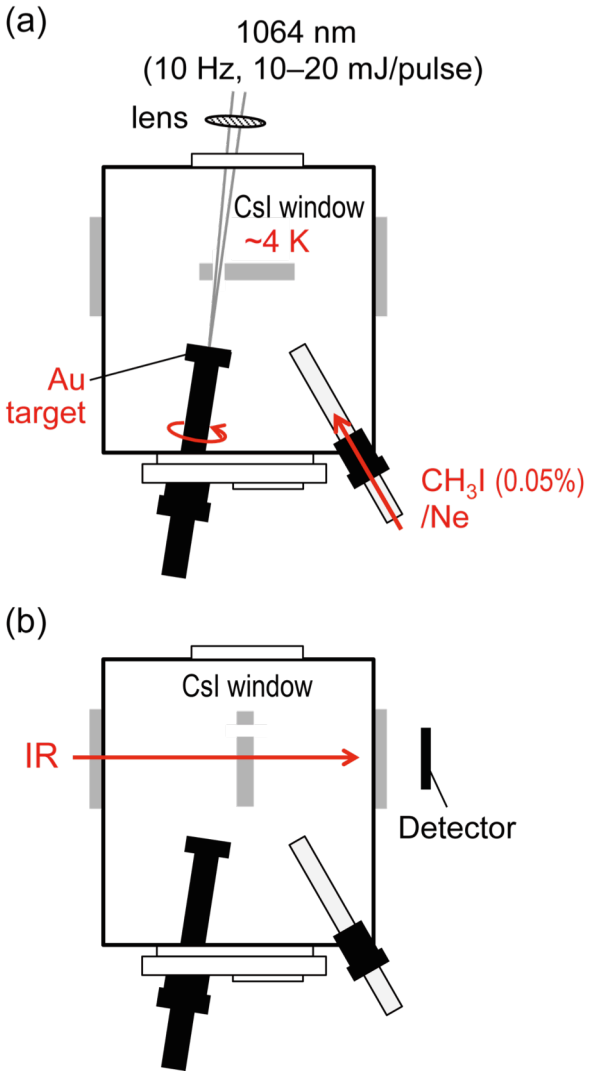


**Figure 4.1.** Experimental setup for (a) sample preparation and (b) IR spectroscopy.[9]

up to 11 K in order to promote diffusion-induced reactions of the trapped molecules. Then, the samples were irradiated with broadband visible light (wavelength > 400 nm) from a high-pressure Hg lamp (~160 W) fitted with a glass filter to promote further reactions and/or dissociations. The same procedure was repeated using deuterated methyl iodide ($CD_3I$) to facilitate the spectral assignments.

### 4.2.2. Computation

Electronic and geometrical structures of the detected species were studied by DFT calculations with the B3LYP[10,11] functional using the Gaussian 09 program.[12] The basis sets used were cc-pVTZ,[13] especially with pseudopotentials for Au and I atoms (cc-pVTZ-PP,[14] from the EMSL Basis Set Exchange Database[15,16]). Structural optimization[17] was carried out followed by harmonic frequency calculations to confirm that the optimized structures were located at local minima (LM) on the potential energy surface. Anharmonic terms (semi-diagonal quartic force field obtained by a perturbative approach[18]) were taken into account in the calculations of vibrational frequencies. Atomic charges were evaluated by natural population analysis based on natural bond orbitals (NBOs).[19]

To gain insights into the reaction mechanisms and estimate the activation barriers, I explored transition-state structures (TSs) using the Gaussian 09[12] and GRRM14[20–23] programs. The GRRM program enabled us to obtain TSs without any intuition, by starting the calculation from the LM structures by means of the anharmonic downward distortion following (ADDF) method. Intrinsic reaction coordinates (IRCs) were calculated to confirm that the obtained TSs connect the appropriate LM structures. All energies shown are corrected by harmonic vibrational zero-point energies (ZPE).

## 4.3. Results and discussion

### 4.3.1. Formation of oxidative addition product [$CH_3$–Au–I]

#### 4.3.1.1. Assignment of infrared spectra

Figure 4.2(a) shows a typical IR spectrum of the initial reaction products in the region of 1550–550 $cm^{-1}$. The four peaks at 1438.6, 1411.6, 1252.0 and 886.1 $cm^{-1}$ are assigned to degenerated (d)-$CH_3$ deformation, a combination of C–I stretching and d-$CH_3$ rocking, symmetric $CH_3$ deformation and d-$CH_3$ rocking vibrational modes of $CH_3I$, respectively, based on previous studies.[24–26] Figures 4.2(b) and (c) show the IR spectra recorded after annealing up to 11 K and irradiating with broadband light (> ~400 nm), respectively. Intensities of the two peaks at 1086.1 $cm^{-1}$ (labeled as **a**) and 641.9 $cm^{-1}$ (labeled as **a'**) are not affected by annealing, but are slightly enhanced by

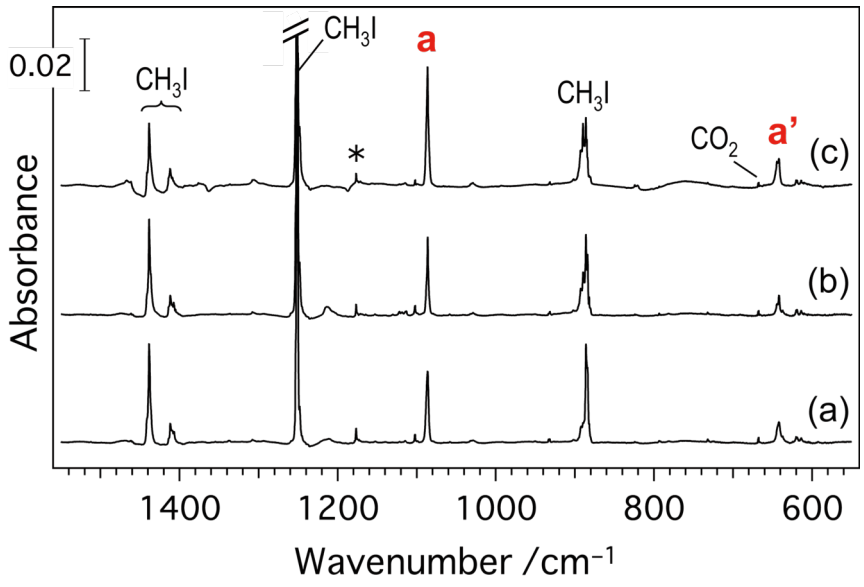


**Figure 4.2.** IR spectra in the region of 1550–550 $cm^{-1}$ recorded (a) after co-deposition of laser-ablated Au and $CH_3I$ in solid Ne at ~4 K for 30 min, (b) after subsequent annealing at 11 K, and (c) after irradiating a photolysis light (> 400 nm) for 15 min. The small peak with an asterisk is due to an impurity present in $CH_3I$ or Ne.

photolysis while retaining their relative intensities. This behavior indicates that the two peaks are derived from the same species. The experiments were repeated using the deuterated methyl iodide ($CD_3I$): peaks **a** and **a'** were red-shifted to 841.9 $cm^{-1}$ (labeled as **α**) and 464.2 $cm^{-1}$ (labeled as **α'**) (Figure 4.3). In the beginning, $[CH_3–Au–I]^-$ was considered to be the candidate for the assignment of peaks **a** and **a'**. Their vibrational frequencies listed in Table 4.1 do not agree with the experimental results. This result suggests that $Au^-$ produced by the laser ablation was not involved in the reactions because of its short lifetime in the $CH_3I$/Ne matrix as in the case of the reaction of Au in $CH_3F$/Ar.[5] Alternatively, previous reports on the formation of $[CH_3–Au–X]$ (X = F, Cl and Br) in the reaction of neutral Au with $CH_3X$ in solid Ar[5,6] suggest that the peaks **a** and **a'** can be assigned to $[CH_3–Au–I]$. Figure 4.4(a) shows the optimized structure of

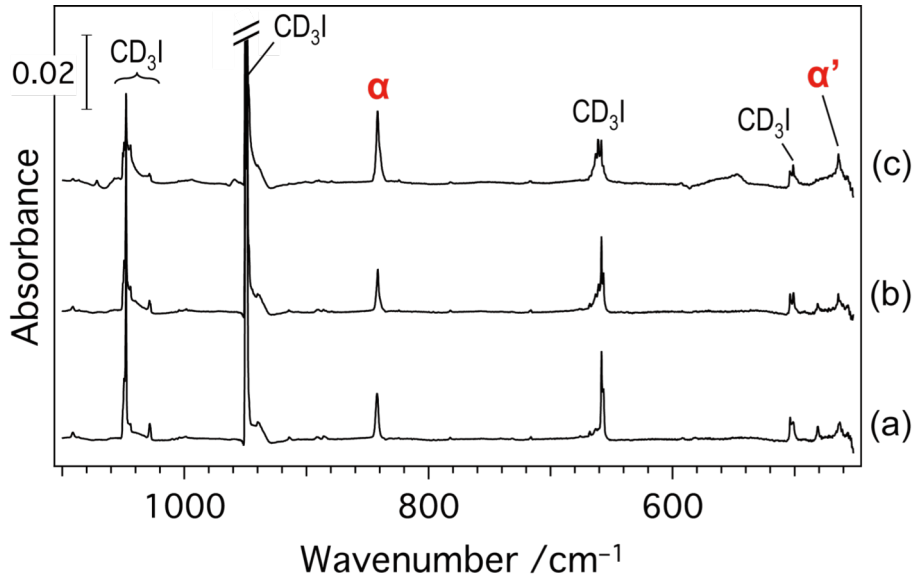


**Figure 4.3.** IR spectra in the region of 1100–450 $cm^{-1}$ recorded after co-deposition of laser-ablated Au and $CD_3I$ in solid Ne at ~4 K. (a) After 30 min of sample deposition, (b) after 11 K annealing, (c) after 15 min of photolysis by light with a wavelength of >400 nm. Assignment of $CD_3I$ is based on ref. 24.

**Table 4.1. Calculated Anharmonic Vibrational Frequencies of Infrared Active Normal Modes of $[CX_3–Au–I]^-$ (X = H or D).**

| Frequencies theoretically calculated /$cm^{-1}$ | | | |
|---|---|---|---|
| Species (symmetry) | Vibrational mode[a] | X = H | X = D |
| $[CX_3–Au–I]^-$ ($C_{3v}$) | d-C–H stretch | 2894.7 (0.76)[b] | 2167.8 (0.77) |
| | s-C–H stretch | 2885.5 (1.0) | 2026.4 (1.0) |
| | s-$CH_3$ deform | 1152.5 (0.14) | 891.0 (0.05) |
| | d-$CH_3$ rock | 718.5 (0.15) | 544.6 (0.20) |

[a] s: symmetric mode ($A_1$ symmetry), d: degenerated mode (E symmetry). [b] Relative IR intensity compared to the most intense peak.

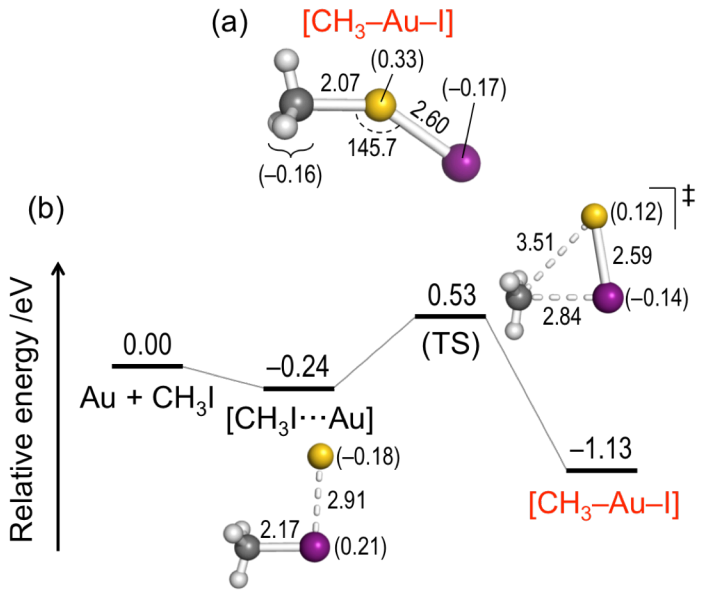


**Figure 4.4.** (a) Optimized structures of $[CH_3–Au–I]$ and (b) calculated energy profile along ground-state reaction pathway to form $[CH_3–Au–I]$ from Au + $CH_3I$. In the optimized structure, bond lengths and angles are shown in units of Å and degrees, respectively. Numbers in parentheses indicate the NBO charges of Au, I, and $CH_3$. In the energy profile, energies are shown with respect to the reactants, Au + $CH_3I$. Gray solid lines represent IRC. Color codes: yellow = Au, purple = I, gray = C, white = H.

[$CH_3$–Au–I], which is similar to that reported previously.[27] Au atom is inserted in the C–I bond of $CH_3I$ as in the case of [$CH_3$–Au–I]$^-$ (Chapters 2 and 3), but the C–Au–I backbone is bent in contrast to the case of [$CH_3$–Au–I]$^-$. One of the reasons for the bending is attributed to the strong σ bonding interaction between Au 5d and I 5p orbitals as shown in a Walsh diagram of [$CH_3$–Au–I] in Figure 4.5. Table 4.2 compares the observed peak positions and vibrational frequencies calculated for [$CH_3$–Au–I]. The frequencies for peaks **a**, **a**$'$, **α**, and **α**$'$ agree semi-qualitatively with those calculated for [$CH_3$–Au–I] and [$CD_3$–Au–I]. The frequency of peak **a** (1086.1 cm$^{-1}$) is comparable to the frequencies of the $CH_3$ deformation modes of [$CH_3$–Au–X] in solid Ar: 1196.5, 1083.5 and 1087.5 cm$^{-1}$ for X = F, Cl, and Br, respectively.[5,6] Close inspection of the expanded IR spectra in Figure 4.6 reveals a small peak at 732.1 cm$^{-1}$ (**a**$''$), which might be assigned to the $CH_3$ rocking mode of [$CH_3$–Au–I] (Table 4.2) although the enhancement of the peak intensity by photolysis was not clearly observed due to the weak intensity and the serious background noise.

#### 4.3.1.2. Reaction mechanism

The formation of [$CH_3$–Au–I] can be viewed as the oxidative addition of $CH_3I$ to Au because the NBO charge on the Au atom in [$CH_3$–Au–I] is increased from 0 to 0.33|e| (Figure 4.4(a)). In Chapter 2, I discussed that $CH_3I$ undergoes the oxidative addition to $Au^-$ in the gas phase via a barrierless mechanism, $S_N2$ attack on $Au^-$, followed by $I^-$ migration to form [$CH_3$–Au–I]$^-$ as shown in eq. 4.2.

$$Au^- + CH_3I \rightarrow [AuCH_3\cdots I^-] \rightarrow [CH_3\text{–}Au\text{–}I]^- \qquad (4.2)$$

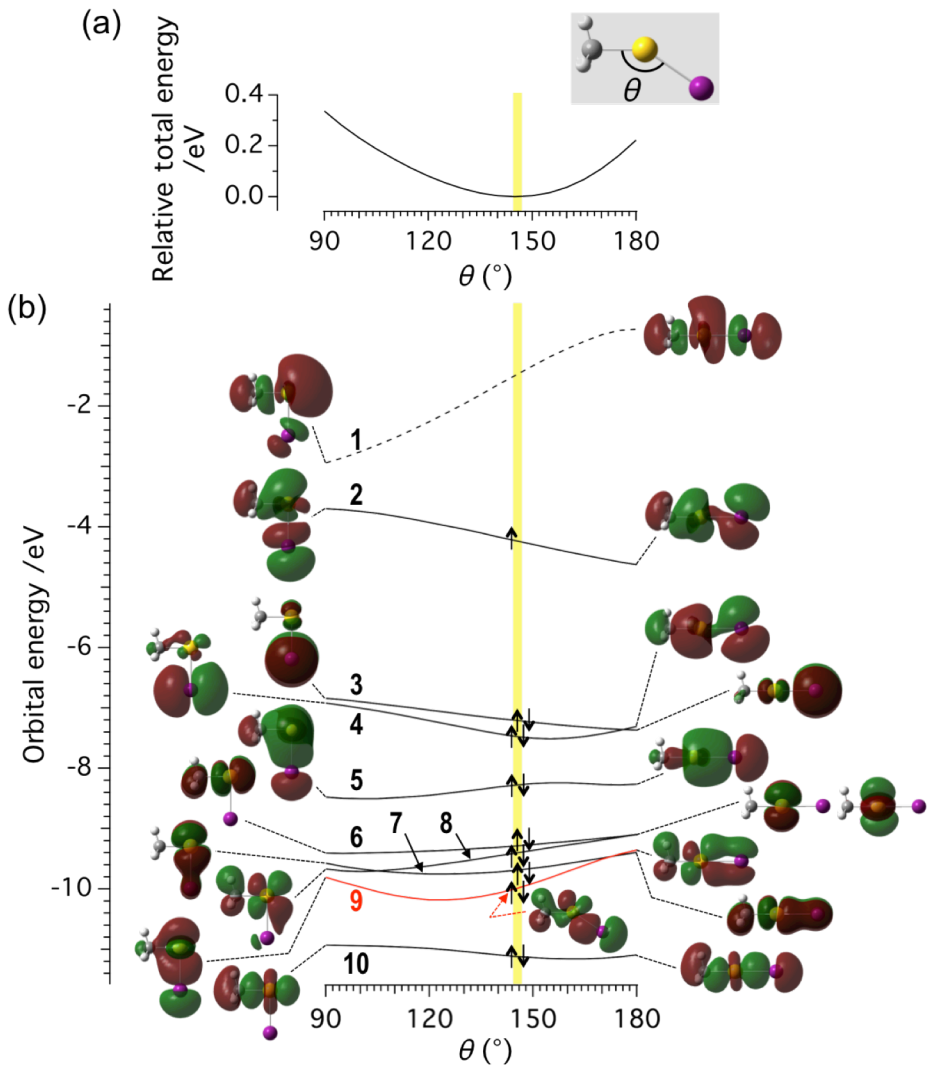


**Figure 4.5.** (a) Total electronic energy of [$CH_3$–Au–I] as a function of C-Au-I angle ($\theta$ (°)) calculated at the level of restricted open-shell B3LYP/LanL2dz (Au, I), 6-31G (C, H). Energies are with respect to the optimized structure ($\theta$ = 145.1°) indicated by a yellow line. (b) $\theta$-dependence of each orbital energy (Walsh diagram). Orbitals **1**: unoccupied, **2**: singly occupied, **3–10**: fully occupied. Stabilization of orbital **2** at $\theta$ = 180° explains the linear structure of [$CH_3$–Au–I]$^-$ anion, since it accommodates the excess electron. For [$CH_3$–Au–I], instead, the stability of orbitals **4**, **6**, **7**, **8** and **9** dominates the geometric structure. Especially in orbital **9** (colored in red), the bonding scheme differs with the $\theta$ angle: Au 5d and I 5p atomic orbitals make the σ bond at $\theta \sim 145°$ (inset) and the π bond at $\theta = 180°$, resulting in particularly large stability in the bent structure.

**Table 4.2. Experimental IR Peak Positions Observed After the Reaction of Au + $CX_3I$ (X = H or D) in Solid Ne, and Calculated Anharmonic Vibrational Frequencies of Selected Normal Modes.**

| Frequencies experimentally observed /$cm^{-1}$ | | | Frequencies theoretically calculated /$cm^{-1}$ [a] | | |
|---|---|---|---|---|---|
| X = H[b] | X = D[c] | Species (symmetry) | Assignment | X = H | X = D |
| 1086.1 (s)[d], **a** | 841.9 (s), **α** | | $CH_3$ deform | 1100.3 (1.0)[e] | 841.7 (1.0) |
| 732.1 (w), **a”** | – | $[CX_3–Au–I]$ ($C_s$) | A” $CH_3$ rock | 701.3 (0.06) | 516.6 (0.06) |
| 641.9 (m), **a’** | 464.2 (m), **α’** | | A’ $CH_3$ rock | 656.0 (0.24) | 496.8 (0.15) |
| 2962.9 (m), **b”** | 2128.4 (m), **β”** | | sym C–H stretch | 2947.5 (0.41) | 2140.5 (0.54) |
| 1213.8 (s), **b** | 914.4 (m), **β** | $[(CX_3)_2–Au–I_2]$ ($C_s$) | $CH_3$ deform | 1224.2 (1.0) | 926.6 (1.0) |
| 780.9 (w), **b’** | – | | A’ $CH_3$ rock | 819.1 (0.18) | 612.3 (0.25) |
| 2887.5 (s), **c** | 2233.4 (s), **γ** | | $A_{2u}$ sym C–H stretch | (2879.9 (1.0)) | (2236.5 (1.0)) |
| 1467.2 (m), **c’** | 1071.8 (m), **γ’** | $C_2X_6$ ($D_{3d}$) | $E_u$ $CH_3$ deform | (1467.1 (0.26)) | (1070.9 (0.30)) |
| 820.7 (m), **c”** | 593.9 (w), **γ”** | | $E_u$ $CH_3$ rock | (824.2 (0.12)) | (595.9 (0.11)) |

[a] Calculations on $C_2X_6$ were conducted for reference. Assignments are based on the reported experimental values.[24] [b] See Figures 4.2 and 4.6. [c] See Figures 4.3 and 4.7. [d] Peak intensity. s: strong, m: medium, w: weak. [e] Relative IR intensity compared to the most intense peak.

On the other hand, calculation on the energy profile along the IRCs revealed that the formation of [$CH_3$–Au–I] from Au($^2S_{1/2}$) in the ground state and $CH_3I$ is highly exothermic (1.13 eV) and proceeds via direct insertion of the Au atom into the C–I bond (Figure 4.4(b)). However, this reaction may be hindered due to a high activation barrier (0.53 eV, Figure 4.4(b)). This inference is supported by the fact that the intensities of peaks **a** and **a'** did not increase by annealing at 11 K (Figures 4.2(a) and (b)). It is plausible that an electronically excited Au atom ($Au^*$) formed in the laser ablation was involved in the formation of [$CH_3$–Au–I] as represented in eq. 4.3. Previous reports proposed that Au($^2P_{1/2}$), higher in energy than Au($^2S_{1/2}$) in the ground state by 4.6 eV,[28] was inserted into the C–X bond of $CH_3X$ (X = H or F) in solid Ar.[5,29] I suggest here another possibility that Au($^2D_{5/2}$) and Au($^2D_{3/2}$), higher in energy than Au($^2S_{1/2}$) by 1.1 and 2.7 eV,[28] are involved in the reaction because it has a longer radiative lifetime (~ms)[30] than Au($^2P_{1/2}$). The excess energy associated with eq. 4.3 is considered to be dissipated into the surrounding Ne matrix.

$$Au^* + CH_3I \rightarrow [CH_3–Au–I]^* \rightarrow [CH_3–Au–I] \qquad (4.3)$$

### 4.3.2. Photoassisted homocoupling of $CH_3I$

#### 4.3.2.1. Formation of [$(CH_3)_2$–Au–$I_2$]

Figures 4.6 and 4.7 show the IR spectra after the reactions of Au + $CH_3I$ (in the region of 3000–2700 and 1550–550 $cm^{-1}$) and Au + $CD_3I$ (in the region of 2280–2100 and 1150–490 $cm^{-1}$), respectively. The most prominent feature in Figure 4.6 is a strong peak at 1213.8 $cm^{-1}$, labeled as **b**. This peak disappears after the photolysis (Figure 4.6(c)). Small peaks at 2962.6 (**b"**) and 780.9 $cm^{-1}$ (**b'**) exhibit similar behavior upon

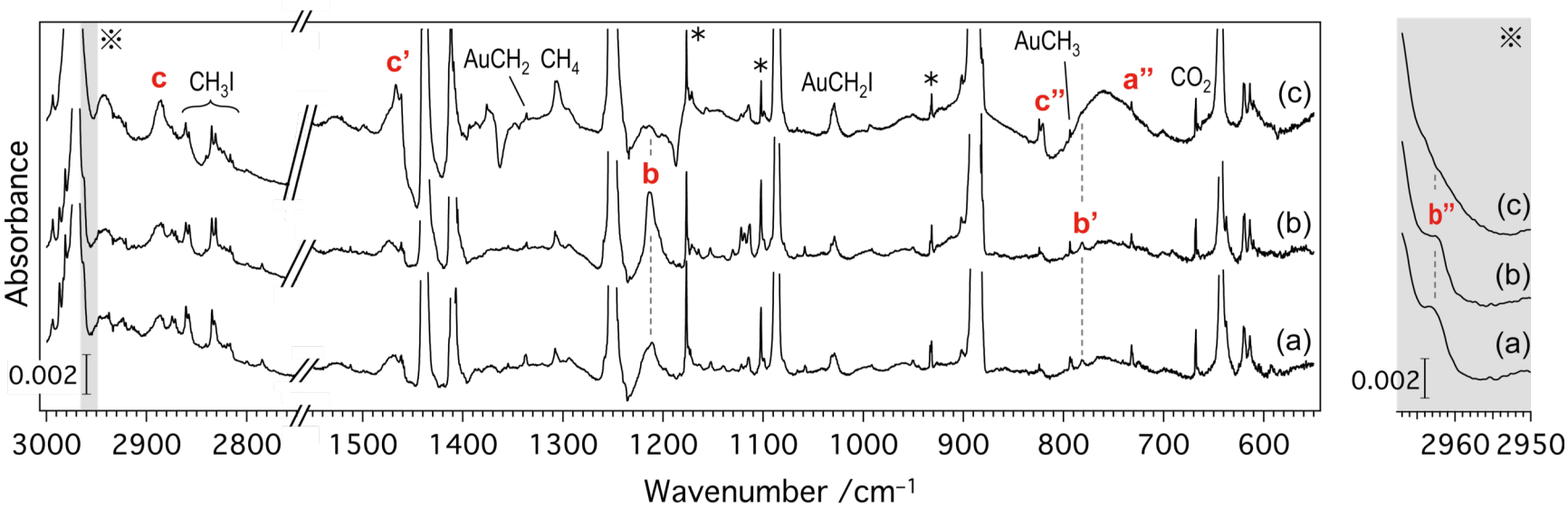


**Figure 4.6.** IR spectra in the regions of 3000–2700 and 1550–550 $cm^{-1}$ recorded (a) after co-deposition of laser-ablated Au and $CH_3I$ in solid Ne at ~4 K for 30 min, (b) after 11 K annealing, (c) after 15 min of photolysis by light with a wavelength of > 400 nm. An expanded view of the region 2967–2950 $cm^{-1}$ is shown separately, colored in gray.

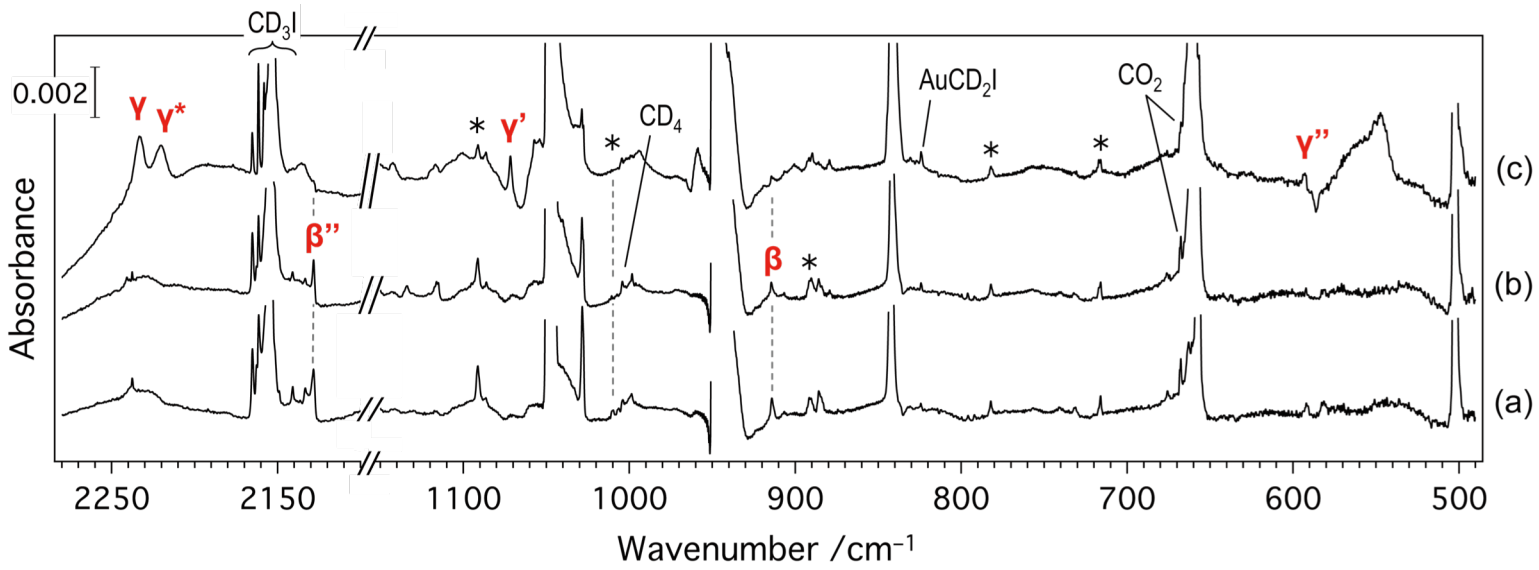


**Figure 4.7.** IR spectra in the region of 2280–2100 and 1150–490 $cm^{-1}$ recorded after co-deposition of laser-ablated Au and $CD_3I$ in solid Ne at ~4 K. (a) After 30 min of sample deposition, (b) after 11 K annealing, (c) after 15 min of photolysis by light with a wavelength of > 400 nm. Peak assignments are shown in Table 1. Peak γ* (not shown in Table 4.2) is assigned to $C_2D_6$ following to ref. 24, although an assigned vibrational mode was not given in the paper.

photolysis. I hypothesized that these peaks are assigned to a reaction product of [$CH_3$–Au–I] and $CH_3I$ based on our previous theoretical prediction of the formation of [$(CH_3)_2$–Au–$I_2$]$^-$ via the oxidative addition of $CH_3I$ onto [$CH_3$–Au–I]$^-$ (Chapter 2). Figure 4.8(a) shows the optimized structure of [$(CH_3)_2$–Au–$I_2$]. The Au atom is bonded by two $CH_3$ groups and two I atoms in a planar configuration. [$(CH_3)_2$–Au–$I_2$] can be viewed as a product of the oxidative addition of two $CH_3I$ molecules to Au because the net charge on the Au atom is increased from 0 to 0.30|e| (Figure 4.8(a)). Table 4.2 lists

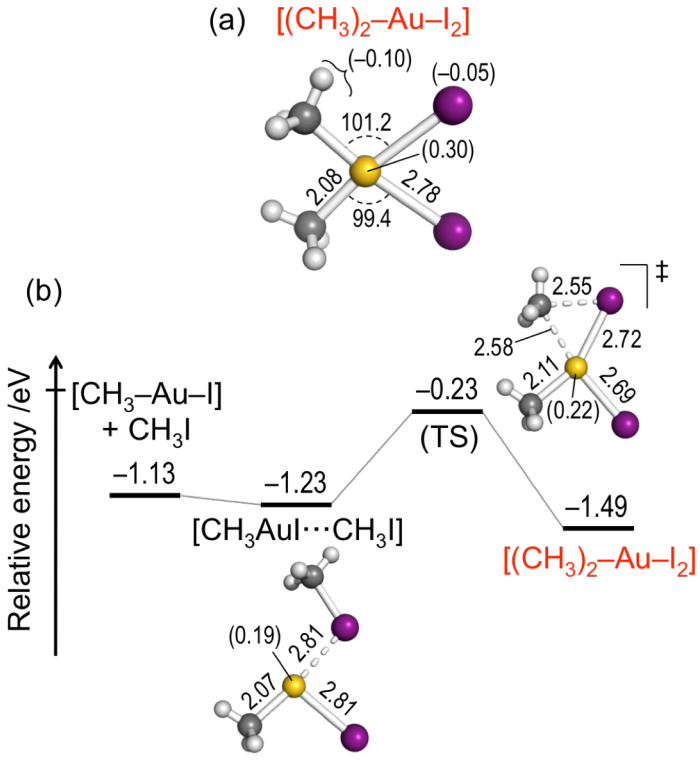


**Figure 4.8.** (a) Optimized structure of [$(CH_3)_2$–Au–$I_2$] and (b) calculated energy profile along ground-state reaction pathway to form [$(CH_3)_2$–Au–$I_2$] from [$CH_3$–Au–I] and $CH_3I$. In the optimized structure, bond lengths and angles are shown in units of Å and degrees, respectively. Numbers in parentheses indicate the NBO charges of Au, I, and $CH_3$. In the energy profile, energies are shown with respect to the initial reactants, Au + 2$CH_3I$. Gray solid lines represent IRCs. Color codes: yellow = Au, purple = I, gray = C, white = H.

the calculated vibrational frequencies of [$(CH_3)_2$–Au–$I_2$]. Quantitative comparison led us to conclude that peaks **b**–**b**" are assigned to [$(CH_3)_2$–Au–$I_2$]. Three peaks **β**–**β**" observed in Figure 4.7 can be assigned to [$(CD_3)_2$–Au–$I_2$] (Table 4.2). Similar compounds consisting of titanium atom (Ti) and $CH_3X$ (X = F, Cl, Br and I), [$(CH_3)_2$–Ti–$X_2$], have been reported.[7,31,32]

Figure 4.8(b) shows a calculated energy profile along the reaction pathway to generate [$(CH_3)_2$–Au–$I_2$] from [$CH_3$–Au–I] and $CH_3I$ in their electronic ground state. Energies are shown with respect to that of Au + $2CH_3I$. It was found that conversion of the complex [$CH_3AuI\cdots CH_3I$] to [$(CH_3)_2$–Au–$I_2$] is an elementary process with a single TS. The activation barrier is as high as 1.00 eV. This calculation result indicates that the formation of [$(CH_3)_2$–Au–$I_2$] does not involve [$CH_3$–Au–I] in the electronically ground state, but rather [$CH_3$–Au–I] and/or Au in the electronically excited state shown in eq. 4.3.

#### 4.3.2.2. Photoassisted elimination of $C_2H_6$ from [$(CH_3)_2$–Au–$I_2$]

Although [$(CH_3)_2$–Au–$I_2$] observed in Figure 4.6 corresponds to an intermediate for homocoupling reactions, the coupling product $C_2H_6$ was not detected in the IR spectra in Figures 4.6(a) and (b). Figure 4.9 shows a calculated energy profile along the reaction pathway for the generation of $C_2H_6$ from [$(CH_3)_2$–Au–$I_2$] in their electronic ground state. Dissociation of [$(CH_3)_2$–Au–$I_2$] into $C_2H_6$ and $AuI_2$ is calculated to be exothermic (1.27 eV) and an elementary reaction via a single TS. At the TS, two Au–C bonds of [$(CH_3)_2$–Au–$I_2$] are weakened concurrently to form a three-membered ring (Au $\cdots$C$\cdots$C). The activation barrier is as high as 1.22 eV. The theoretically predicted high barrier is consistent with the non-production of $C_2H_6$ even by annealing [$(CH_3)_2$–Au–$I_2$]

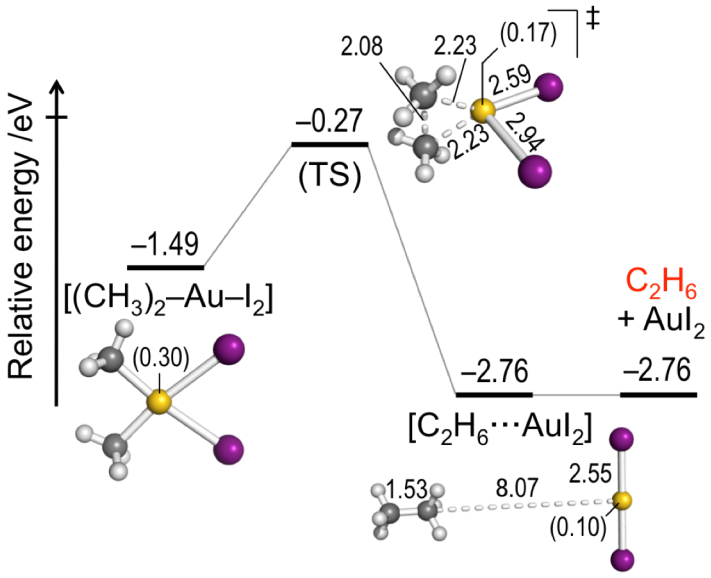


**Figure 4.9.** Calculated energy profile along ground-state reaction pathway for generation of $C_2H_6$ from $[(CH_3)_2–Au–I_2]$. Energies are shown with respect to that of Au + $2CH_3I$. Gray solid lines represent IRCs. Each optimized structure is shown with bond length in Å and NBO charge of Au atom (numbers with parentheses). Color codes: yellow = Au, purple = I, gray = C, white = H.

at 11 K.

After irradiation with visible light, new peaks assignable to $C_2H_6$ appeared at 2887.5 (peak **c**), 1467.2 (peak **c**'), and 820.7 $cm^{-1}$ (peak **c**")[24] in Figure 4.6(c). The emergence of peaks **c**, **c**', and **c**" is accompanied by the disappearance of peaks **b**, **b**', and **b**". This correlation indicates that $C_2H_6$ is produced by photoexcitation of $[(CH_3)_2–Au–I_2]$. A control experiment in the absence of Au atom (Figure 4.10) showed no indication of $C_2H_6$ formation, confirming that Au is indispensable for $C_2H_6$ production. The formation of the putative counterpart $AuI_2$ could not be confirmed in the present study because the vibrational frequencies of $AuI_2$ (< 450 $cm^{-1}$) are outside the range of our measurements. Although the details of the reaction mechanism in the electronically

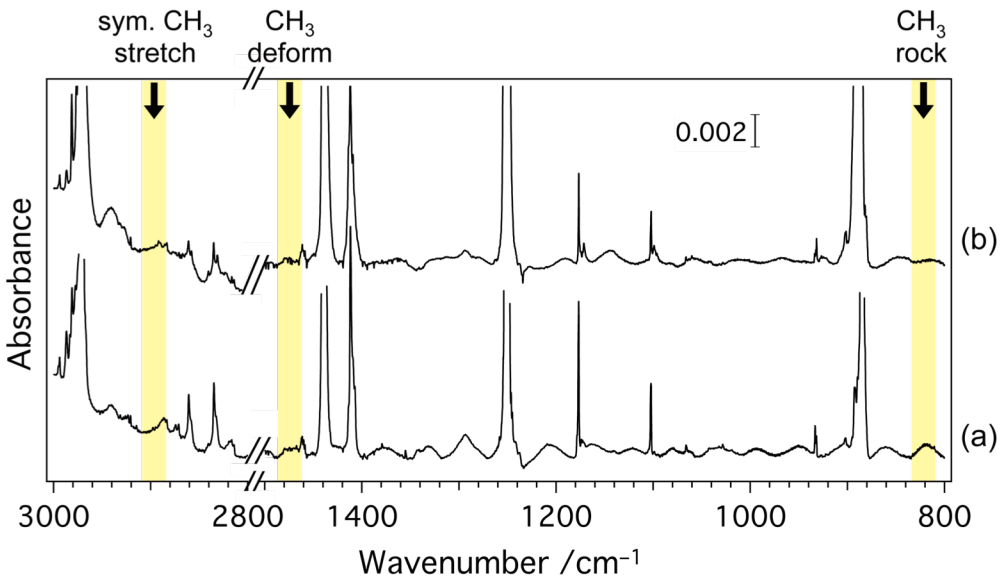


**Figure 4.10.** IR spectra in the region of 3000–2800 and 1500–800 $cm^{-1}$ recorded after deposition of $CH_3I$ in solid Ne at ~4 K without laser-ablated Au. (a) After 30 min of sample deposition, (b) after 15 min of photolysis by light with a wavelength of >400 nm. The expected peak positions of $C_2H_6$ (Table 4.2) are indicated by yellow lines.

excited state is beyond the scope of the present study, the elimination of $C_2H_6$ from $[(CH_3)_2–Au–I_2]$ may proceed via a nonadiabatic transition from an electronically excited state to the ground state near the TS as described in eq. 4.4.

$$[(CH_3)_2–Au–I_2] \xrightarrow{h\nu} [(CH_3)_2–Au–I_2]^* \rightarrow C_2H_6 + AuI_2 \qquad (4.4)$$

A slightly enhanced intensity of peaks **a** and **a'** after light irradiation (Figure 4.2(c)) suggests that the initial reactant $[CH_3–Au–I]$ is formed via eq. 4.5 by overcoming a barrier as high as 1.26 eV (Figure 4.8(b)).

$$[(CH_3)_2\text{–}Au\text{–}I_2] \xrightarrow{h\nu} [(CH_3)_2\text{–}Au\text{–}I_2]^* \rightarrow [CH_3\text{–}Au\text{–}I] + CH_3I \qquad (4.5)$$

In contrast, in Chapter 2, I proposed that $C_2H_6$ is produced via reductive elimination from $[(CH_3)_2\text{–}Au\text{–}I_2]^-$ generated by sequential oxidative addition of two $CH_3I$ molecules to $Au^-$, although the neutral product $C_2H_6$ was not detected by mass spectrometry. There are two possible reasons for spontaneous elimination of $C_2H_6$ from $[(CH_3)_2\text{–}Au\text{–}I_2]^-$: (1) TSs for the oxidative addition and reductive elimination are far below in energy with respect to the reactants $Au^- + 2CH_3I$; (2) there is not enough solvent (or third body) that stabilizes the reacting systems into intermediates.

### 4.3.3. Formation of other minor products

Finally, it is noteworthy that other peaks observed in Figure 4.6 were comparable to those reported in previous studies on the reactions of Au and $CH_3X$ (X = H, F, Cl, Br) in solid Ar.[5,29] For example, a peak at 1241.5 $cm^{-1}$ observed in the reaction of Au and $CH_3F$ in an Ar matrix was assigned to $AuCH_2F$.[5] The peaks in Figure 4.6 are

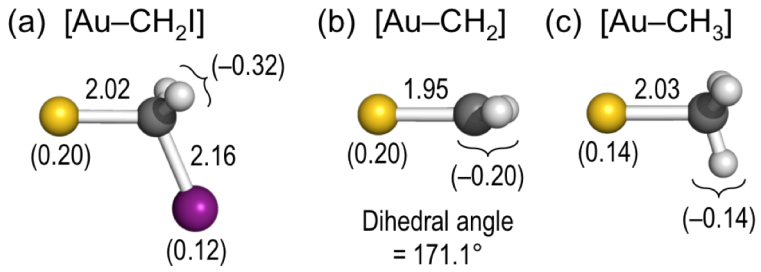


**Figure 4.11**. Optimized structures of (a) $[Au\text{–}CH_2I]$, (b) $[Au\text{–}CH_2]$, and (c) $[AuCH_3]$. Bond lengths are shown in units of Å. Numbers in parentheses indicate the NBO charges of Au, I, $CH_2$, and $CH_3$. Note that $[Au\text{–}CH_2]$ is not planar; the angle between two Au-C-H planes (dihedral angle) is 171.1°. Color codes: yellow = Au, purple = I, gray = C, white = H.

assigned to novel species [Au–$CH_2$I] and reported species [Au–$CH_2$] and [Au–$CH_3$], whose optimized structures are shown in Figure 4.11. The structure of [Au–$CH_2$I] does not correspond to a simple fragment of [$CH_3$–Au–I] (Figure 4.4(a)). The peak at 1028.9 $cm^{-1}$ was assigned to the $CH_2$ wagging mode of [Au–$CH_2$I] (calculated frequency: 1058.4 $cm^{-1}$). The peaks at 1336.3 and 793.5 $cm^{-1}$ were assigned to the $CH_2$ scissoring mode of [Au–$CH_2$] and the d-$CH_3$ rocking mode of [Au–$CH_3$], respectively, based on reported values in the Ar matrix[5,29] (calculated frequencies: 1290.4 and 788.3 $cm^{-1}$). Formations of [Au–$CH_2$I] and [Au–$CH_2$] indicate that the C–H bond is activated and cleaved in the reaction of $CH_3$I with Au.

## 4.4. Summary

I demonstrated by means of IR absorption spectroscopy and DFT calculations that the reaction of laser-ablated Au with $CH_3$I in a solid Ne matrix affords the oxidative addition product [$CH_3$–Au–I], similar to our previous study on $Au^-$ in the gas phase. I further characterized the product of Au and two $CH_3$I molecules, [$(CH_3)_2$–Au–$I_2$], which can be regarded as an intermediate for Au-mediated homocoupling of $CH_3$I molecules. It was clarified that visible light irradiation triggers the conversion of the intermediate to the coupling product $C_2H_6$. This study showed the potential of Au atoms to promote C–C coupling of haloalkanes and introduces the concept of the photoassisted C–C coupling reaction, which could be applied in designing novel gold catalysts.

## References


1. Whittle, E.; Dows, D. A.; Pimentel, G. C. *J. Chem. Phys.* **1954**, *22*, 1943.
2. Andrews, L.; Moskovits, M. *Chemistry and Physics of Matrix-Isolated Species*; Elsevier: North Holland, 1989.
3. Huber, H.; McIntosh, D.; Ozin, G. A. *Inorg. Chem.* **1977**, *16*, 975–979.
4. Xu, Q.; Jiang, L. *J. Phys. Chem. A* **2006**, *110*, 2655–2662.
5. Cho, H. G.; Andrews, L. *Inorg. Chem.* **2011**, *50*, 10319–10327.
6. Cho, H. G.; Andrews, L. *Organometallics* **2013**, *32*, 2753–2759.
7. Andrews, L; Cho, H. G. *Organometallics* **2006**, *25*, 4040–4053.
8. Wang, G. J.; Zhou, M. F. *Int. Rev. Phys. Chem.* **2008**, *27*, 1–25.
9. Andrews, L.; Citra, A. *Chem. Rev.* **2002**, *102*, 885–911.
10. Becke, A. D. *J. Chem. Phys.* **1993**, *98*, 5648–5652.
11. Lee, C.; Yang, W.; Parr, R. G. *Phys. Rev. B: Condens. Matter Mater. Phys.* **1988**, 37, 785–789.
12. Frisch, M. J.; Trucks, G. W.; Schlegel, H. B.; Scuseria, G. E.; Robb, M. A.; Cheeseman, J. R.; Scalmani, G.; Barone, V.; Mennucci, B.; Petersson, G. A.; Nakatsuji, H.; Caricato, M.; Li, X.; Hratchian, H. P.; Izmaylov, A. F.; Bloino, J.; Zheng, G.; Sonnenberg, J. L.; Hada, M.; Ehara, M.; Toyota, K.; Fukuda, R.; Hasegawa, J.; Ishida, M.; Nakajima, T.; Honda, Y.; Kitao, O.; Nakai, H.; Vreven, T.; Montgomery, J. A., Jr.; Peralta, J. E.; Ogliaro, F.; Bearpark, M.; Heyd, J. J.; Brothers, E.; Kudin, K. N.; Staroverov, V. N.; Kobayashi, R.; Normand, J.; Raghavachari, K.; Rendell, A.; Burant, J. C.; Iyengar, S. S.; Tomasi, J.; Cossi, M.; Rega, N.; Millam, J. M.; Klene, M.; Knox, J. E.; Cross, J. B.; Bakken, V.; Adamo, C.; Jaramillo, J.; Gomperts, R.; Stratmann, R. E.; Yazyev, O.; Austin, A. J.; Cammi, R.; Pomelli, C.; Ochterski, J. W.; Martin, R. L.; Morokuma, K.; Zakrzewski, V. G.; Voth, G. A.; Salvador, P.; Dannenberg, J. J.; Dapprich, S.; Daniels, A. D.; Farkas, Ö.; Foresman, J. B.; Ortiz, J. V.; Cioslowski, J.; Fox, D. J. Gaussian 09, Revision C.01/D.01, Gaussian, Inc., Wallingford CT, 2013.
13. Dunning, T. H., Jr. *J. Chem. Phys.* **1989**, *90*, 1007–1023.
14. Peterson, K. A. Puzzarini, C. *Theor. Chem. Acc.* **2005**, *114*, 283–296.
15. Feller, D. *J. Comput. Chem.* **1996**, *17*, 1571–1586.
16. Schuchardt, K. L.; Didier, B. T.; Elsethagen, T.; Sun, L.; Gurumoorthi, V.; Chase, J. Li, J. Windus, T. L. *J. Chem. Inf. Model.* **2007**, *47*, 1045–1052.
17. Peng, C.; Ayala, P. Y.; Schlegel, H. B.; Frisch, M. J. *J. Comp. Chem.* **1996**, *17*, 49–56.

18. Barone, V. *J. Chem. Phys.* **2005**, *122*, 14108.
19. Reed, A. E.; Curtiss, L. A.; Weinhold, F. *Chem. Rev.* **1988**, *88*, 899–926.
20. Ohno, K.; Maeda, S. *Chem. Phys. Lett.* **2004**, *384*, 277–282.
21. Maeda, S.; Ohno, K. *J. Phys. Chem. A* **2005**, *109*, 5742–5753.
22. Ohno, K.; Maeda, S. *J. Phys. Chem. A* **2006**, *110*, 8933–8941.
23. Maeda, S.; Ohno, K. *J. Phys. Chem. A* **2007**, *111*, 4527–4534.
24. Snelson, A. *J. Phys. Chem.* **1970**, *74*, 537–544.
25. Ito, F.; Nakagawa, T.; Futami, Y.; Kudoh, S.; Takayanagi, M.; Nakata, M. *Chem. Phys. Lett.* **2001**, *343*, 185–191.
26. Morino, Y.; Nakamura, J. *Bull. Chem. Soc. Jpn.* **1965**, *38*, 443–459.
27. Huang, Z.; Yuan, Y.; Sun, L.; Wang, X.; Li, Y. *RSC Adv.* **2016**, 87, 84016–84024.
28. Moore, C. E. *Atomic Energy Levels*; Circular of the US Nat'l. Bur. Stds. 467; U.S. National Bureau of Standards: Washington, DC, 1958.
29. Cho, H. G.; Andrews, L. *Dalton Trans.* **2011**, *40*, 11115–11124.
30. Schrittenlacher, W.; Kolb, D. M. *Ber. Bunsenges. Phys. Chem.* **1984**, *88*, 492–497.
31. McGrady, G. S.; Downs, A. J.; Bednall, N. C.; McKean, D. C.; Thiel, W.; Jonas, V.; Frenking, G.; Scherer, W. *J. Phys. Chem. A* **1997**, *101*, 1951–1968.
32. Lyon, J. T.; Andrews, L. *Inorg. Chem.*, **2005**, *44*, 8610–8616.

# Chapter 5.

# Reaction of $CH_3I$ with gold cluster anions, $Au_n^-$ ($n$ = 2–4)

第 5 章

本章については、5 年以内に雑誌等で刊行予定のため、非公開。

# Chapter 6.

# Concluding remarks

## 6.1. Summary of the thesis study

Aiming at gaining clues to rationally develop the highly active coinage metal-based catalysts for carbon–halogen bond activation, I focused on $CH_3I$ as the simplest organohalide and have explored the possibility of the C–I bond activation by coinage metal atoms and clusters. Throughout the studies on the following four research themes, I investigated experimentally and theoretically the effects on the activation of $CH_3I$ by the coinage metal atoms/clusters while changing the key factors such as element, charge state, and cluster size (Figure 6.1).

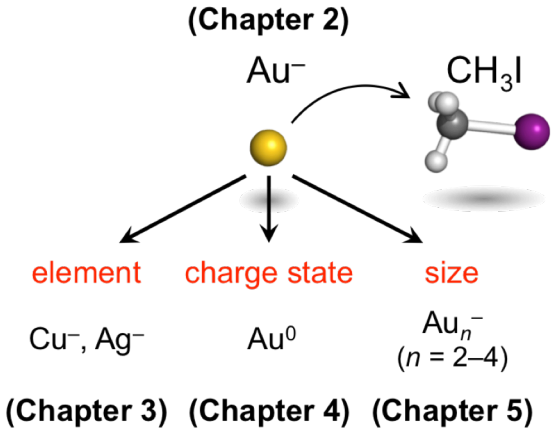


**Figure 6.1.** Summary of the current study.

In Chapter 2, I investigated the gas phase reaction of atomic $Au^-$ with $CH_3I$. Mass spectrometry on the reaction products revealed the formation of adduct compound $AuCH_3I^-$. Photoelectron spectroscopy and density functional theory (DFT) calculations clarified that, in $AuCH_3I^-$, Au atom is oxidatively inserted into the C–I bond in a linear configuration to form $[CH_3–Au–I]^-$. Theoretical studies indicated that oxidative addition proceeds in the successive two steps: nucleophilic attack of $Au^-$ toward $CH_3I$ in a $S_N2$

manner, followed by migration of the leaving $I^-$ to Au. This mechanism was supported by the formation of an ion-neutral complex, $[Au^-\cdots t\text{-}C_4H_9I]$, in the reaction of $Au^-$ with $t\text{-}C_4H_9I$ due to the activation barrier along the $S_N2$ pathway resulting from the steric hindrance. Finally, I theoretically proposed that the oxidative addition product $[CH_3–Au–I]^-$ further undergoes the consecutive oxidative addition of another $CH_3I$ followed by reductive elimination of $C_2H_6$, leaving $AuI_2^-$. These results suggest that $Au^-$ acts as a nucleophile to activate $C(sp^3)$–I bond of $CH_3I$ and induces the C–C coupling reaction of $CH_3I$.

In Chapter 3, I extended the scope of the reaction found in Chapter 2 to the other coinage metal anions, $Cu^-$ and $Ag^-$. Mass spectrometry, photoelectron spectroscopy, and DFT calculations revealed that the gas phase reactions of coinage metal anions $M^-$ (M = Cu, Ag, Au) with $CH_3I$ yields the common oxidative addition product $[CH_3–M–I]^-$ in highly exothermic pathway via $S_N2$ attack of $M^-$ on $CH_3I$ followed by $I^-$ migration. Based on the exothermicity associated with the formation process, I concluded that the thermodynamic stabilities of the products increase in the order of Au < Ag < Cu. Notably, their thermodynamic stabilities are significantly higher than that of typical Grignard reagent, $CH_3–Mg–I$. I attributed the high stability of the $[CH_3–M–I]^-$ to a strong bonding interaction between d orbitals of M atoms with 5p and σ/π orbitals of I and $CH_3$ ligands, respectively.

In Chapter 4, I examined the reaction of neutral Au atom with $CH_3I$ in low-temperature neon matrix. Infrared spectroscopy on the products and DFT calculations showed that novel Au complexes $[CH_3–Au–I]$ and $[(CH_3)_2–Au–I_2]$, in which one and two $CH_3I$ molecule(s), respectively, are oxidatively adsorbed on the neutral Au atom, were formed. Reaction pathway exploration calculations revealed that

the heights of the activation barriers for the sequential oxidative addition to produce [$CH_3$–Au–I] and [$(CH_3)_2$–Au–$I_2$] were 0.53 and 1.00 eV, respectively, suggesting that the reactions proceeded via electronically excited states. The reductive elimination of $C_2H_6$ from [$(CH_3)_2$–Au–$I_2$] leaving $AuI_2$ was hindered by an activation barrier as high as 1.22 eV, but was induced by visible light irradiation of [$(CH_3)_2$–Au–$I_2$]. These results suggest that photoassisted homocoupling of $CH_3I$ is mediated by Au atom, via [$(CH_3)_2$–Au–$I_2$] as an intermediate.

In Chapter 5, I studied the gas phase reaction of small $Au_n^-$ cluster anions ($n$ = 2–4) with $CH_3I$ to clarify the cluster size effect on the C–I bond activation. Mass spectrometry and pseudo-first order kinetic analyses clarified that $Au_2^-$ were most reactive among $Au_n^-$ clusters with the size of $n$ = 1–4. The $Au_2I^-$ was formed as the main product of the reaction of $Au_2^-$ and $CH_3I$, whereas the adduct compound $Au_2CH_3I^-$ was hardly formed, in sharp contrast to the reaction of $Au^-$ (Chapter 2). Calculations revealed that both of the oxidative addition pathway via $S_N2$ step to yield $[CH_3–Au_2–I]^-$ and the I abstraction pathway to form $Au_2I^-$ + $CH_3$ were exothermic and barrierless theoretically. I concluded that the reaction proceeded dominantly via I abstraction pathway that is highly preferential from the viewpoint of the steric factor. This study suggests that the branching ratio of the reaction can be controlled by the cluster size.

In conclusion, I demonstrated throughout Chapters 2–5 that Au atom and clusters, as well as other coinage metals, have high potentials to activate the C–I bond of $CH_3I$ via oxidative addition or I abstraction processes, and to promote the C–C homocoupling reaction between the $CH_3$ adsorbates to afford $C_2H_6$. It was revealed that the charge state and cluster size markedly affected the barrier heights for the activation and preferable mechanisms, which must be kept in mind in the practical development of

coinage-metal based catalysts in a future.

## 6.2. Future prospects

In Chapters 2–4, I focused on the C–I bond activation by atomic coinage metals. As described in Chapter 1, much attention has recently been paid to the single atom catalysts. For example, Au atoms on metal oxides have been used as catalysts for methanol steam reforming, water-gas shift, ethanol dehydrogenation, and CO oxidation.[1–4] In these Au atom catalysts, it has been considered that Au atoms have a cationic nature due to the electronic charge transfer to the metal oxide support. The cationic nature of the supported Au atoms is similar to the case of homogeneous Au(I) and Au(III) catalysts.[5] On the other hand, my thesis study revealed the anionic Au atoms can efficiently promote oxidative addition and homocoupling of $CH_3I$, which prompts us to develop new catalysts based on anionic Au atoms. Since Au has the largest electron affinity among the metal elements,[6] a few examples have reported the synthesis of anionic Au atom compounds under low-temperature and inert conditions.[7] In contrast, anionic Au clusters can be synthesized under ambient conditions by

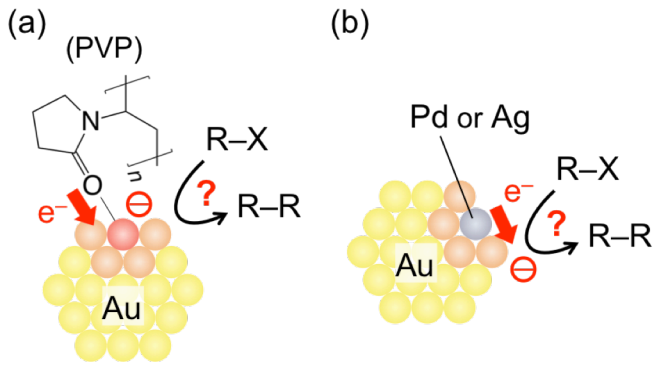


**Figure 6.2.** Negatively charged Au clusters by (a) stabilization with PVP and (b) doping hetero-metal atoms (e. g. Pd or Ag).

stabilizing them with electron-donating organic molecules such as polyvinylpyrrolidone (PVP)[8] or doping them with hetero-metal atoms such as Ag[9] and Pd.[10] These modulation of charge state of the Au clusters enhanced the catalytic performance for aerobic oxidations.[9,10] Thus, I expect that the catalytic applications of such negatively charged Au species for C–X bond activations are one of interesting future subjects (Figure 6.2).

Another future prospect includes further deepening of the basic understanding on chemical reactivity of coinage metal clusters in the framework of "superatom concept"[11] or originally "electronic shell model".[12] In this model, we consider that the valence electrons of the clusters are accommodated in discrete "superatomic orbitals": 1S, 1P, 1D, 2S, 1F, 2P, and so on, which resemble the conventional atoms (Figure 6.3). This model has long been used to explain the magic stability of the clusters; the clusters gain the exceptional stability when the superatomic orbital shells are closed at "magic numbers": $n_e$ = 2, 8, 20, 34 (or 40), 58, and so on ($n_e$: number of valence electrons). That is, the magic stability is explained in a similar manner to the high stability of conventional noble gas atoms.

There have been a few reports on application of the superatom concept to chemical reactivity of the clusters; we could predict the reactivity of the clusters based on a similarity to the corresponding

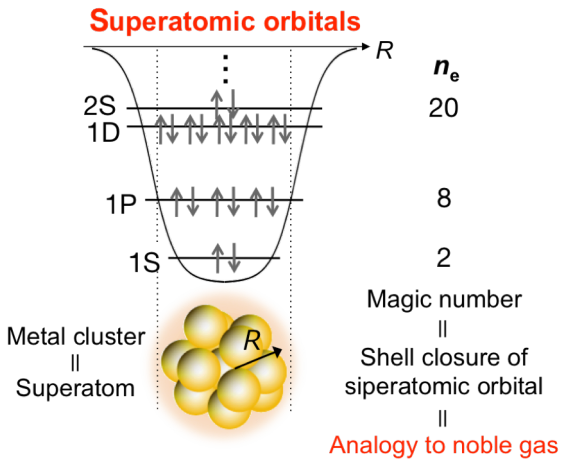


**Figure 6.3.** Schematic image of superatomic orbitals. $n_e$ represents the number of valence electrons of the superatom.

conventional atoms.[13] For example, it was proposed that superatomic alkali metals, $Cu_8^-$ and $Ag_8^-$ ($n_e$ = 9), may react with $Cl_2$ molecules in a harpooning mechanism,[14] a typical mechanism in a reaction of K atom toward $I_2$.[15]

The closed and open electronic configurations of $Au^-$ ($(1S)^2$) and $Au_2^-$ ($(1S)^2(1P)^1$) simply remind us of hydride ($H^-$) and alkali metal (e. g. Li). $H^-$ anion and Li atom are known to react with $CH_3X$ (X: halogen) in $S_N2$[16] and I abstraction[17] mechanisms, respectively, in consistent with the results for $Au^-$ and $Au_2^-$ (Chapters 2 and 5). Then, the question arises as to whether the superatom concept can predict the reactivity of coinage metal clusters with various sizes. To reveal the similarity and difference in chemistry of superatoms and conventional atoms, further study is required on the larger superatoms of coinage metals M (M = Cu, Ag, and Au): e. g. superatomic halides $M_7^-$ and $M_{19}^-$ and superatomic alkali metal $M_9$ and $M_{21}$. I expect such studies also will lead to discoveries of novel reactions completely unique to the clusters, which can never be explained by the similarity to the conventional atoms.

## References


1. Gu, X. K.; Qiao, B. T.; Huang, C. Q.; Ding, W. C.; Sun, K. J.; Zhan, E. S.; Zhang, T.; Liu, J. Y.; Li, W. X. *ACS Catal.* **2014**, *4*, 3886–3890.
2. Yang, M.; Li, S.; Wang, Y.; Herron, J. A.; Xu, Y.; Allard, L. F.; Lee, S.; Huang, J.; Mavrikakis, M.; Flytzani-Stephanopoulos, M. *Science* **2014**, *346*, 1498–1501.
3. Wang, C.; Garbarino, G.; Allard, L. F.; Wilson, F.; Busca, G.; Flytzani-Stephanopoulos, M. *ACS Catal.* **2016**, *6*, 210–218.
4. Qiao, B.; Liang, J. X.; Wang, A.; Xu, C. Q.; Li, J.; Zhang, T.; Liu, J. J. *Nano Res.* **2015**, *8*, 2913–2924.
5. Hashmi, A. S. K.; Hutchings, G. J. *Angew. Chem., Int. Ed.* **2006**, *45*, 7896–7936.
6. Rumble, J. R. (Ed.) *Handbook of Chemistry and Physics: 98th edition*, CRC Press: Boca Raton, 2017.
7. Jansen, M. *Chem. Soc. Rev.* **2008**, *37*, 1826–1835.
8. Tsunoyama, H.; Ichikuni, N.; Sakurai, H.; Tsukuda, T. *J. Am. Chem. Soc.* **2009**, *131*, 7086–7093.
9. Chaki, N. K.; Tsunoyama, H. Negishi, Y.; Sakurai, H.; Tsukuda, T. *J. Phys. Chem. C* **2007**, *111*, 4885–4888.
10. Xie, S.; Tsunoyama, H.; Kurashige, W.; Negishi, Y.; Tsukuda, T. *ACS Catal.* **2012**, *2*, 1519–1523.
11. Walter, M.; Akola, J.; Lopez-Acevedo, O.; Jadzinsky, P. D.; Calero, G.; Ackerson, C. J.; Whetten, R. L.; Grönbeck, H.; Häkkinen, H. *Proc. Natl. Acad, Sci. USA* **2008**, *105*, 9157–9162.
12. de Heer, W. A. *Rev. Mod. Phys*. **1993**, *65*, 611–676.
13. Luo, Z.; Castleman, A. W., Jr. *Acc. Chem. Res.* **2014**, *47*, 2931–2940.
14. Luo, Z. X.; Berkdemir, C.; Smith, J. C.; Castleman, A. W., Jr. *Chem. Phys. Lett.* **2013**, *582*, 24−30.
15. Gillen, K. T.; Rulis, A. M.; Bernstein, R. B. *J. Chem. Phys.* **1971**, *54*, 2831–2851.
16. Martinez, O., Jr.; Yang, Z.; Demarais, N. J.; Snow, T. P.; Bierbaum, V. M. *Astrophys. J.* **2010**, *720*, 173–177.
17. Sholeen, C. M.; Herm, R. R. *J. Chem. Phys.* **1976**, *65*, 5398–5407.

# List of Publications and Presentations

## Publications related to the thesis

(Chapter 2)

1. "Oxidative Addition of $CH_3I$ to $Au^-$ in the Gas Phase", Satoru Muramatsu, Kiichirou Koyasu and Tatsuya Tsukuda, *J. Phys. Chem. A* **2016**, *120*, 957–963.

(Chapter 3)

2. "Formation of Grignard Reagent-like Complex $[CH_3–M–I]^-$ via Oxidative Addition of $CH_3I$ on Coinage Metal Anions $M^-$ (M = Cu, Ag, Au) in the Gas Phase", Satoru Muramatsu, Kiichirou Koyasu and Tatsuya Tsukuda, *Chem. Lett.* **2017**, *46*, 676–679.

(Chapter 4)

3. "Photoassisted Homocoupling of Methyl Iodide Mediated by Atomic Gold in Low-Temperature Neon Matrix", Satoru Muramatsu, Xuan Wu, Mohua Chen, Mingfei Zhou and Tatsuya Tsukuda, *J. Phys. Chem. A* **2017**, *121*, 8408–8413.

## Publications not related to the thesis

1. "Suppressing Isomerization of Phosphine–Protected $Au_9$ Cluster by Bond Stiffening Induced by Single Pd Atom Substitution", Seiji Yamazoe, Shota Matsuo, Satoru Muramatsu, Shinjiro Takano, Kiyofumi Nitta and Tatsuya Tsukuda, *Inorg. Chem.* **2017**, *56*, 8319–8325.

2. "Anion Photoelectron Spectroscopy of Free $[Au_{25}(SC_{12}H_{25})_{18}]^-$", Keisuke Hirata, Keishiro Yamashita, Satoru Muramatsu, Shinjiro Takano, Keijiro Ohshimo, Toshiyuki Azuma, Ryuzo Nakanishi, Takashi Nagata, Seiji Yamazoe, Kiichirou Koyasu and Tatsuya Tsukuda, *Nanoscale* **2017**, *9*, 13409–13412.

**Oral presentations**

1. “Reaction of atomic gold anion to abstract halogen from halomethane”, Satoru Muramatsu, Kiichirou Koyasu, Tatsuya Tsukuda, 日本化学会第 95 春季年会, 日本大学, 2015 年 3 月.
2. “ハロアルカンの炭素–ハロゲン結合への金原子負イオンの挿入”, 村松悟, 小安喜一郎, 佃達哉, 第 9 回分子科学討論会, 東京工業大学, 2015 年 9 月.**（優秀講演賞）**
3. “Mechanism of oxidative addition of haloalkanes to atomic gold anion”, Satoru Muramatsu, Kiichirou Koyasu, Tatsuya Tsukuda, 日本化学会第 96 春季年会, 同志社大学, 2016 年 3 月.
4. “Oxidative addition of haloalkanes to coinage metal anions $M^-$ (M = Cu, Ag, Au) in the gas phase”, Satoru Muramatsu, Kiichirou Koyasu, Tatsuya Tsukuda, 日本化学会第 97 春季年会, 慶應義塾大学, 2017 年 3 月.**（学生講演賞）**
5. “低温希ガスマトリックス中における、金原子によるヨウ化メチルのホモカップリング反応”, 村松悟, Xuan Wu, Mohua Chen, Mingfei Zhou, 佃達哉, 第 11 回分子科学討論会, 東北大学, 2017 年 9 月.
6. “Oxidative Addition of Haloalkanes to Atomic Coinage Metal Anions $M^-$ (M = Cu, Ag, Au) in the Gas Phase”, Satoru Muramatsu, Kiichirou Koyasu, Tatsuya Tsukuda, The 8th International Conference on Theory of Atomic & Molecular Clusters (TAMC VIII), Beijing, China, September 2017.
7. “金原子 Au および金原子負イオン $Au^-$を用いたハロアルカンのホモカップリング反応”, 村松悟, Xuan Wu, Mohua Chen, 小安喜一郎, Mingfei Zhou, 佃達哉, IQCE 量子化学探索講演会 2017「量子化学で探る化学の最先端」, 学士会館, 2017 年 10 月.**（依頼講演）**

**Poster presentations**

1. “Insertion reaction of atomic gold anion into carbon–halogen bond of haloalkanes”, Satoru Muramatsu, Kiichirou Koyasu, Tatsuya Tsukuda, 第 31 回化学反応討論会, 北海道大学, 2015 年 6 月.
2. “Gas phase reaction of $Au^-$ and $Au_2^-$ toward $CH_3I$”, Satoru Muramatsu, Kiichirou Koyasu, Tatsuya Tsukuda, 第 32 回化学反応討論会, 大宮ソニックシティ, 2016 年 6 月.**（ベストポスター賞）**
3. “Oxidative Addition of Haloalkanes to Atomic Gold Anion in the Gas Phase”, Satoru Muramatsu, Kiichirou Koyasu, Tatsuya Tsukuda, International Symposium on Small Particles and Inorganic Clusters (ISSPIC) XVIII, Jyväskylä, Finland, August 2016.

# Acknowledgements

The present works were carried out at Department of Chemistry, Graduate School of Science, The University of Tokyo, under the supervision of Prof. Tatsuya Tsukuda.

First of all, I would like to express my deep gratitude to Prof. Tsukuda for his dedicated instructions for as long as 6 years. His education has included not only scientific discussions and guidance in skills for presentations/thesis writing, but also showing me how a scientist should be; his attitude as a leading scientist always encourages and promotes myself spiritually.

I am heartily grateful to Associate Prof. Kiichirou Koyasu for his instructions in the gas phase experiments and theoretical calculations, the backbone of my research. Most of the development in my technical skills in the experiments is attributed to his teaching, although still my skills are no match to his at all. I greatly appreciate every help of Prof. Seiji Yamazoe (Tokyo Metropolitan Univ.); he gave me a variety of inspiring insights from the viewpoint of a synthetic, catalytic, and material chemist as well as an X-ray spectroscopist. I am especially thankful to Assistant Prof. Shinjiro Takano for the fruitful discussions and his daily support not only as a faculty staff but also as a great senior colleague in the close generation.

I respectfully acknowledge Prof. Emeritus Koichi Ohno (Tohoku Univ.) for providing me GRRM programs and for his expert advice. He is a chair of Institute for Quantum Chemistry Exploration (IQCE), which is also acknowledged for the financial support (IQCE Research Fellowship for Young Scientists). I am grateful to Prof. Hiroshi Nishihara (The Univ. of Tokyo) for allowing my access to a commercial MALDI mass spectrometer in my preliminary experiments.

I wish to show my appreciation to Prof. Mingfei Zhou, Associate Prof. Mohua Chen, and Ms. Xuan Wu (Fudan Univ.) for their collaboration in matrix-isolation IR spectroscopy (Chapter 4). The laboratory members supported me with warm hospitality during my stay in Fudan.

I am grateful to Ms. Yuka Sakurai for her every effort with exceeding kindness including the support in office work. The thanks also go to the current laboratory members: Dr. Liang Feng, Mr. Ryo Takahata, Mr. Ryohei Tomihara, Mr. Shun Hayashi, Mr. Keisuke Hirata, Mr. Sojiro Emori, Mr. Kazuyuki Tsuruoka, Mr. Tsubasa Omoda, Mr. Naoto Sasaki, Mr. Daiki Shuto, Mr. Toshiaki Yanase, Mr. Hiroki Yamada, Mr. Hiroki Yamamoto, Mr. Naoaki Shinjo, Mr. Yuto Nakajima, Mr. Shingo Hasegawa, Mr. Rei Horie, Mr. Shunichi Yamazaki, Mr. Kuenhee Kim, Mr. Wei Loon Lim, Mr. Mizuki

Shimojima, Mr. Haru Hirai, and Mr. Atsushi Matsuo. Furthermore, I really want to offer my special thanks to Dr. Tomomi Watanabe for her kind and warm instructions in my age of bachelor and master course degrees, as well as to the other former laboratory members: Assistant Prof. Jun-ichi Nishigaki (Tokyo Metropolitan Univ.), Dr. Prasenjit Maity, Dr. Mohammad Jakir Hossain, Dr. Md. Jafar Sharif, Dr. Hirokazu Kitazawa, Dr. Tachamapan Yoskamtorn, Dr. Diego J. Guzman, Ms. Nana Kawada, Ms. Setsuka Arii, Mr. Masaru Urushizaki, Mr. Akimaro Yanagimachi, Mr. Shota Matsuo, Mr. Teppei Misumi, Mr. Yuichiro Kawahara, Mr. Ryo Ishida, Mr. Tatsuya Higaki, Mr. Keishiro Yamashita, and Mr. Ryota Shibuya. Mr. Yanagimachi and Mr. Tsuruoka are also acknowledged for their collaborations in improvements of the mass and photoelectron spectrometers (Chapter 3).

I would like to express my important debt to Mr. Kunihiro Aoshima (ADCAP Vacuum Technology Co.Ltd.) for his kind instructions in design of the experimental apparatus.

I acknowledge a Japan Society for the Promotion of Science (JSPS) Research Fellowship for Young Scientists for the financial supports.

Finally, I sincerely thank my friends and family, who are my spiritual supports at all times.

Satoru Muramatsu